universität wien

DISSERTATION / DOCTORAL THESIS

Titel der Dissertation / Title of the Doctoral Thesis

„On lee waves and rotors“

verfasst von / submitted by

Mag. rer. nat. Johannes Sachsperger

angestrebter akademischer Grad / in partial fulfilment of the requirements for the degree of

Doktor der Naturwissenschaften (Dr. rer. nat.)

Wien, 2016 / Vienna 2016

Studienkennzahl lt. Studienblatt / degree programme code as it appears on the student record sheet:	A 796 605 415
Dissertationsgebiet lt. Studienblatt / field of study as it appears on the student record sheet:	Meteorologie
Betreut von / Supervisor	Prof. Dr. Vanda Grubišić

Acknowledgements

I would like to say thank you to those who supported me on my PhD journey. First of all, I am grateful to my mentor Vanda Grubišić for awaking my fascination on wave motions in fluid flows, for her supervision and for letting me grow my own ideas. Also, I thank her for being a good advisor in difficult situations and for giving me great opportunities for scientific exchange during research stays abroad. Another person without whom this work would not have been possible is Stefano Serafin. I thank him for supporting me since the first day I joined the research group and for the friendly collaboration with him over the years. Also, I am grateful to him for employing me within his research project. Furthermore, I am happy that Lukas Strauss decided to share an office with me and I thank him for the numerous scientific and nonscientific discussions. I profited also from scientific exchange with researchers from outside the group and would like to thank (in alphabetical order): Peter Baines, Branko Grisogono, Richard Rotunno, Ivana Stiperski, Miguel Teixeira, Volkmar Wirth and numerous others.

Thanks also go to my family and friends for their interest in my work and for detaching me from science. Lastly, I thank Anna for accompanying me with esprit every day during this period of my life. I am looking forward to what comes next.

Abstract

The prediction of airflow response on the lee side of mountains is one of the major goals of mesoscale alpine meteorology. Depending on the upstream flow conditions and the mountain, different flow responses may occur. Among the most striking responses are lee waves and hydraulic jumps. Both can give rise to vigorous vertical motion and flow separation, which leads to zones of severe low-level turbulence known as atmospheric rotors. One aim of this thesis is to investigate the coupling between mountain waves and rotors in order to predict rotor properties from the wave forcing. Therefore, a large portion of this thesis is devoted to exploring the properties of mountain waves, focusing on (i) vertically propagating gravity waves and (ii) trapped lee waves on the boundary-layer inversion. The thesis consists of three parts.

In the first part, we present results of numerical simulations of wave-induced rotor formation in two-dimensional uniformly stratified flows. The comparison of the rotor properties with linear predictions of wave amplitudes reveals strong rotor-wave coupling in nonhydrostatic flows. The strongest and highest rotors develop in nonlinear and nonhydrostatic flow regimes. In the near-hydrostatic flow regime, rotor properties were found not to scale with the primary mountain wave amplitude. In these cases, rotors form due to secondary wave motion along a strongly stratified jet on the lee slope of the mountain after the primary hydrostatic mountain wave breaks. The wavelength of these secondary waves was found to be consistent with wavelength estimations of interfacial wave theory.

In the second part, focusing further on interfacial lee waves, we review different types of trapped lee waves and the dependence of their wavelength to different environmental parameters. The observational study of a Madeira lee wave case reveals that interfacial waves, which are similar to surface water waves, represent also the most accurate description of lee waves on the boundary-layer inversion. Furthermore, the effects of free-atmospheric stratification on the horizontal wavelength of lee waves are discussed.

In the third part, a nonlinear analytical model for the amplitude of surface water waves is extended to atmospheric lee waves. This model assumes that energy flux convergence at an internal hydraulic jump is compensated by energy radiation through laminar waves. The wave amplitude is then proportional to the interface height difference across the jump. Amplitude predictions by this analytical model are in good agreement with measurements of lee waves in water tank experiments and corresponding numerical simulations. This suggests that trapped lee waves might originate at hydraulic jumps, when the height difference across the jump is relatively small. If the interface height difference is too large, lee waves break and a turbulent hydraulic jump forms. This regime transition can be predicted from the upstream flow parameters and the mountain height.

This thesis contributes to the current understanding of lee wave dynamics and provides analytical tools for the prediction of boundary-layer separation and low-level turbulence in the lee of complex terrain associated with atmospheric rotors.

Zusammenfassung

Die Vorhersage von Strömungsphänomenen auf der Leeseite von Gebirgen ist eines der Kernziele in der Gebirgsmeteorologie. Abhängig von Luftschichtung und Gebirgsgröße können sich unterschiedliche Phänomene im Lee ausbilden. Zu den eindrucksvollsten gehören Leewellen und hydraulische Sprünge, welche starke Vertikalbewegungen und Strömungsablösung in Verbindung mit starken Turbulenzregionen, bekannt als Rotoren, auslösen können. Ein Hauptziel dieser Arbeit ist es, die Rotoreigenschaften in Abhängigkeit der Leewelleneigenschaften zu untersuchen. Aus diesem Grund bezieht sich ein großer Teil dieser Dissertation auf die analytische Abschätzung der Wellenlänge und Amplitude von Gebirgswellen. Im Speziellen werden vertikal propagierende Schwerewellen und Leewellen an der Grenzschichtinversion betrachtet. Diese Arbeit ist in drei Teile aufgeteilt:

Im ersten Teil werden numerische Simulationen von welleninduzierter Grenzschichtablösung in einer zweidimensionalen Strömung mit konstanter Schichtung und konstantem Wind untersucht. Der Vergleich von Rotoreigenschaften und Abschätzungen der Leewellenamplitude durch lineare Theorie zeigt, dass Rotoren in nichthydrostatischen Strömungen eng mit der Gebirgswelle skalieren. Im Gegensatz dazu sind Rotoren im beinahe hydrostatischen Strömungsregime nicht an die primäre Gebirgswelle gekoppelt, sondern entstehen durch sekundäre Wellenentwicklung entlang eines stark geschichteten Jets, wenn die primäre Welle bricht. Die Wellenlänge dieser sekundären Welle ist konsistent mit den Wellenlängenabschätzungen linearer Grenzflächenwellentheorie.

Im zweiten Teil wird ein Überblick über unterschiedliche Leewellenarten und deren Wellenlängenabhängigkeit in Bezug auf unterschiedliche Strömungsparameter präsentiert. Eine Fallstudie zu einem Leewellenereignis in Madeira zeigt, dass Leewellen an der Grenzschichtinversion am adäquatesten als Grenzflächenwellen, ähnlich zu Wellen an der Wasseroberfläche, beschrieben werden können. Weiters wird der Einfluss der Schichtung in der freien Atmosphäre auf die Wellenlänge diskutiert.

Im dritten Teil wird ein nichtlineares analytisches Modell für die Amplitude von Wasserwellen erweitert und auf atmosphärische Leewellen angewandt. Im Modell wird angenommen, dass die Energieflusskonvergenz an einem internen hydraulischen Sprung durch die Energieabstrahlung durch Leewellen kompensiert wird. Dadurch ist die Amplitude von Leewellen proportional zur Höhendifferenz der Grenzfläche am hydraulischen Sprung. Die gute Übereinstimmung des analytischen Modells mit Messungen in Wassertankexperimenten und dazugehörigen numerischen Simulationen legt nahe, dass Leewellen an internen hydraulischen Sprüngen entstehen wenn die Höhendifferenz der Grenzfläche gering ist. Ist der Sprung zu groß, bricht die Leewelle und ein turbulenter hydraulischer Sprung bildet sich aus. Dieser Regimeübergang kann aus den Strömungsparametern und der Gebirgshöhe vorhergesagt werden.

Diese Arbeit trägt zu einem umfassenderen Einblick in die Dynamik von Leewellen an der Grenzschichtinversion bei und entwickelt analytische Modelle für die Vorhersage von leeseitiger Grenzschichtablösung und Turbulenz im Zusammenhang mit atmosphärischen Rotoren.

Contents

Chapter 1

Introduction

Waves are among the most fascinating and esthetic phenomena in fluid flows. They may occur when forces in the interior or at the free surface of the fluid act towards restoring a balanced unperturbed state. An illustrative example is when a stone falls into a pond with a smooth water surface releasing a gravity wave that propagates laterally on the surface in concentric circles. Those waves are harmless on the scale of a pond, but can be hazardous on a much larger scale in the ocean in form of tsunami waves. Tsunamis are generated in deep water, where they have long wavelength ($\sim$100 km) and small amplitude ($\sim$1 m) and can barely be noticed by an observer. However, as those waves approach the shallow-water region at the coast, the wavelength decreases while the amplitude dramatically increases due to mass conservation, causing devastating flooding in coastal areas.

Analogous to surface waves in the ocean, horizontally propagating waves can also occur in the atmosphere, where they are typically generated on the lee side of mountains. Those waves are known as *lee waves* and can often be observed in satellite images as cloud stripe pattern, see the example in Fig. 1.1. Despite their harmless appearance, they may lead to extreme flow responses if their amplitude becomes large. In those cases, the flow accelerates as it passes over the mountain forming a strong downslope windstorm on the lee side followed typically by an adjacent large amplitude lee wave train further downstream. Zones of strong low-level turbulence, known as *atmospheric rotors*, may arise below the lee wave crests when the wave-induced pressure gradient forces are strong enough to cause flow separation. In the most energetic cases, the lee wave train is replaced by an *internal hydraulic jump*, which represents an abrupt expansion of the wind storm layer to the downstream unperturbed atmosphere causing extreme turbulence and vigorous vertical motion. It can be inferred from those events that waves may pose a hazard to air and road traffic, impact the power yield of wind turbines or wash out polluted air in alpine valleys. Therefore, accurate forecasts of such high impact weather events are important.

Today, the dynamics of atmospheric gravity waves is relatively well understood from numerous case studies combining observations, theory and numerical simulations. However, their prediction can still be a challenging task for operational forecasters, in particular if the horizontal wavelength is small ($\lesssim$ 10 km) compared to the horizontal resolution of op-

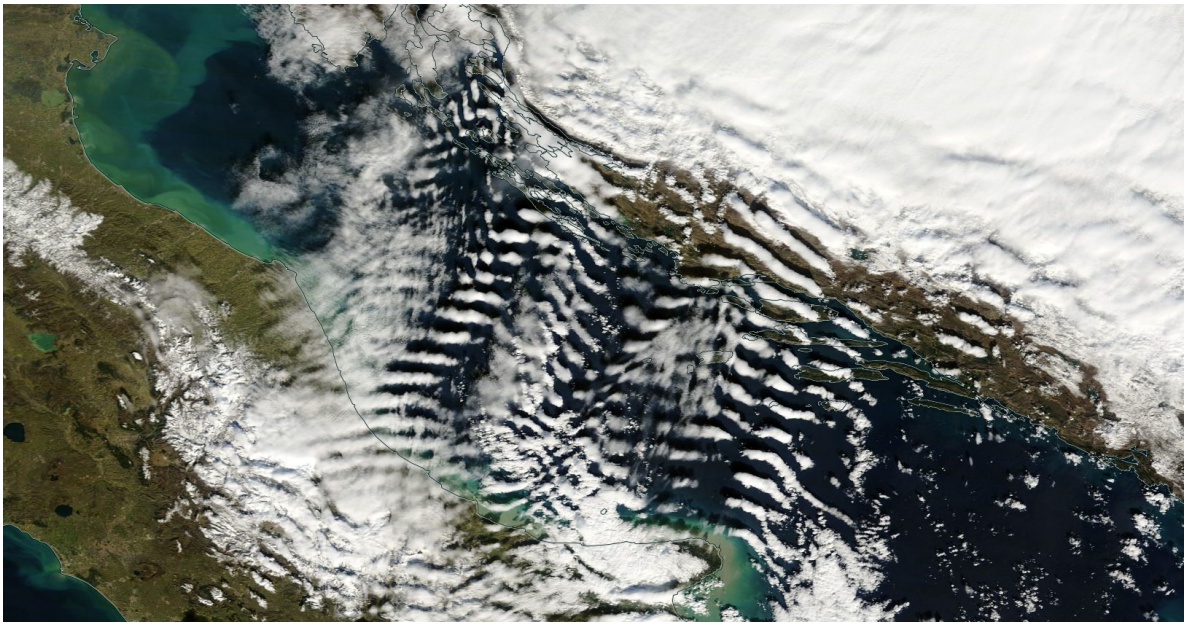

Figure 1.1: MODIS satellite image of a lee wave event on 10 Februar 2015 generated by the Dinaric Alps at the Croatian coast. Flow comes from north east. [from NASA Worldview, `https://worldview.earthdata.nasa.gov`]

erational numerical weather prediction models. In addition to resolution issues, numerical models also tend to smear out sharp vertical gradients, e.g. in temperature, which are often essential for gravity wave development. Consequently, the formation of gravity waves is often not captured in the models or underestimated in terms of amplitude and severe wave responses in the lee of mountains may be overlooked in the forecasts. Simple analytical models for wavelength and amplitude as well as flow regime diagrams are, therefore, required to efficiently predict the flow response in the lee of a mountain based on the upstream flow profile.

This thesis investigates the wavelength and amplitude of orographically-induced lee waves, which play a key role in the formation of rotors and the onset of low-level turbulence. The main aim of this work is to relate the wave properties to the upstream flow parameters in order to predict the onset of turbulence from the upstream flow conditions. The introduction begins with a short overview of research related to mountain waves (section 1.1), followed by a review of different wave types developing in different flow configurations in section (1.2). The third part of the introduction (section 1.3) focuses on the process of wave-induced boundary-layer separation, which is responsible for the generation of low-level turbulence.

1.1 A short overview of research on waves in fluids

Today's knowledge of the dynamics of mountain waves is the result of a 300-year long record of significant discoveries on wave motions in fluids. Two typical flow scenarios for mountain waves have been established. First of these is multi-layer flow with a density discontinuity between the individual fluid layers, along which interfacial waves may develop (described by *interfacial wave theory*). Such a scenario can be applied to the atmosphere in case of a well-mixed (netural) boundary layer topped by a boundary-layer inversion, above which lies a continuously stratified free atmosphere. The second scenario considers continuously-stratified fluid layers, in the interior of which internal gravity waves may form (described by *internal gravity wave theory*).

1.1.1 Interfacial wave theory

First systematic studies of waves in fluids date back to the late 17$^{\text{th}}$ century, when Isaac Newton first described the dependence of the frequency of deep-water waves on their wavelength, i.e. he established the frequency dispersion relationship (FDR). As described by Craik (2004), this discovery set off the quest for a general mathematical description of surface waves in fluids of arbitrary depth. Among the first to correctly describe those waves was Airy (1841). Only a short time later, Stokes (1847) extended Airy's theory by adding a second fluid layer of different density on top of the first layer and obtained the FDR for internal waves at a density interface, such as the boundary-layer inversion.

Probably the first study of mountain waves using interfacial wave theory was published in the well-known paper by Scorer (1949). Along with lee waves in continuously stratified flows[1], Scorer also analyzes the case of waves that form along an inversion underneath a layer of calm air. For a neutrally stratified lower layer, such as the convective boundary layer, the FDR of those lee waves becomes identical to that of Airy (1841), except for reduced gravity. In the subsequent years, interfacial wave theory had not received much attention in the meteorological literature; most likely because the theory of waves in continuously-stratified fluids was discovered and heavily investigated at about that time (Scorer, 1949). Interfacial waves have been reintroduced only recently by Vosper (2004) to describe certain aspects of lee waves. Vosper examined two-dimensional flow over a mountain with a neutral lower layer topped by an inversion above which lies a continuously-stratified atmosphere. He found critical values of height and strength of the boundary-layer inversion for the development of lee waves. Vosper also discusses the case of large amplitude waves, which may lead to atmospheric rotors (see section 1.3).

One aspect of this thesis is the review of important theoretical frameworks for interfacial waves and the assessment of their capabilities in predicting the wavelength of lee waves on

[1] Scorer's (1949) paper is much better known for the theory of trapped lee waves (see section 1.2.2), which form on the lee side of a mountain due to wave energy trapping in layers close to the ground due to the variation of stability and wind with height.

the boundary-layer inversion (see chapter 3).

In the limit of infinitely long lee wave wavelength, interface dynamics can be explained in the framework of hydraulic theory. This theory is hydrostatic and based on the principles of mass and momentum conservation. Therefore, it can describe nonlinear flows. One of the first significant studies that employed hydraulic theory has been published by Rayleigh (1914) who was interested in the nature of hydraulic jumps on the water surface. Assuming conservation of mass and momentum across a jump, Rayleigh showed that energy cannot be conserved at the transition and accumulates at a certain rate depending on the jump size. This excess energy is converted into turbulent kinetic energy, leading to mixing in the jump[2]. Based on these findings, Favre (1935) carried out a series of water tank experiments and discovered that the accumulating energy at small jumps is not converted to turbulence, but rather it is radiated downstream through laminar waves. This approach has been described mathematically by Lemoine (1948). He combined a hydraulic jump model with a linear wave propagation model to obtain the amplitude that a wave disturbance of certain wavelength must have in order to radiate energy at the same rate as energy accumulates at the jump.

Long (1954) correctly pointed out that hydraulic jumps may also occur in the atmosphere and formulated a two-layer hydraulic model to predict internal jumps based on the upstream flow conditions and the mountain height. Another important hydraulic model for topographic flow is the single layer model of Houghton and Kasahara (1968), which is in close agreement with that of Long. Given the high number of citations, these two contributions can be regarded as the classical theory of hydraulic jumps that applies to atmospheric flows.

So far, to the best knowledge of the author, Lemoine's approach for the amplitude of water waves has not been extended to atmospheric lee waves. This missing contribution is presented in chapter (4) of this thesis.

1.1.2 Internal gravity wave theory

Taylor (1931) and Goldstein (1931) realized that discontinuities in atmospheric flows are not realistic because density typically changes continuously across a layer of finite thickness. In order to study instabilities of waves in stratified flows, they independently derived the wave equation for small amplitude internal gravity waves, which is now commonly referred to as the *Taylor-Goldstein Equation*. A similar result has been obtained also by Haurwitz (1931a,b), as described in Craik (1988), but his work did not seem to have received much attention in the literature.

With the rise of aviation in the early 20$^{\text{th}}$ century, strong up- and downdrafts and severe turbulence encountered by glider pilots have been attributed to internal waves in the pioneering studies by Küttner (1938, 1939). First linear analytical solutions of mountain waves were then presented by Lyra (1940, 1943). In the latter paper, Lyra discusses the formation of

[2]Rayleigh verified his theory qualitatively with experiments in a sink, where a stream of water striking a plane surface creates a hydraulic jump, as explained in the appendix of his paper.

atmospheric rotors induced by the pressure field of the wave (see also section 1.3). Since he had used rectangular obstacles in his study, his work had received some criticism and was extended to smooth bottom topography by Queney (1947, 1948) resulting in more realistic solutions and better agreement with observations, as described in a review by Queney et al. (1960). A short time later, Scorer (1949) stated that the lee waves studied by Lyra and Queney are insignificant for rotor formation at the ground[3], and presented the linear theory of resonant lee waves. This theory applies to vertically propagating waves that are reflected downward at a certain level due to vertical variation of stratification and wind speed. The reflection leads to wave resonance forming a horizontally propagating wave that is trapped in the layer below (trapped lee wave). Today, almost 70 years later, Scorer's wave resonance theory still remains the commonly accepted explanation for the formation of trapped lee waves (Durran, 1986b; Wurtele et al., 1996; Teixeira, 2014). One important contribution of the recent years to further enlighten the dynamics of resonant lee waves is the numerical study of Durran (1986a). In his paper, analogies between hydraulic flow and two-layer stratified flow were found and discussed in the context of orographically-induced resonant lee waves.

Significant contribution towards understanding nonlinear wave dynamics in continuously stratified fluids was made in a set of papers by Long (1953, 1955). He developed an analytical model for finite amplitude waves, known today as *Long's model*. For the special case of constant wind speed and stability, Long showed that finite amplitude waves can be described with a linear partial differential equation of similar form as the Taylor-Goldstein equation. Although *Long's model* used a rigid lid condition at the top boundary, which is typically not appropriate for atmospheric flows, many following studies successfully used and extended his model to investigate finite amplitude effects in stratified flows, as described in Smith (1979). Among the most significant applications of Long's model is the theoretical study on downslope wind storms by Smith (1985). He attributed the strong accelerations of downslope winds to flow channeling between the surface and a stagnant wave-breaking region further aloft. Large amplitude waves have also been studied by Baines and Hoinka (1985) who, based on laboratory experiments, showed that waves in continuously-stratified flows can be strong enough to cause flow separation and rotor formation (see also section 1.3). In a later study, Baines (1995, p237) summarized the laboratory flow responses in a regime diagram that predicts flow separation and rotor formation based on upstream stratification, wind speed and the mountain height and width.

In this thesis, high-resolution two-dimensional numerical simulations are carried out to confirm the regime transitions in the diagram of Baines (1995, p237) (see chapter 2). Moreover, the mechanisms of rotor formation in the simple case of uniformly stratified flow are investigated focusing on the dependence of rotor height and strength on different mountain wave regimes.

[3]Scorer was wrong on that point as was shown later in studies of Long (1955) and Baines (1995) on rotor formation in uniformly stratified flows.

1.2 Mountain-induced gravity waves

In the framework of linear theory, isolated mountains excite a spectrum of wave modes, which are independent of each other and show a unique propagation character depending on the wavenumber k. To obtain the complete wave structure, the Fourier integral over all wave modes needs to be evaluated. In order to study the propagation properties of mountain waves it is, however, instructive to consider a single monochromatic wave mode k, keeping in mind that the full solution is composed of a range of wavemodes. In the following sections, wave propagation in typical configurations of flow over mountains is investigated.

1.2.1 Uniformly stratified flow

Wave disturbances in an infinitely-deep continuously-stratified fluid layer propagate throughout the interior of the fluid layer as internal gravity waves in vertical and horizontal direction. Some properties of this important class of waves are reviewed in the proceeding sections.

The governing equations

Internal gravity waves can be described with the linearized framework of the Euler equations for a two-dimensional (x, z), non-rotating and inviscid flow. Applying the Boussinesq approximation and assuming a hydrostatically balanced background flow, the linearized equations of motion are (Nappo, 2012)

$$\frac{\partial u}{\partial t} + U\frac{\partial u}{\partial x} + w\frac{\partial U}{\partial z} = -\frac{1}{\rho_0}\frac{\partial p}{\partial x} \tag{1.1}$$

$$\frac{\partial w}{\partial t} + U\frac{\partial w}{\partial x} = -\frac{1}{\rho_0}\frac{\partial p}{\partial z} - \frac{\rho}{\rho_0}g \tag{1.2}$$

$$\frac{\partial u}{\partial x} + \frac{\partial w}{\partial z} = 0 \tag{1.3}$$

$$\frac{\partial \rho}{\partial t} + U\frac{\partial \rho}{\partial x} + w\frac{\partial \rho_0}{\partial z} = 0 \quad . \tag{1.4}$$

Here, the quantities $\psi = (u, w, p, \rho)$ denote the perturbations of horizontal and vertical wind speed, pressure and density respectively. The background flow speed is $U = U(z)$, the density profile is $\rho_0 = \rho_0(z)$ and g represents the gravitational acceleration. Equations (1.1) and (1.2) are the momentum equations in horizontal and vertical direction and Equations (1.3) and (1.4) ensure conservation of mass and energy.

Assuming wave-like perturbations $\psi = \tilde{\psi}(z)\exp[i(kx - \omega t)]$, with horizontal wavenumber k, apparent wave frequency ω, and vertical wave structure $\tilde{\psi}(z)$, Equations (1.1)–(1.4) yield

the *polarization relationships* of internal gravity waves

$$-i\omega\tilde{u} + iUk\tilde{u} + \tilde{w}\frac{dU}{dz} = -\frac{ik}{\rho_0}\tilde{p} \tag{1.5}$$

$$-i\omega\tilde{w} + iUk\tilde{w} = -\frac{1}{\rho_0}\frac{d\tilde{p}}{dz} - \frac{\tilde{\rho}}{\rho_0}g \tag{1.6}$$

$$ik\tilde{u} + \frac{d\tilde{w}}{dz} = 0 \tag{1.7}$$

$$-i\omega\tilde{\rho} + iUk\tilde{\rho} + \tilde{w}\frac{d\rho_0}{dz} = 0 \quad . \tag{1.8}$$

These equations are an important result, because they relate the phase and amplitude of the perturbations of horizontal and vertical wind speed, pressure and density. Therefore, they can be used to examine whether disturbances in measurements or numerical simulations obey to internal gravity wave theory. If so, the relations (1.5)–(1.8) must be satisfied (if nonlinear- and viscous effects are unimportant).

The Taylor-Goldstein equation

The wave equation for internal gravity waves is the Taylor-Goldstein equation (Taylor, 1931; Goldstein, 1931), which gives solutions for the vertical structure $\tilde{\psi}(z)$ of the wave. It can be derived from the polarization relationships (1.5)–(1.8), as explained in detail by Nappo (2012). For stationary waves ($\omega = 0$) in a fluid of large scale height, such as the atmosphere, the Taylor-Goldstein equation becomes

$$\frac{d^2\hat{w}}{dz^2} + \left[\frac{N^2}{U^2} - \frac{1}{U}\frac{d^2U}{dz^2} - k^2\right]\hat{w} = 0 \quad , \tag{1.9}$$

where N represents the buoyancy frequency and $\hat{w} = (\rho_0(z)/\rho_s)^{1/2}\ \tilde{w}$ is an auxiliary variable assuming an exponential density profile, ρ_s being the density at the surface. In the general case of variable N and U with height, the Taylor-Goldstein equation is typically solved numerically. However, simple analytical solutions are possible when N and U are uniform with height. Then, the above equation reduces to

$$\frac{d^2\hat{w}}{dz^2} + \left[\frac{N^2}{U^2} - k^2\right]\hat{w} = 0 \quad . \tag{1.10}$$

The term in the brackets represents a vertical wave number $m = \pm(N^2/U^2 - k^2)^{1/2}$. Since Equation (1.10) is a hyperbolic partial differential equation, the Taylor-Goldstein equation has wave-type solutions of the form

$$\hat{w} = Ae^{imz} + Be^{-imz} \tag{1.11}$$

and the vertical wind speed perturbation becomes

$$w(x,z) = \tilde{w}e^{-ikx} = \left(\frac{\rho_s}{\rho_0(z)}\right)^{\frac{1}{2}}\hat{w}e^{-ikx}. \tag{1.12}$$

The two terms on the right in Equation (1.11) represent an up- and downward propagating branch of the wave respectively. The coefficients A and B need to be determined from the boundary conditions. Four combinations of $\pm k$ and $\pm m$ are possible, representing different propagation directions. In the case of mountain waves, the combination $k < 0$ and $m < 0$ is the only physical solution (Nappo, 2012, p61), implying that the wave energy source is at the surface and wave fronts stand against the flow.

Possible forms of mountain waves

Depending on m, different mountain wave regimes can occur. It is instructive to consider the case of a purely upward moving wave in a flow with constant N and U. Since k and m are negative, A must be zero in Equation (1.11) to recover the physical solution for mountain waves ($B = 0$ would lead to an infinite growth of the wave amplitude with height, as shown further below). For a sinusoidal surface corrugation of the form $h(x) = H\exp(-ikx)$, the solution for vertical wind speed (Equation 1.12) can be determined from Equation (1.11) and the parallel flow condition $w(z = 0) = Udh/dx$ and is

$$w(x, z) = -ikUH \left(\frac{\rho_s}{\rho_0(z)} \right)^{\frac{1}{2}} e^{-i(kx+mz)} \quad . \tag{1.13}$$

Using the polarization relations (1.5)–(1.7) for stationary ($\omega = 0$) waves, the perturbations of horizontal wind speed and pressure become

$$u(x, z) = -\frac{m}{k} w = imUH \left(\frac{\rho_s}{\rho_0(z)} \right)^{\frac{1}{2}} e^{-i(kx+mz)} \tag{1.14}$$

$$p(x, z) = -\rho_0 U u = -i\rho_0 m U^2 H \left(\frac{\rho_s}{\rho_0(z)} \right)^{\frac{1}{2}} e^{-i(kx+mz)} \quad . \tag{1.15}$$

Different wave forms can arise depending on the parameter

$$l^2 = \frac{N^2}{U^2} - \frac{1}{U} \frac{d^2U}{dz^2} \quad , \tag{1.16}$$

which is often termed *Scorer parameter* and controls whether the exponents in the solutions (1.13)–(1.15) are real or imaginary. This has a large influence on the vertical wave structure and the phase relations between the wave quantities $\hat{\psi}$. In the case of uniform background flow speed, the Scorer parameter simplifies to $l^2 = N^2/U^2$ and two types of wave solutions are possible.

1. **Periodic (propagating) solution:** $l^2 > k^2$
   In this case, the vertical wavenumber $m = -(l^2 - k^2)^{1/2}$ is real and the exponent of the solutions is imaginary $\hat{\psi}(z) \sim \exp(-imz)$. Consequently, the vertical structure of the wave field is periodic, as becomes apparent in Fig. 1.2a, with the vertical wavelength

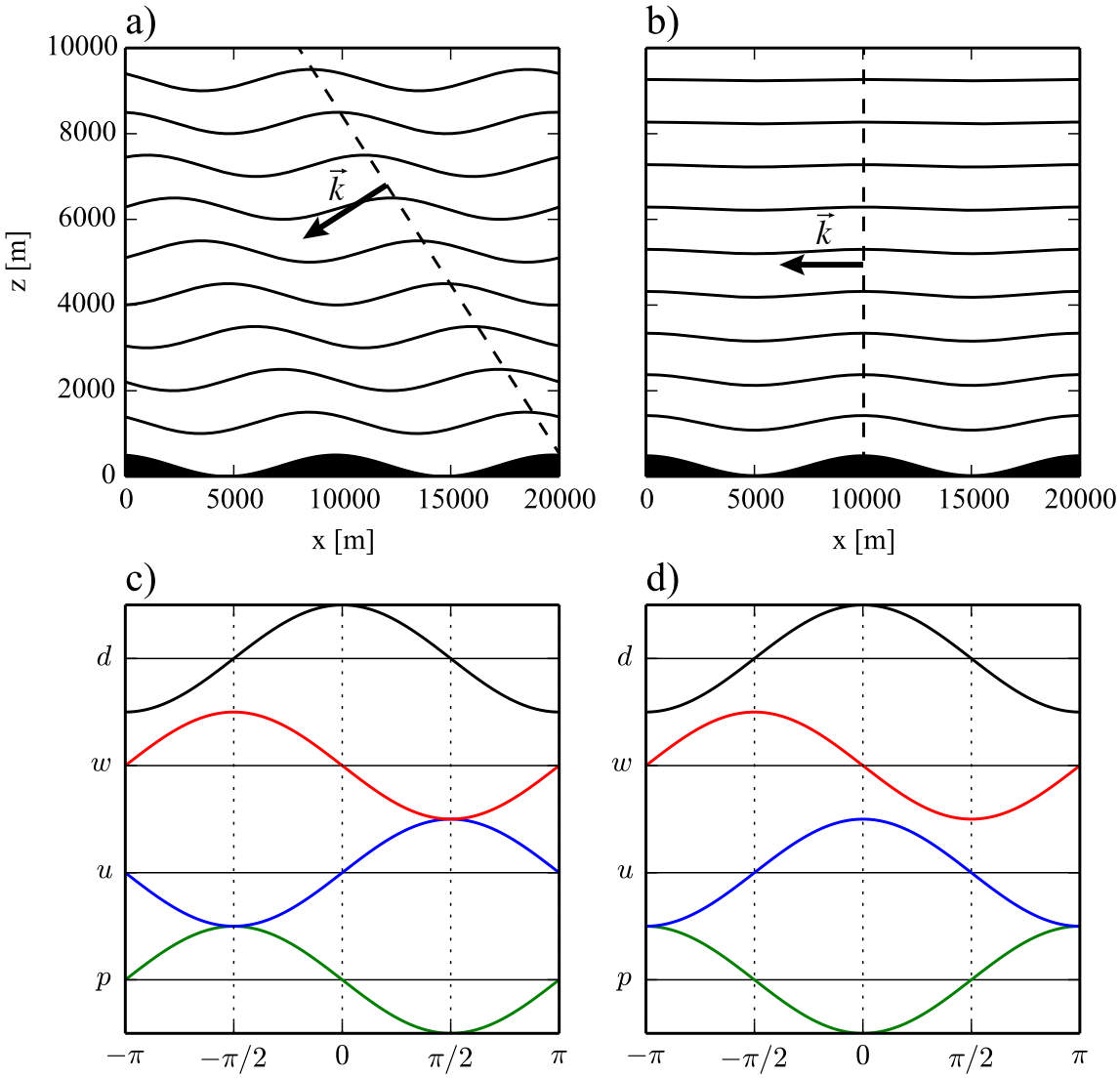

Figure 1.2: Displacement fields for (a) propagating and (b) evanescent waves. The wave solutions are calculated with (a) $N = 0.01$ s^{-1} and (b) $N = 0.0055$ s^{-1} and $U = 10$ m s^{-1} and $H = 250$ m. The dashed lines in (a) and (b) indicate the phase line of the wave and solid arrows represent the wave number vector. The bottom row shows the polarization relations between displacement d, vertical and horizontal wind speed w and u and pressure p for (a) propagating and (b) evanescent waves.

$\lambda_z = 2\pi/m$. Apparently, there is an upstream tilt of the phase lines (dashed line in Fig. 1.2a), which is perpendicular to the wavenumber vector $\vec{k} = (k, m)$. Wave energy is transported upward and upstream with the group velocity $\vec{c_g} \sim (m, -k)$ in parallel direction to the phase lines.

2. **Damping (evanescent) solution:** $l^2 < k^2$
   In the damping case, the vertical wavenumber becomes imaginary with $m = in$, where $n = -(k^2 - l^2)^{1/2}$, and the wave disturbance damps out with height, since the exponent in $\hat{\psi}(z) \sim \exp(nz)$ is negative ($n < 0$) and real. It becomes clear, that selecting the wave branch $A > 0$ and $B = 0$ in the generic solution (1.11) would lead to an increase of the wave amplitude with height as the exponent of $\hat{\psi}(z) \sim \exp(-nz)$ would be positive. This scenario is not observed in nature and, thus, regarded as unphysical. In the case of evanescent waves, the vertical components of $\vec{k}$ and $\vec{c}_g$ are imaginary indicating purely horizontal energy propagation. The corresponding wave field is shown in Fig. 1.2b, in which no phase tilt is apparent and the wave damps out with height.

The phase relationships of propagating (Fig. 1.2c) and evanescent waves (Fig. 1.2d) differ in the phase of u and p with respect to the wave crest ($x = 0$). In the former case, u and p are asymmetric, while in the latter case they are symmetric about the crest. The relation between w and the displacement d is consistent with the parallel flow condition and the phase relation between p and u is a manifestation of the exchange of potential and kinetic energy.

In this section, the simple case of upward propagating waves in uniformly-stratified flow was discussed. Adding more fluid layers to the system allows to study more complex flows with variable N and U in the upstream profile (e.g. Houghton, 1964; Klemp and Lilly, 1975). The next section describes multi-layer fluid systems in which wave trapping may occur.

1.2.2 Multi-layer flow

In multi-layer fluids, vertically propagating waves can get reflected at a layer interface above which wave propagation is not supported. The reflected wave is then trapped in the layer below and a horizontally propagating lee wave may develop. The dynamics of wave trapping can be easiest understood from a simple two-layer model, as is explained next.

Two-layer model for resonant lee waves

In the following, a system of two continuously-stratified fluid layers with vertically uniform flow speed is considered, see Fig. 1.3a. If wave trapping occurs, the upward propagating wave branch (B in Equation (1.11)) is reflected at the interface and the downward propagating branch (A in Equation (1.11)) becomes non-zero. The superposition of the two wave branches results in vertical phase lines and a horizontally propagating *resonant* lee wave (Scorer, 1949; Durran, 1986b). In contrast to the uniformly stratified case, for which all wave modes can become stationary depending on the phase tilt, only selected wave modes can become stationary in the case of wave trapping. These modes can be identified by solving the Taylor-Goldstein Equation (1.10) in each fluid layer. Two generic wave solutions to Equation (1.10) are considered

$$\hat{w}_1(x, z') = A_1 e^{im_1 z'} + B_1 e^{-im_1 z'} \tag{1.17}$$

$$\hat{w}_2(x, z') = A_2 e^{im_2 z'} + B_2 e^{-im_2 z'}, \tag{1.18}$$

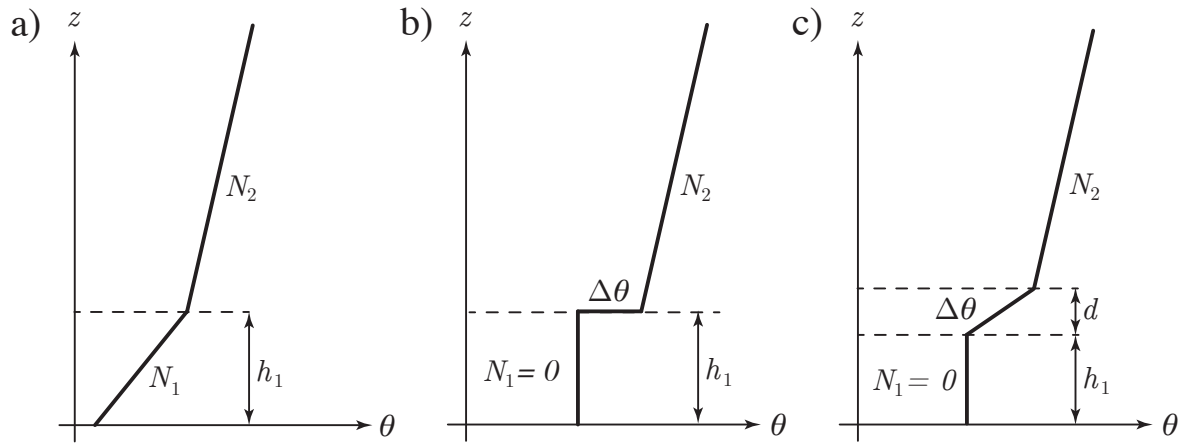

Figure 1.3: Potential temperature profiles of (a) two-layer model for resonant lee waves, (b) two-layer model for interfacial lee waves and (c) three-layer model for interfacial waves. Symbols N_i, θ, h_1 and d denote stratification, potential temperature, interface height and inversion layer depth respectively. In all three cases (a)–(c) wind speed U in uniform with height.

where the subscript $i = \{1, 2\}$ denotes the lower and upper fluid layer respectively and $z' = z - h_1$ is the geometric height with respect to the interface height h_1. The coefficients A_i and B_i need to be determined from the boundary conditions (BC).

Adding a second fluid layer requires two additional boundary conditions at the layer interface in order to couple their dynamics. First, the kinematic boundary condition, which ensures continuous vertical motion across the interface and, second, the dynamic boundary condition, which represents continuous pressure. In total, four boundary conditions are required in a two-layer system.

BC1: *Parallel flow condition*, $\hat{w}_1 = 0$, at the lower boundary ($z' = -h_1$). Here, flat terrain $h(x) = 0$ is assumed, which is sufficient to determine the possible stationary wave modes k of the system. For amplitude estimations, non-zero terrain $\hat{w}_1(z' = -h_1) = U\partial h/\partial x$ needs to be included here.

BC2: *Kinematic boundary condition*, $\hat{w}_1 = \hat{w}_2$, at the layer interface ($z' = 0$). This BC couples the cross-interface motion. Interface parallel motion ($\hat{u}$) does not have to be coupled, because it does not transfer momentum across the interface (in the case of linear waves).

BC3: *Dynamic boundary condition*, $d\hat{w}_1/dz = d\hat{w}_2/dz$, at the layer interface ($z' = 0$). This condition is equivalent to continuous pressure $\hat{p}_1(z' = 0) = \hat{p}_2(z' = 0)$, as becomes clear from the continuity equation (1.7) and the polarisation relation (1.5).

BC4: *Radiation condition*, $A_2 = 0$, in the upper layer. Consequently, only upward wave propagation is possible above the interface. Alternatively, e.g. for flows in a channel, a

rigid lid condition $\hat{w}_2(z' = h_2) = 0$ can be enforced here, which allows reflection from the upper wall of a channel (see for example chapter 4).

Substituting the generic solutions (1.17)–(1.18) into (BC1)–(BC4) leads to the frequency dispersion relationship of stationary resonant lee waves (Scorer, 1949)

$$\coth(im_1h_1) = \frac{m_2}{m_1} \quad . \tag{1.19}$$

Scorer showed that this equation has solutions only when two conditions are satisfied

$$l_1^2 > k^2 > l_2^2 \tag{1.20}$$

$$l_1^2 - l_2^2 > \frac{\pi^2}{4h_1^2} \quad , \tag{1.21}$$

$l_{1,2}$ being the Scorer parameter in the lower and upper layer respectively. Physically, the first condition means that the trapped wave mode k must be propagating in the lower- and evanescent in the upper layer, i.e. the wave must be trapped. The second condition implies that there is a minimum layer height h_1 in order to observe wave resonance. If h_1 is large, multiple resonant modes may occur, which can be determined by solving Equation (1.19) for k. Since the FDR (1.19) is transcendental with respect to k, it cannot be solved analytically. Therefore, numerical approaches, such as Newton's method, are necessary to determine the resonant modes for a given interface height h_1 and Scorer parameters l_1 and l_2. Typically, the longest wave mode (minimum k) is dominant in the flow field.

In the above description of lee waves, wind speed is assumed to be uniform with height and wave trapping occurs due to different stratifications in the layers (*temperature duct*). Such situations are, however, relatively rare in the atmosphere. Resonant lee waves are typically observed when vertical wind shear is present (*wind duct*, e.g. Stiperski and Grubišić, 2011). For variable wind speed $U = U(z)$, the Scorer parameter has the form of Equation (1.16) and wave trapping will occur either when U increases with height, or in the case of strong curvature, like in low-level jets. The analysis of the wind duct, however, requires numerical approaches and is out of the scope of the thesis.

Two-layer model for interfacial waves

Also interfacial lee waves, which form along density interfaces such as the boundary-layer inversion, can be studied with a two-layer model following the procedure of the previous section. The corresponding potential temperature profile is shown in Fig. 1.3b. Since a density (or potential temperature θ in compressible fluids) discontinuity is present at the layer interface, the dynamic boundary condition, which accounts for continuous pressure across the interface, needs to be extended in order to account for the density inhomogeneity. This can be done with a Taylor series expansion of pressure about the displacement of the wave at the interface, as is described in Vosper (2004). The dynamic boundary condition (BC3) then becomes

$$\frac{d\hat{w}_1}{dz} - \frac{d\hat{w}_2}{dz} = \hat{w}_1 \frac{g'}{U^2}, \tag{1.22}$$

where $g' = g\Delta\rho/\rho_0 = g\Delta\theta/\theta_0$ is reduced gravity. Due to the additional gravity term, cf. (BC3) and Equation (1.22), the gradient of vertical wind speed will not be continuous across the interface anymore.

The FDR of interfacial waves can be obtained analogously to the previous section by substituting the generic solutions (1.17)–(1.18) into the boundary conditions (BC1), (BC2), (1.22) and (BC4), and becomes (Vosper, 2004)

$$U^2 = \frac{g'}{k \coth(kh_1) + \sqrt{k^2 - l_2^2}} \quad . \tag{1.23}$$

In contrast to resonant lee waves, for which multiple stationary wave modes can exist, density interfaces support only a single stationary lee wave mode, which can be determined from the upstream flow conditions by solving Equation (1.23) numerically for k. Again, the wavelength of interfacial waves is independent of topography. For lee waves of relatively short wavelength, the deep-water approximation ($kh_1 \gg 1$, Turner, 1973) is typically appropriate and Equation (1.23) becomes analytically solvable with $k = g'/(2U^2) + N_2^2/(2g')$. Interfacial wave theory appears to be relatively accurate in predicting the wavelength of lee waves forming on the boundary-layer inversion, as discussed in chapter (3) below.

Three-layer model for interfacial waves

As was mentioned above, discontinuities are not realistic in atmospheric flows. Therefore, a stratified fluid layer of finite depth is a more appropriate representation of an inversion. The corresponding flow configuration consists of a neutral lower layer, a strongly stratified inversion layer and a continuously-stratified layer on top, see Fig. 1.3c. In this case, wave trapping occurs in the middle fluid layer for those wave modes that are evanescent above and below. The corresponding FDR can be obtained analogously to the procedure presented in the previous sections. However, additional boundary conditions (kinematic (BC2) and dynamic (BC3)) are necessary at the second layer interface, resulting in six BCs in total. The FDR for resonant wave modes becomes (Baines, 1995)

$$\left[\tan(m_1 h_1) - \frac{i m_1}{m_2}\right](m_2 - m_3) = e^{-2i m_2 d}\left[\tan(m_1 h_1) + \frac{i m_1}{m_2}\right](m_2 + m_3) \quad , \tag{1.24}$$

where d is the thickness of the inversion layer and m_i represents the vertical wavenumbers in the three layers $i = \{1, 2, 3\}$, numbered from below.

It can be readily shown that for $d = 0$ the three-layer FDR (1.24) becomes identical to Scorer's two-layer FDR (1.19), because zero thickness removes the middle layer. However, using the stratification $N_2 = (g'/d)^{1/2}$, which represents the change of $\Delta\theta$ across the inversion layer, wavelength estimations of the three-layer model (1.24) become similar to that of interfacial wave theory (1.23) for small but finite inversion layer thickness $d \gtrsim 0$, as can be shown numerically (see Fig. 3 of section 3.3). This circumstance suggests that interfacial lee waves correspond to the limiting case of resonant lee waves in an infinitely thin layer.

The models presented above are suitable for describing nonhydrostatic (short wavelength) waves. In the case of large amplitude waves, strong vertical motions occur together with strong horizontal pressure gradients at the surface. These properties are known to cause boundary-layer separation and severe turbulence in atmospheric rotors, as explained in the next chapter.

1.3 Boundary-layer separation

The boundary layer is the part of the flow which is in contact with a solid boundary. Whereas the rest of the fluid can be assumed to be inviscid if the Reynolds number is large, the boundary layer is influenced by friction and buoyancy fluxes. The conceptual model of a boundary layer has been developed by Prandtl (1904) and is of central importance in engineering applications, such as the aerodynamics of airfoils, but also very important in atmospheric flows. Atmospheric boundary layers are responsible for exchange processes between the surface and the free atmosphere further aloft (Stull, 2012). Therefore, boundary layers play an important role for, e.g., convection (Kalthoff et al., 2011), air pollution (Lareau et al., 2013; Gohm et al., 2009) or lee wave formation when strong boundary-layer inversions are present (see section 1.2.2; *Two-layer model for interfacial waves*).

Typically, the boundary layer remains attached to the surface. However, if a pressure gradient force decelerates the flow close to the surface to rest, stagnation occurs ($dU/dz = 0$ at the surface) and the flow separates from the surface as a consequence of mass continuity (Batchelor, 1967, p325). This process is known as *boundary-layer separation* (BLS) and has been discovered by Prandtl (1904). A key parameter for boundary-layer separation is the surface roughness, which is typically represented by the roughness length z_0. A rough surface causes a thicker boundary layer (Prandtl, 1904) and, therefore, reduces the flow speed close to the surface. As a consequence, the pressure gradient force can more easily decelerate the fluid near the surface to rest and the flow becomes more prone to boundary-layer separation.

When the atmospheric boundary layer separates from the surface, atmospheric rotors may form downstream of the separation point giving rise to strong turbulence. Early schematics of rotors were developed by Küttner (1938, 1939), Förchtgott (1949, 1957) and Holmboe and Klieforth (Sierra Rotors Project, 1954, 1957) based on glider measurements. Lacking numerical simulations and high resolution observational datasets, they interpreted the turbulent region as horizontal vortex tube that forms underneath the crest of a lee wave, see Fig. 1.4a; therefore the name *rotor*. Today, new insights from high-resolution numerical simulations and comprehensive observational studies revealed that the nature of rotors is substantially more complex. Doyle and Durran (2007) showed in their three-dimensional simulations that strong vorticity is confined to a thin layer, which, once lifted off the surface, breaks up into small vortices due to Kelvin-Helmholtz instability, see Fig. 1.4b. Strongest turbulence is evident in the shear lines of the up- and downdraft regions of the rotor.

Observational evidence for boundary-layer separation was found in several recent field campaigns: Mesoscale Alpine Program (MAP, Bougeault et al., 2001); NASA Orographic

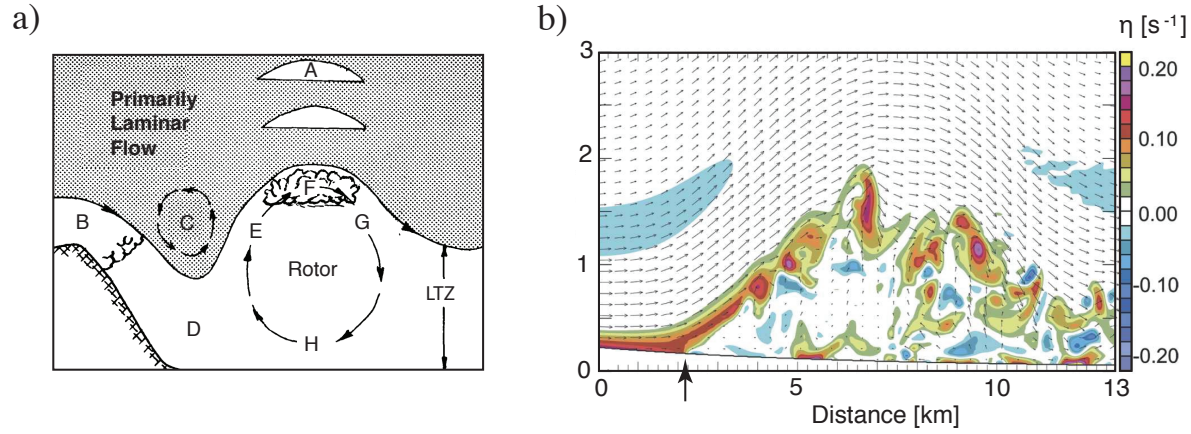

Figure 1.4: Panel (a) shows a schematic of rotor formation according to studies of Holmboe and Klieforth (1957) [adapted from Lester and Fingerhut (1974)] where shaded areas indicate laminar flow and white areas the lower turbulence zone (LTZ). The labels are: A lenticular cloud; B cap cloud; C reversed rotor; D gusty surface winds; E strong updrafts and severe turbulence; F rotor cloud; G downdrafts and severe turbulence; H reversed surface winds. Panel (b) shows a three-dimensional simulation by Doyle and Durran (2007, their Fig. 7). The large arrow indicates the separation point, small arrows indicate the flow direction in the x–z plane and colors indicate horizontal vorticity η. Flow is from left to right.

Clouds Experiment (NASA06, French et al., 2015); Terrain-induced Rotor Experiment (T-REX, Grubišić et al., 2008); Mountain Terrain Atmospheric Modeling and Observations Program (MATERHORN, Fernando et al., 2015); Meteor Crater Experiment (METCRAX II, Lehner et al., 2016). A detailed compendium of the most important observations regarding boundary-layer separation and rotor formation can be found in Strauss (2015). In essence, rotors according to the classical schematic from the 1960s in Fig. 1.4a could not be observed. Rather, they were found to be transient, sensitive to the upstream and downstream environment (valley atmosphere processes are important), display considerable small-scale variability and show weak, if at all, return flow. The only common properties with the old schematics are that they form underneath wave crests and feature strong turbulence concentrated at the shear lines along the up- and downdraft branches of the rotor.

Boundary-layer separation can be forced by evanescent or propagating waves, as described in section 1.2.1 and Fig. 1.2. The former case is termed as *bluff-body* BLS and the latter case is known as *wave-induced* BLS. In the following, these two types are discussed in more detail.

1.3.1 Bluff-body separation

This type of flow separation has been discovered by Prandtl (1904) in water tank experiments. In the atmosphere, it typically occurs leeward of steep mountains. In this case, the majority

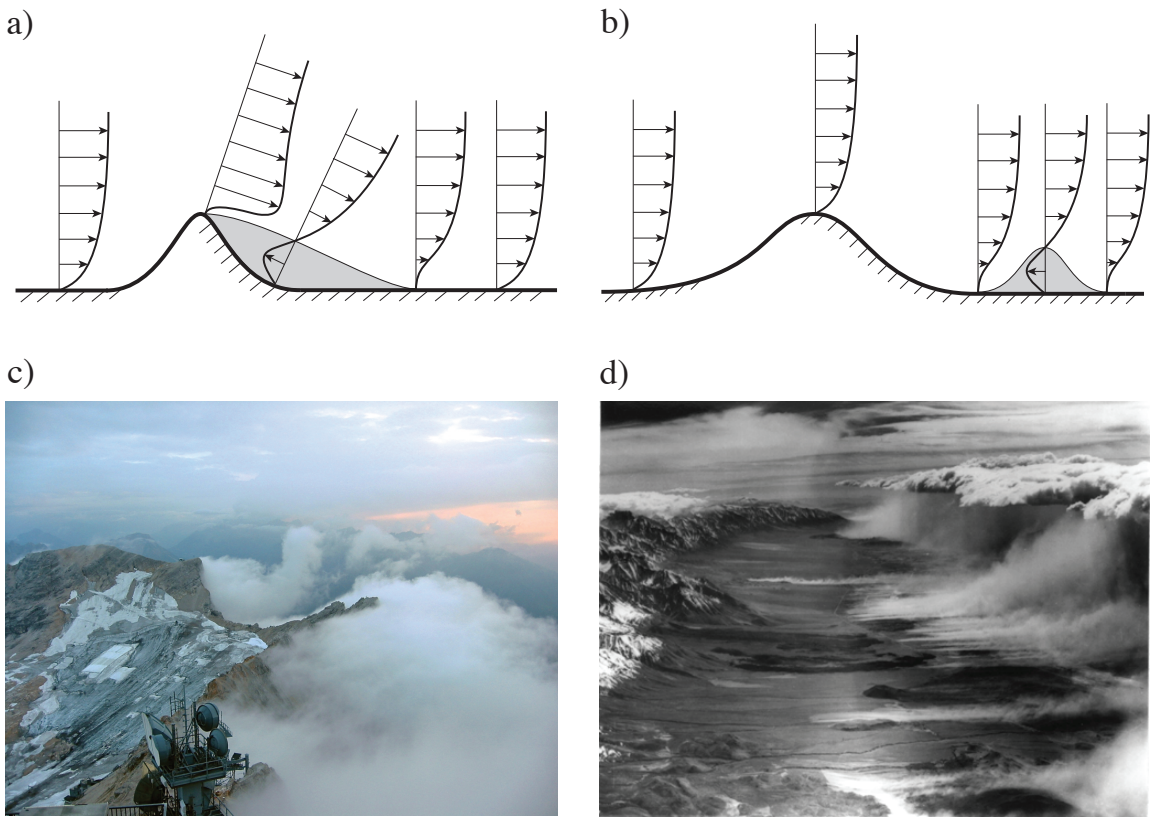

Figure 1.5: Schematic diagrams of (a) bluff-body separation and (b) wave-induced boundary-layer separation. The arrows indicate the flow speed profile and gray shades indicate separated air (rotors). Corresponding examples are shown in (c) bluff-body separation at Mt. Zugspitze (image from Wirth et al., 2012) and (d) wave-induced separation leeward of the Sierra Nevada (Photo taken by Robert Symons). The image in (d) is flipped to correspond to the flow direction in the corresponding schematic. Panel (a) and (b) are not to scale.

of the wave modes excited by topography are evanescent ($k^2 > l^2$) and the resulting flow shows a symmetric pressure field about the crest of the obstacle (cf. d and p at $x = 0$ in Fig. 1.2d). For a single evanescent wave mode with $m = k$, the pressure perturbation (1.15) at the surface ($z = 0$, $\rho_0 = \rho_s$) becomes

$$p_s = \rho_0 k U^2 H \cos(-kx) \quad . \tag{1.25}$$

Minimum pressure (note that $k < 0$) is found at the crest ($x = 0$) and maximum pressure close to the upstream and downstream foot of the mountain (Fig. 1.2d). When $|k|$ and H are both large (steep topography), the surface pressure minimum at the crest is strongly pronounced.

Considering the horizontal pressure gradient force

$$-\frac{1}{\rho_0}\frac{dp_s}{dx} = -k^2U^2H\sin(-kx) \quad , \tag{1.26}$$

it appears that deceleration occurs immediately leeward of the crest ($0 < -kx < \pi$) and, consequently, leeside flow separation occurs close to the mountain top. According to Equation (1.26), strong deceleration of the flow can be expected for steep mountains (k and H both large) and for strong wind speed U. At obstacles with salient edges (e.g. Mt. Zugspitze in Fig. 1.5c), where $k \to \infty$, flow separation occurs always in the lee (Batchelor, 1967, p330).

The schematic in Fig. 1.5a illustrates the process of bluff-body separation. When boundary-layer flow is advected over a steep mountain, strong deceleration in the lee leads to stagnation at the surface ($dU/dz = 0$) and the flow separates from the mountain. The region of separated air (wake, grey shades) originates typically close to the top of the mountain on the lee slope and extends further downstream until the outer flow reattaches to the surface. Recent airborne observations of orographically forced flows revealed that moderate to severe levels of turbulence may occur in the bluff-body separation wake of a mountain (Strauss et al., 2015b).

An atmospheric phenomenon related to bluff-body separation are banner clouds (see Fig. 1.5c), which have been studied extensively in recent years (e.g. Wirth et al., 2012; Schappert and Wirth, 2015; Prestel and Wirth, 2016) and found to occur predominantly in conditions for which bluff-body separation can be expected. Unlike the case of classical orographic clouds, which occur on the upwind side of a mountain, banner clouds develop on the lee side in the wake of three-dimensional topography. The necessary uplift for condensation originates from air parcels that go around the obstacle at low levels, entrain the wake in the lee and are raised into the cloud region. If blocking is strong, e.g. due to the presence of an inversion, vortices may shed from the obstacle (Prandtl, 1904; Schär and Smith, 1993), as can often be observed leeward of mountainous islands, such as Madeira (Grubišić et al., 2015), Gran Canaria (Nunalee et al., 2015) or Jan Mayen (Mohr, 1971).

1.3.2 Wave-induced separation

In the meteorological literature, wave-induced boundary-layer separation has received substantially more attention than bluff-body separation; probably because it is more important for aviation, since the resulting turbulence is stronger (Strauss et al., 2015a) and spreads over a wider area. In the case of wide mountains, boundary-layer separation typically occurs further downstream in the lee of the obstacle, in contrast to the bluff-body separating regime where the flow separates close to the crest. This happens because in the wave-induced case, the pressure field is asymmetric about the mountain top, with a maximum on the upstream side and a minimum on the downstream side of the mountain. This lateral shift with respect to the mountain top happens when topography excites mostly wave modes k that are in the propagating wave regime ($l^2 > k^2$) for which the pressure perturbations are not symmetric about the crest, see Fig. 1.2c. The strongest negative pressure gradient force is therefore

found further in the lee of the obstacle as compared to the bluff-body separation case. The pressure perturbation (1.15) at the surface then becomes

$$p_s = \rho_0 m U^2 H \sin(-kx) \quad , \tag{1.27}$$

and has a minimum in the lee ($k < 0$ and $m < 0$), shifted by $\pi/2$ to the wave crest (cf. displacement d and pressure p in Fig. 1.2c). The wave-induced pressure-gradient force at the surface becomes

$$-\frac{1}{\rho_0}\frac{dp_s}{dx} = mkU^2 H \cos(-kx) \quad , \tag{1.28}$$

and is strongest at the foot of the mountain (minimum of d in Fig. 1.2c). The separation points are therefore located underneath the troughs of the wave and rotor formation occurs downstream of it underneath the wave crests. It becomes clear from Equation (1.28), that both k and $m = -(l^2 - k^2)^{1/2}$ must be large in order to observe strong deceleration in the lee. Since $|m|$ reduces with increasing $|k|$, a large Scorer parameter is necessary for both wave numbers to be large. From these elaborations, it can be concluded that flows must be sufficiently nonlinear ($NH/U \gtrsim 1$) in order to observe wave-induced flow separation. However, large NH/U is not sufficient because the horizontal pressure gradient force (Equation 1.28) also scales with U^2 and, therefore, considerable wind speed is necessary for separation.

The following sections give a brief overview of the most important studies on wave-induced BLS of the recent years (see also the historical overview in section 1.1) grouped by the different wave types presented in section 1.2.

Internal gravity waves in uniformly stratified flow

After the discovery of trapped lee waves by Scorer (1949), rotors were mainly attributed to the existence of resonant lee waves (see next section). Boundary-layer separation in uniformly stratified flows, as was studied by Lyra (1943) and Queney (1948), was reexamined much later by Baines and Hoinka (1985) and Baines (1995). They carried out water tank experiments and grouped the observed flows in a regime diagram for (i) no separation, (ii) bluff-body separation and (iii) wave-induced separation (see Fig. 1 in chapter 2). They found wave-induced separation to occur when $NH/U \gtrsim 1$. This value has been confirmed later by means of linear theory by Ambaum and Marshall (2005). A complementary set of numerical simulations has been carried out in this thesis in chapter (2) and largely confirms the regime transitions in the diagram by Baines (1995). Similar results have been obtained also in a recent study by Prestel and Wirth (2016).

Numerical simulations have been used also in Zängl (2003) to show that nonhydrostatic vertically-propagating mountain waves can be strong enough to trigger rotor formation. A short time later, rotors were also found in the hydrostatic flow regime by Jiang et al. (2007) who showed that linear theory alone cannot explain their formation. Another related study considering uniformly stratified flows has been carried out by Smith and Skyllingstad (2009) to investigate the impact of surface heating on rotors.

A common observation in all these studies is that rotor formation is directly linked to wave breaking in the hydrostatic mountain wave. It is interesting to note that the width of the rotors λ_r can be estimated accurately with the horizontal wavelength of the most nonhydrostatic wave mode $\lambda_r = 2\pi U/N$, as is shown in the comparison with the observed wavelength λ_{sim} in the simulations

Publication	N [s^{-1}]	U [m s^{-1}]	λ_{sim} [km]	λ_r [km]
Zängl (2003), Fig 12a–b	0.01	10	6	6.2
Jiang et al. (2007)	0.01	10	7	6.2
Smith and Skyllingstad (2009)	0.015	5	2	2.1

In the case of Zängl (2003) this is probably not surprising because the mountain wave regime is intrinsically nonhydrostatic ($k^2 \lesssim N^2/U^2$) and the horizontal wavenumber approximately equal to the Scorer parameter $l = N/U$. However, the good agreement of the latter studies, in which the flow is hydrostatic ($l^2 \gg k^2$), is contrary to expectations because hydrostatic waves are typically of large wavelength and rotors should exhibit much longer wavelength than that of the nonhydrostatic wave mode. This apparent contradiction is further explored in this thesis, specifically in section (2.4).

Resonant lee waves

Numerical simulations of boundary-layer separation and rotor formation forced by resonant lee waves were carried out firstly by Doyle and Durran (2002). Their two-dimensional simulations confirmed Lyra's (1943) statement that the wave-induced horizontal pressure gradient force at the surface is the driving mechnism for rotor formation. The rotors forming underneath the simulated wave crests correspond to the early schematics by Holmboe and Klieforth (1957) with a single vortex tube underneath the wave crests, see Fig. 1.4a. However, a later study by Doyle and Durran (2007) employing high-resolution three-dimensional simulations revealed a considerably higher complexity of the rotor structure with small scale sub-vortices in the rotor interior due Kelvin-Helmholtz instability along the upstream shear line, see Fig. 1.4b.

Other investigations of resonant-lee-wave-induced BLS were mostly carried out in real-case studies, for example in the Sierra Nevada mountains (e.g. Grubišić and Billings, 2007; Stiperski and Grubišić, 2011; Sheridan and Vosper, 2012) and the Alps (Doyle and Smith, 2003). All these studies show that trapped lee waves are an important mechanism for boundary-layer separation and rotor formation.

Interfacial lee waves

Another important type of waves causing BLS are interfacial waves, which may play a key role for rotor formation during Bora events (e.g. Belušić et al., 2007; Gohm et al., 2008; Grisogono and Belušić, 2009). As mentioned earlier in the overview of interfacial wave theory (section 1.1), Vosper (2004) was among the first to study the effects of inversions

on rotor formation. His numerical simulations of two-layer flow (according to Fig. 1.3b), covering a parameter space spanned by the Froude number $Fr = U/(g'h_1)^{1/2}$ and nondimensional mountain height H/h_1, showed different flow responses in the lee. It is apparent from Vosper's simulations that hydraulic jumps form only for Fr below a certain threshold. For Fr greater than this threshold, laminar nonhydrostatic lee waves develop at the interface and wave-type rotors may form underneath the wave crests if the obstacle is sufficiently high.

Only few studies to date have focused on conditions favorable for hydraulic-jump-type rotors, which are considered to be most intense. Among them are investigations by Hertenstein and Kuettner (2005) and Hertenstein (2009) on wave-type- and hydraulic-jump-type rotors. They attribute the flow response type mainly to spanwise vorticity η in the inversion layer with wave-type rotors occurring for ($\eta > 0$) and hydraulic-jump-type rotors for ($\eta \lesssim 0$). In their study, they control vorticity in the inversion layer by systematically varying wind speed above the inversion in the upstream conditions. However, they disregard the fact that changing the absolute value of wind speed also affects the wavelength of the wave disturbance in the lee and thus the wave steepness, which has a large impact on the breaking of waves. In fact, hydraulic jumps occur also in the simulations with uniform upstream flow speed $\eta = 0$ in Vosper (2004). This suggests, that other factors might be equally important for the flow response type, as will be further investigated in chapter (4).

1.4 Scope of this work

The major goal of this thesis is to advance the knowledge of the dynamics of wave-induced rotor formation. Herein, the focus lies on the relatively unexplored cases of rotor formation induced by (i) vertically propagating internal gravity waves and (ii) interfacial lee waves. In particular, four research questions are addressed in this thesis.

Internal gravity waves

1. What flow condition leads to the largest (vertical extent) and strongest rotors?
   Baines (1995) showed that wave-induced rotors occur when $NH/U \gtrsim 1$. However, it has not been clarified yet under what flow conditions the rotors become particularly strong and large.

2. What is the origin of rotors in hydrostatic flows?
   Rotors are a nonhydrostatic phenomenon because they are typically narrow and feature strong vertical motion. Therefore, they are expected to occur in nonhydrostatic flows. However, rotors have been found to develop also in near-hydrostatic flows (Jiang et al., 2007) and their origin is still unclear.

Interfacial lee waves

1. Is it possible to determine the wavelength and amplitude of interfacial lee waves from the upstream flow parameters?
   From scaling arguments, it can be expected that the wavelength and amplitude of interfacial waves can be expressed in terms of governing nondimensional flow parameters. Systematic analytical studies investigating the influence of the upstream flow parameters on the wavelength are still lacking. A previous study by Vosper (2004) showed that interfacial wave theory is relatively accurate in predicting the wavelength, but inaccurate for amplitude predictions. Therefore, investigations of the amplitude require alternative approaches because nonlinear effects are important.

2. Can the flow response (lee waves or hydraulic jumps) downstream of a mountain be inferred from the upstream flow profile?
   Numerical simulations in Vosper (2004) revealed that a threshold Froude number exists (depending on the nondimensional mountain height) which separates the hydraulic jump regime from the lee wave regime. The precise conditions for which hydraulic jumps can be expected instead of laminar lee waves have not been identified analytically yet.

Chapter 2

Dynamics of rotor formation in uniformly stratified two-dimensional flow over a mountain

This chapter presents the results of investigations of rotor formation in uniformly stratified flows over a two-dimensional mountain ridge. The main aims of the study were to: (i) identify the flow regime which gives rise to the largest and strongest rotors, (ii) investigate the coupling between wave amplitudes and rotor properties and (iii) shed light on the rotor formation process in hydrostatic flows.

The author contributed to the layout of this study and to the numerical experiment design. Furthermore, he performed the simulations, analyzed the model output and carried out the theoretical analysis of the wave forcing. Also, the author prepared all figures and contributed to the interpretation of the results and the writing of the text.

This paper is published in the Quarterly Journal of the Royal Meteorological Society:
Sachsperger, J., S. Serafin, and V. Grubišić, 2016a: Dynamics of rotor formation in uniformly stratified two-dimensional flow over a mountain. *Q. J. R. Meteorol. Soc.*, **142**, 1201–1212

Quarterly Journal of the Royal Meteorological Society Q. J. R. Meteorol. Soc. 142: 1201–1212, April 2016 A DOI:10.1002/qj.2746

RMetS
Royal Meteorological Society

Dynamics of rotor formation in uniformly stratified two-dimensional flow over a mountain

Johannes Sachsperger,[a]* Stefano Serafin[a] and Vanda Grubišić[b,†]
[a]*Department of Meteorology and Geophysics, University of Vienna, Austria*
[b]*National Center for Atmospheric Research[‡], Boulder, CO, USA*

*Correspondence to: J. Sachsperger, Department of Meteorology and Geophysics, University of Vienna, Althanstraße 14 UZA2, 1090 Vienna, Austria. E-mail: johannes.sachsperger@univie.ac.at
[†]Additional affiliation: Department of Meteorology and Geophysics, University of Vienna, Austria
[‡]The National Center for Atmospheric Research is sponsored by the National Science Foundation

The coupling between mountain waves in the free atmosphere and rotors in the boundary layer is investigated using a two-dimensional numerical model and linear wave theory. Uniformly stratified flow past a single mountain is examined.

Depending on background stratification and mountain width, different wave regimes are simulated, from weakly to strongly nonlinear and from hydrostatic to non-hydrostatic. Acting in conjunction with surface friction, mountain waves cause the boundary layer to separate from the ground, causing the development of atmospheric rotors in the majority of the simulated flows.

The rotors with largest vertical extent and strongest reverse flow near the ground are found to develop when the wave field is nonlinear and moderately non-hydrostatic, in line with linear theory predictions showing that the largest wave amplitudes develop in such conditions. In contrast, in near-hydrostatic flows boundary-layer rotors form even if the wave amplitude predicted by linear theory is relatively small. In such cases, rotors appear to be decoupled from the wave field aloft by low-level wave breaking. In fact, rotor formation is caused by short-wavelength modes propagating horizontally along an elevated and stably stratified jet below the neutrally stratified wave-breaking region. Once formed, atmospheric rotors trigger non-hydrostatic wave modes that can penetrate through the finite-depth neutral layer above the jet and propagate into the free atmosphere.

In all simulated cases, non-hydrostatic effects – i.e. sharp vertical accelerations – appear to be essential for rotor formation, regardless of the degree of hydrostaticity in the primary wave field.

Key Words: atmospheric rotors; boundary-layer separation; wave breaking; mountain wave; rotor streaming; uniformly stratified flow

Received 22 October 2015; Revised 13 January 2016; Accepted 15 January 2016; Published online in Wiley Online Library 17 March 2016

1. Introduction

Boundary-layer separation (BLS) may occur when a strong adverse pressure-gradient force in the outer flow acts on the boundary layer and brings the underlying fluid to rest (e.g. Batchelor, 1967; Scorer, 1997). In the case of flow over topography, BLS can occur in different scenarios. Over very steep obstacles, the boundary-layer flow normally separates directly at the top. This is often observed in flow past sharp mountains, e.g. in the case of banner cloud formation (Wirth *et al.*, 2012). Over more gently sloped obstacles, strong adverse pressure gradients can also be generated downstream of the obstacle top if the flow is stably stratified and large-amplitude gravity waves are present. BLS is said to be 'post-wave' or 'wave-induced' in this case (Baines, 1995).

Atmospheric rotors are a potentially hazardous phenomenon, closely related to BLS, which may occur downstream of the location where the boundary layer is lifted off the surface, i.e. the separation point (Doyle and Durran, 2002). Rotors are zones within the boundary layer with strong turbulence, large values of spanwise vorticity and neutral stability. Their turbulent nature makes atmospheric rotors dangerous for general aviation and road traffic (Förchtgott, 1957; Keller *et al.*, 2015). A sequence of

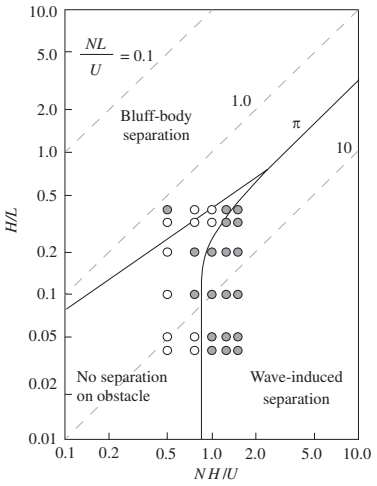

Figure 1. Dependence of boundary-layer separation regimes on the vertical aspect ratio of the mountain, H/L, and on the nonlinearity parameter, NH/U (adapted from Baines, 1995). Dashed lines show values of the hydrostaticity parameter NL/U. Solid lines delimit the three BLS regimes. Dots represent our numerical experiments with small roughness length ($z_0 = 0.001$ m). Grey shading indicates that BLS occurs, as detected by the presence of reversed flow in the lee of the obstacle.

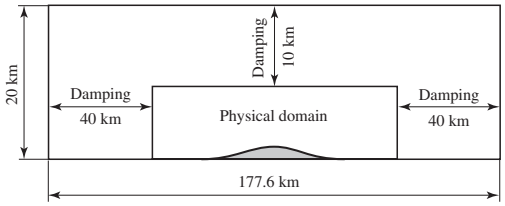

Figure 2. Sketch of the simulation domain.

rotors may form if the mountain wave features multiple wave crests in the horizontal direction. This phenomenon is known as *rotor streaming* (Förchtgott, 1957) and implies that a fraction of the wave energy released by flow over a mountain has to be trapped in a wave duct.

One of the first systematic studies of BLS in stratified flows was reported by Baines and Hoinka (1985), who characterized the dependence of BLS on the governing flow through a series of water tank experiments. According to their results, a few parameters describing the flow and the obstacle shape appear to be sufficient in order to determine whether BLS occurs or not. These are the buoyancy frequency N, the ambient wind speed U and the mountain height H and half-width L, which can be combined in the non-dimensional groups NH/U (nonlinearity parameter), NL/U (hydrostaticity parameter) and H/L (vertical aspect ratio of the obstacle). Depending on NH/U and NL/U, the flow regime can range from linear to nonlinear and from non-hydrostatic to hydrostatic. A detailed discussion on the impact of these parameters on flow over mountains is provided by Smith (1979) and Nappo (2012).

The results of the experiments by Baines and Hoinka (1985) are summarized in Figure 1 (adapted from Baines, 1995), where three distinct regimes are indicated: (i) bluff-body BLS, (ii) wave-induced BLS and (iii) no BLS. Bluff-body BLS occurs in near-neutral non-hydrostatic flows over relatively narrow peaks. Wave-induced BLS, conversely, occurs more easily when the flow is closer to the hydrostatic limit. Also, a certain degree of nonlinearity is necessary for the mountain wave to impose a sufficiently strong adverse pressure-gradient force at the surface. Ambaum and Marshall (2005) explained the transitions between the three separation regimes with a simple linear analytical model.

Early studies on wave-induced BLS only considered scenarios with constant N and U. However, considerably higher complexity can result from variations of these parameters with height, an issue that has been studied mostly by means of numerical simulations. Doyle and Durran (2002) confirmed that surface friction and a sufficiently large pressure gradient are necessary conditions for rotor formation beneath trapped lee waves. Hertenstein and Kuettner (2005) investigated the impact of elevated inversions and shear layers on atmospheric rotors and found that, depending on the dynamics of vorticity along the inversion, either lee-wave type or hydraulic-jump type rotors may occur, the latter being more severe than the former. Vosper (2004) used numerical simulations to assess the impact of the strength and height of an inversion on the downstream flow. Considering a constant upstream wind profile, he showed that the leeside flow can feature either a hydraulic jump or trapped lee waves (depending on the Froude number of the incoming flow), with or without rotor formation (depending on the height of the inversion relative to the mountain height). Jiang *et al.* (2007) focused on the hydraulic-jump regime and categorized different types of flow adjustment depending on the shallow-water Froude number and on NH/U.

Other studies explored BLS and rotor formation under real-case conditions, e.g. over the Sierra Nevada (USA; Grubišić and Billings, 2007; Sheridan and Vosper, 2012; Strauss *et al.*, 2015a), the Dinaric Alps (Croatia; Gohm *et al.*, 2008) and the Medicine Bow Mountains (USA; French *et al.*, 2015; Strauss *et al.*, 2015b). All these investigations show that rotor formation and cessation is very complex in reality, due to the interaction between diabatic processes, turbulence, transient atmospheric conditions and orography. They also show that the amplitude of mountain waves is among the most important factors in determining the severity of BLS and rotor formation.

Only a few numerical studies to date have focused on BLS in the seemingly simple case of uniformly stratified flow (i.e. with N and U constant with height) over mountains. These include the contributions by Zängl (2003) on BLS in flows close to the non-hydrostatic limit, by Smith and Skyllingstad (2009) on the rotor formation process in conjunction with surface heating and cooling and by Jiang *et al.* (2007) on BLS caused by large-amplitude hydrostatic mountain waves.

In this work, we explore rotor formation in a uniformly stratified atmosphere with a constant upstream wind profile to identify the flow regimes that lead to the highest (largest vertical extent) and strongest (largest reversed flow) rotors. To our knowledge, this issue has not been addressed systematically so far. We concentrate on the same parameter space explored by Baines (1995) and study in detail the ranges $0.5 < NH/U < 1.5$ and $0.04 < H/L < 0.4$, where relatively small variations in the governing parameters can generate considerably different flow responses. In our analysis, we make use of two-dimensional nonlinear numerical simulations and a linear semi-analytical model based on the Taylor–Goldstein equation (Nappo, 2012).

The article is organized as follows. Section 2 gives a brief overview of the numerical model and the set-up of simulations. Numerical results are presented in section 3. The discussion in section 4 relies on linear theory and describes the impact of NH/U and H/L on the rotor height and strength. The occurrence of rotor streaming in near-hydrostatic and highly nonlinear flows is also discussed. Conclusions are drawn in section 5.

2. Numerical model and experimental design

Numerical experiments are carried out using the Bryan Cloud Model (CM1: Bryan and Fritsch, 2002; Doyle *et al.*, 2011). CM1 is a fully compressible, nonlinear and non-hydrostatic large-eddy simulation model. Turbulent stresses and turbulent scalar fluxes are parametrized after Deardorff (1980). The model equations are

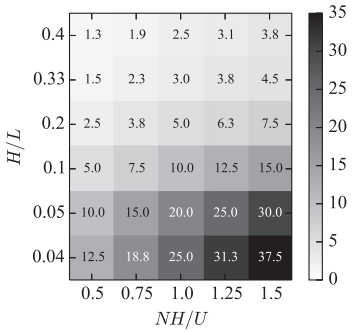

Figure 3. Values of the hydrostaticity parameter NL/U in our simulations.

integrated with a third-order Runge–Kutta time-split scheme and a fifth-order advection scheme in both the horizontal and vertical directions. In addition to the numerical diffusion implicitly provided by the advection scheme, sixth-order artificial diffusion in the horizontal and vertical directions is added in our simulations to prevent the onset of nonlinear numerical instability.

The numerical set-up is identical for all simulations. The two-dimensional domain consists of 3552×123 grid points in the x and z directions respectively (see Figure 2). The horizontal grid spacing is constant and equal to $\Delta x = 50$ m and the vertical grid spacing stretches from $\Delta z = 10$ m at the ground to $\Delta z = 200$ m at $z = 5$ km and remains then constant until the model top. This corresponds to a domain length of 177.6 km and a depth of 20 km. A mountain is located in the centre of the domain. In analogy with Baines and Hoinka (1985), the topography is specified as

$$h(x) = \begin{cases} \frac{H}{2}\left[1 + \cos\left\{\frac{\pi}{L}(x - x_0)\right\}\right] & \text{if } |x - x_0| < L \\ 0 & \text{elsewhere,} \end{cases}$$

where $x_0 = 88.8$ km is the location of the mountain top and $H = 1000$ m is the mountain height. The mountain half-width, L, differs in each run (see below).

A Rayleigh damping layer above $z = 10$ km minimizes reflections at the upper boundary, where a rigid-lid condition is enforced. Boundary conditions at the inflow and outflow boundaries are open-radiative, with a 40 km wide Rayleigh damping zone at each of the boundaries to prevent the reflection of outward-moving disturbances. The physical domain, i.e. the part of the domain where no damping is applied, extends over the ranges $40 < x < 137.6$ km and $0 < z < 10$ km, covering a large part of the region downstream of the mountain where rotor formation is expected.

The initial model state is hydrostatically balanced and continuously stratified (with constant N). The surface potential temperature and surface pressure are set, respectively, to $\theta_s = 300$ K and $p_s = 1000$ hPa. The incoming flow speed U is constant with height and increases from zero to a nominal value ($10\ \mathrm{m\,s^{-1}}$) in the first simulation hour. This procedure minimizes spurious effects triggered by the impulsive start of the model integration. The total integration time is 3.3 h (200 min) for all simulations.

The parameter space covered in this study is spanned by $NH/U \in \{0.5, 0.75, 1, 1.25, 1.5\}$ and $H/L \in \{0.04, 0.05, 0.1, 0.2, 0.33, 0.4\}$. Accordingly, NL/U varies from 1.25–37.5 (Figure 3). Consequently, the flow regimes under examination range from weakly to moderately nonlinear and from non-hydrostatic to approximately hydrostatic. This parameter space covers the central part of the regime diagram by Baines (1995), shown in Figure 1.

Three different sets of simulations were performed, with free-slip conditions at the lower boundary and quasi-no-slip conditions over smooth ($z_0 = 0.001$ m) and rough ($z_0 = 0.1$ m) surfaces, respectively. In free-slip simulations, surface stresses are set to zero, whereas in quasi-no-slip runs they are parametrized using a drag relationship. In the latter case, the drag coefficient depends on the roughness length z_0 as prescribed by similarity theory. The majority of the results presented in this article refer to simulations in which z_0 has a value appropriate for most natural surfaces ($z_0 = 0.1$ m). The set of simulations with $z_0 = 0.001$ m was performed specifically for the purpose of comparison with laboratory experiments (Baines and Hoinka, 1985; Baines, 1995) that made use of smooth obstacles.

Keeping the mountain height $H = 1000$ m and the incoming flow speed $U = 10\ \mathrm{m\,s^{-1}}$ fixed for all simulations, the desired values of NH/U and H/L were achieved by setting $N \in \{0.005, 0.0075, 0.01, 0.0125, 0.015\}\ \mathrm{s^{-1}}$ and $L \in \{25, 20, 10, 5, 3, 2.5\}$ km. Combining five values of N, six of L and three of z_0 results in a total of 90 experiments.

A quasi-steady simulation stage is reached between the end of the model spin-up (1 h) and the onset of nonlinear interactions of the mountain-wave field (Nance and Durran, 1998). In the set of simulations with $z_0 = 0.1$ m, the length of this period varies from 20 min ($NH/U = 1.5$ and $H/L = 0.4$) to 140 min ($NH/U = 0.5$ and $H/L = 0.4$). We determine the quasi-steady phase for each simulation by measuring abrupt changes in the surface wind speed downstream of the mountain, using the root-mean-square deviation (RMSD) between adjacent output times. The first significant peak of RMSD indicates a strong sudden change of the surface wind field and thus the beginning of the non-stationary phase.

The simulations presented in this study consider domains with two spatial dimensions (x and z). Simulating atmospheric flow in 2D has proved very effective in studying the properties of mountain waves and related phenomena in weakly to moderately nonlinear regimes, even when turbulent mixing – an inherently 3D process – may result from boundary effects or from the release of instabilities (e.g. Doyle and Durran, 2002; Hertenstein and Kuettner, 2005). Doyle and Durran (2007) have shown that, even if the turbulence structure in the interior of atmospheric rotors is largely dependent on vortex tilting and stretching, the defining characteristics of a rotor (e.g. vertical and horizontal extent, surface pressure gradient) remain quantitatively unaltered even if the flow is constrained to 2D. Our preliminary comparisons between runs with two-dimensional and three-dimensional domains in a limited number of cases showed differences only in regions where mixing occurs; most distinctively in the rotor region; see the example presented in Figure 4. In the three-dimensional simulation (Figure 4(b)), the reversed flows are weaker (spanwise vorticity in the surface layer is largely positive), while the vortex structure of the rotors is more turbulent (less coherent) compared with the corresponding two-dimensional simulation (Figure 4(a)). This suggests that large parts of the kinetic energy (KE) of the reversed flow within the rotor are converted into turbulent kinetic energy (TKE) when 3D turbulence is allowed to develop. This conversion of energy happens through vortex tilting and stretching (Doyle and Durran, 2007), significantly weakening the reversed flow. Flow regimes that lead to the strongest rotors in two-dimensional flow can, therefore, be expected to lead to the most turbulent rotors in three-dimensional flow.

3. Results

3.1. *Free-slip simulations: flow regimes*

We begin by investigating how mountain-wave activity responds to changes in nonlinearity and mountain width when free-slip conditions are imposed at the ground. Such flows are less prone to flow separation than those over a rough surface, because the wave-induced deceleration has to overcome stronger near-surface winds. In fact, in none of our free-slip experiments is the wave activity strong enough to trigger lee-side flow

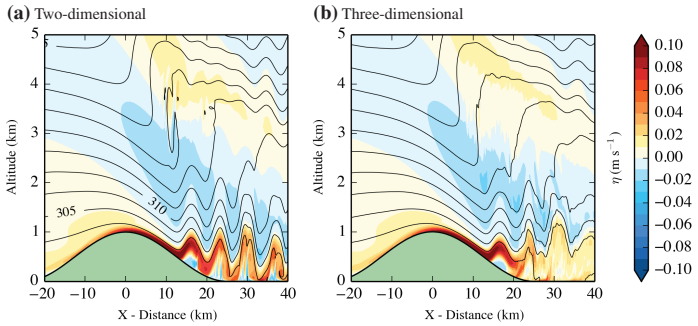

Figure 4. Three-dimensional effects on the flow field with $NH/U = 1.25$, $H/L = 0.04$ and $z_0 = 0.1$ m. The panels show spanwise vorticity η at $t = 180$ min for (a) two-dimensional flow and (b) three-dimensional flow. The setup of the 3D simulation is identical to that of the 2D simulation (see section 2) except for the spanwise extent of the domain (7.2 km with $\Delta y = \Delta x = 50$ m). The values in cross-section (b) represent a spanwise average of η.

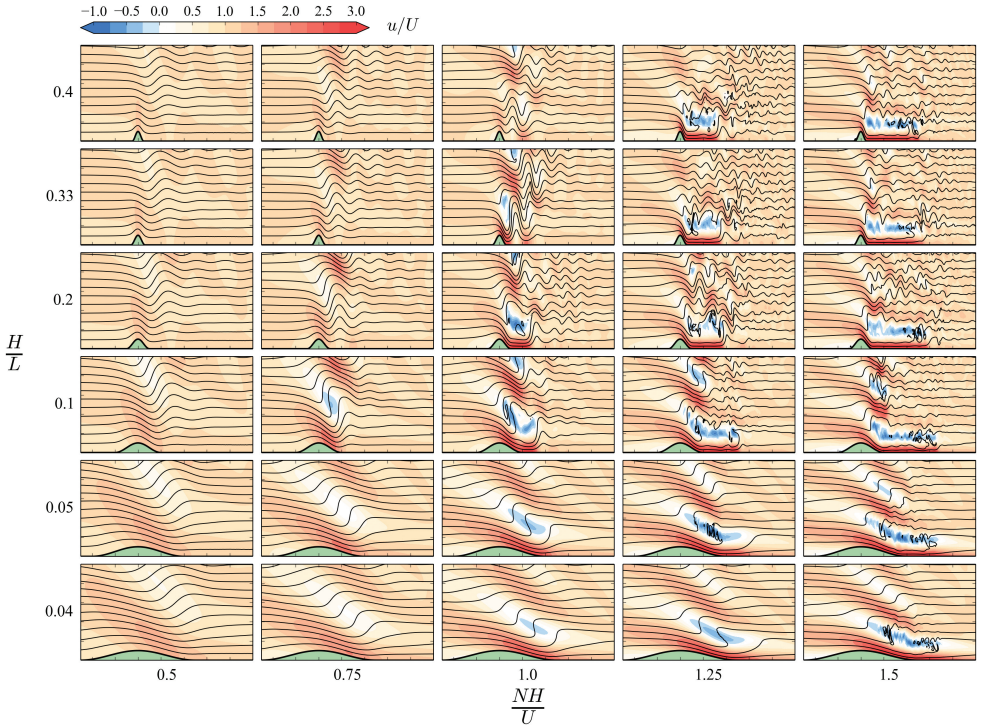

Figure 5. Cross-sections of normalized horizontal wind speed u/U derived from free-slip simulations at $t = 150$ min. Blue colours indicate reversed flow. Each panel shows the subdomain corresponding to $z \in [0, 10]$ km (y axis) and $x \in [-25, 50]$ km (x axis, origin at the mountain top). Isentropes are displayed in all panels to illustrate wave motion. Because N increases from the left column to the right, variable contour intervals are used (from left to right: 0.7, 1.6, 2.9, 4.7, 7.0 K).

separation. Therefore, the results of this section are expected to be more easily comparable with those from well-known analytical mountain-wave models, where similar lower boundary conditions are adopted.

In Figure 5, vertical cross-sections of non-dimensional horizontal wind speed, u/U, are shown for all combinations of NH/U and H/L. In the bottom row ($H/L = 0.04$), the effect of increasing nonlinearity is clearly evident in the increase of the horizontal wind-speed perturbation, $u'/U = u/U - 1$. Isentropes at the height of the first wave crest start to overturn for values of $NH/U \gtrsim 0.75$, leading to wave breaking (i.e. overturning isentropes and $u/U < 0$), with a downslope windstorm developing underneath. This is consistent with the results of Miles and Huppert (1969), who used Long's (1953) model to estimate a critical value of $NH/U = 0.85$ for wave breaking over bell-shaped topography.

For $NH/U = 0.5$, increasing H/L (and consequently decreasing NL/U) shifts the wind-speed maximum upstream towards the mountain top, while non-hydrostatic wave modes become dominant in the wave structure. For $H/L = 0.4$, the pressure disturbance becomes almost symmetric around the mountain and near-surface flow is nearly irrotational, with maximum speed at the mountain top (potential flow).

Strong downslope windstorms, with $u/U > 3$ in the strongest events, are evident in wave-breaking cases. The fronts of the windstorms adjust abruptly to the unperturbed environment and resemble a propagating internal jump, the propagation speed of which is consistent with hydraulic theory estimates

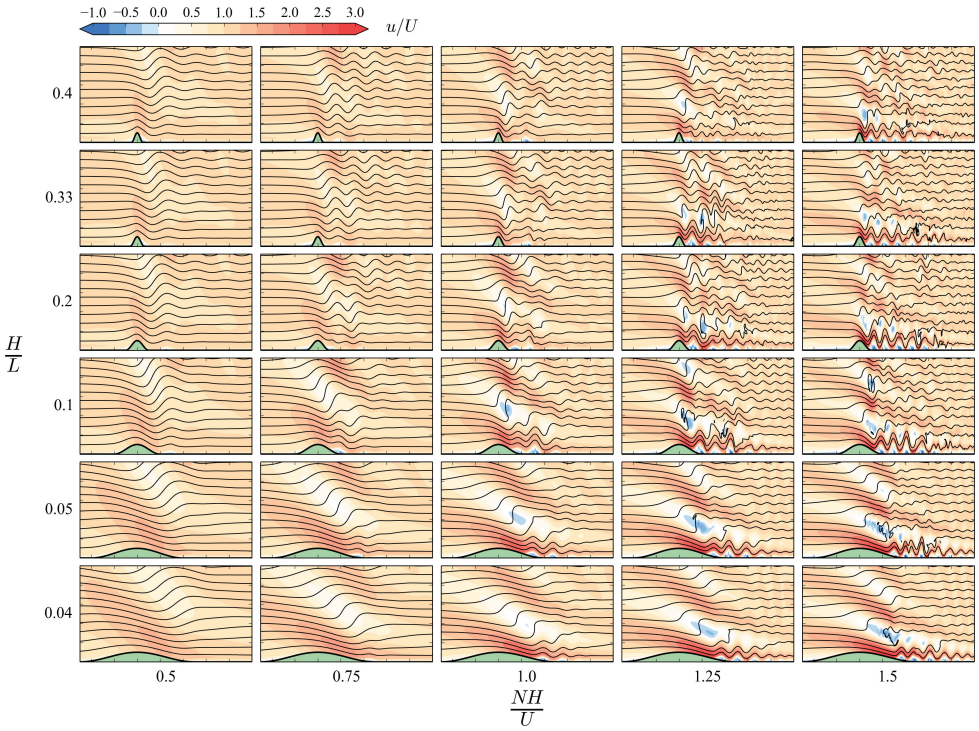

Figure 6. As Figure 5 but for quasi-no-slip lower boundary conditions ($z_0 = 0.1$ m).

(not shown; see Houghton and Kasahara, 1968). At the same time, an upstream-propagating bore on the windward side of the mountain is observed.

When $NH/U = 0.75$, overturning isentropes and reversed flows appear to occur only for $H/L = 0.1$. Also, for larger values of NH/U the wave amplitude appears to be greatest for intermediate values of H/L, ranging between 0.1 and 0.2.

3.2. *Quasi no-slip simulations: flow regimes*

When the flow is subject to friction along the lower boundary, the near-surface wind speed decreases everywhere. The additional deceleration caused by the horizontal pressure gradient induced by the mountain wave can now force the flow to separate from the lower boundary. Figure 6 presents a set of simulations in which a quasi-no-slip boundary condition ($z_0 = 0.1$ m) was applied. The largest differences between the free-slip (Figure 5) and no-slip (Figure 6) simulation results are found downstream of the mountain.

The evidence of BLS is present in all simulations of Figure 6 (see also Figure 7). The reversed flow ($u/U < 0$) strengthens in general with increasing nonlinearity of the flow. In fact, the strength of the reversed flow (downstream of the negative pressure perturbation in the lee of the mountain) is known to depend on the wave-induced pressure-gradient force in the x direction, PGF_x, at the surface (Doyle and Durran, 2002).

The laboratory experiments by Baines and Hoinka (1985) and the linear model by Ambaum and Marshall (2005) suggest that wave-induced BLS occurs for $NH/U \gtrsim 0.8$ for any H/L. In contrast, our corresponding numerical simulations (smooth surface with $z_0 = 0.001$ m) show that BLS is possible even for lower values of NH/U, at least when $H/L \approx 0.1$ (see the grey dots in Figure 1). This is consistent with the findings reported above concerning free-slip simulations, namely that the maximum mountain-wave amplitude for a given value of NH/U is found for $0.1 < H/L < 0.2$. The flow conditions most favourable for BLS and intense rotor formation are identified in section 3.3 below. Evidence from numerical experiments is then interpreted in view of the linear theory of mountain waves in section 4.1.

A unique aspect of no-slip simulations of strongly nonlinear flows is the formation of multiple recirculation regions (atmospheric rotors, Figure 6). As in the free-slip simulations, downslope windstorms develop under strongly nonlinear conditions in response to mountain-wave breaking aloft. However, unlike the windstorms in free-slip simulations, which extend far downstream of the mountain, the windstorms in no-slip simulations separate from the surface and give rise to a sequence of rotors. This process has been referred to as *rotor streaming* (Förchtgott, 1957) and is discussed in depth in section 4.2.

In Figure 7, which presents Hovmöller diagrams of the 10 m horizontal wind speed of our simulations, rotor streaming is evident as a repeating pattern of separation and reattachment (visible as blue streaks downstream of the mountain) in simulations with $NH/U \gtrsim 0.75$. It is apparent that this separation pattern is remarkably persistent over time, even after the onset of nonlinear wave interactions.

3.3. *Rotor height and strength*

In order to understand what flow conditions are conducive to the most intense rotors, we evaluate the height and the strength of recirculation regions related to BLS in all our no-slip simulations ($z_0 = 0.1$ m). We only consider the quasi-steady phase of simulations and identify rotors with an objective method based on their thermal structure.

Due to vigorous parametrized turbulent mixing, the interior of atmospheric rotors is nearly neutrally stratified. The vertical extent of a rotor can therefore be determined from the altitude of the interface between the neutrally stratified rotor and the

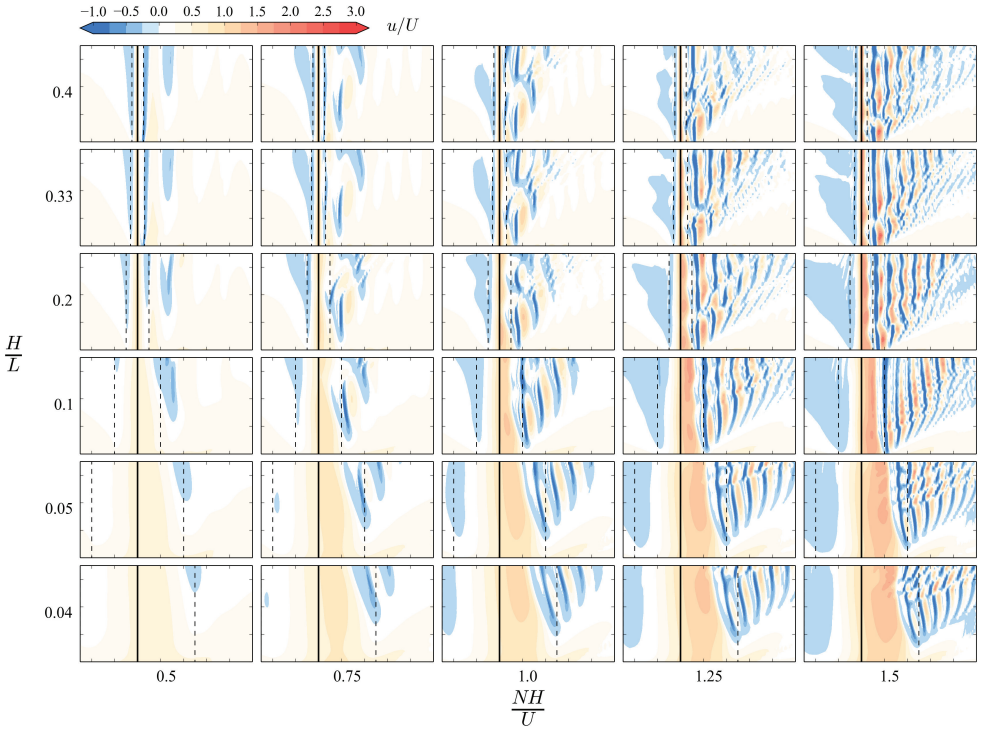

Figure 7. As Figure 5, but showing time–distance diagrams of normalized horizontal wind speed u/U derived from quasi-no-slip simulations ($z_0 = 0.1$ m) at the lowest model level (10 m a.g.l.). Each panel refers to $t \in [60, 200]$ min (y axis) and $x \in [-25, 50]$ km (x axis, origin at the mountain top). Solid vertical black lines in all panels indicate the mountain top, while dashed vertical lines correspond to the foot of the slopes.

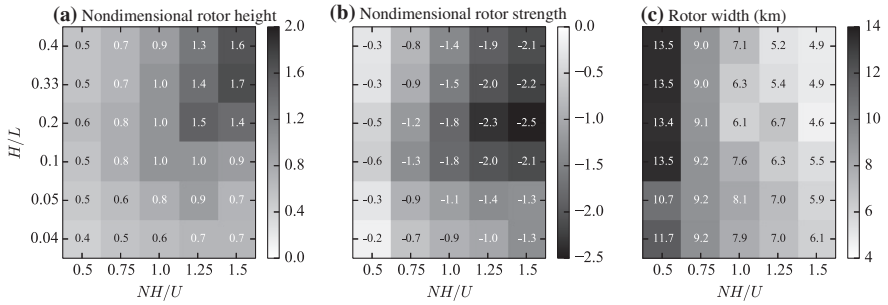

Figure 8. Dependence of (a) non-dimensional rotor height h_r/H, (b) non-dimensional rotor strength $u_{\min}/U$ and (c) width on NH/U and H/L as determined from numerical simulations with $z_0 = 0.1$ m (see text for details).

stably stratified free atmosphere aloft. This transition region is located at the first significant peak in the curvature of the vertical potential temperature profile, proceeding upwards from the ground. The first maximum in the height of the interface, proceeding downstream from the first separation point, identifies the rotor height. The rotor strength is defined as the minimum (largest negative) horizontal wind speed component u in the interior of the rotor, i.e. the strength of the reversed flow. Since the rotor height and strength are time-dependent, in what follows we refer to them as their extreme values within the quasi-steady phase.

Non-dimensional rotor heights h_r/H and strengths $u_{\min}/U$ for the whole set of model runs are reported in Figure 8(a) and (b). Clearly, the most severe rotors in terms of height and strength are found in nonlinear and non-hydrostatic flows. Some of the rotors reach higher than the mountain height, with non-dimensional heights up to $h_r/H = 1.7$, and are more than twice as strong as the incoming flow speed, with non-dimensional reversed flows up to $u_{\min}/U = -2.5$. If 3D turbulence were allowed to develop, the strongest rotors would feature large values of TKE, instead of strong reversed flow. This happens because a large part of the KE in the reversed flow would be converted to TKE in this case (Doyle and Durran, 2007). The severity of the rotors is then related to turbulence and not to the strength of the reversed flow.

In what follows, we demonstrate that the dependence of rotor height and strength on the governing parameters is determined mostly by the mountain-wave field above the boundary layer. In particular, we note that the highest rotors are associated with maxima in the wave-induced vertical velocities and the strongest rotors are closely correlated with the largest flow-opposing horizontal pressure gradient force PGF_x (induced by the wave). The conditions for maxima in w and PGF_x are explained by means of linear mountain-wave theory in section 4.1 below.

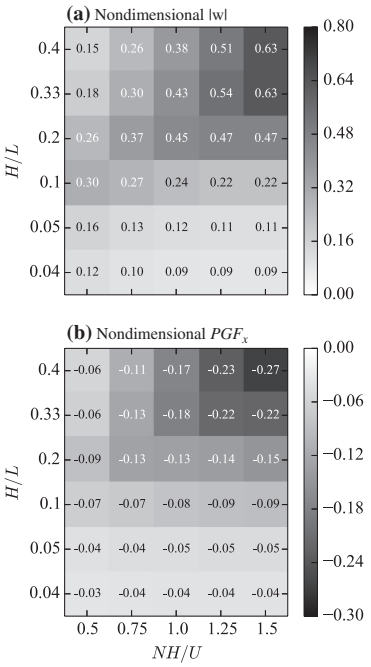

Figure 9. Dependence of wave perturbations on NH/U and H/L as determined from linear mountain-wave theory. The two panels refer to (a) w_{max}/U below $\lambda_{zh} = 2\pi U/N$ and (b) $\min(PGF_x)/(NU)$ at the surface.

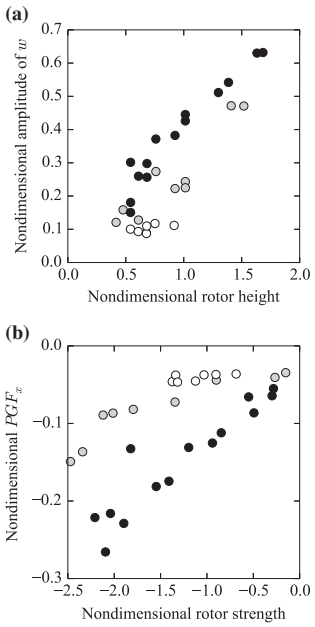

Figure 10. Correlation between numerical simulation output and linear theory results. The two panels refer to (a) h_r/H (x axis) and w_{max}/U (y axis) and (b) u_{min}/U (x axis) and $\min(PGF_x)/(NU)$ (y axis). Marker colours refer respectively to $NL/U < 5$ (black), $5 \leq NL/U < 15$ (grey) and $NL/U \geq 15$ (white).

4. Discussion

4.1. Rotor-wave coupling

The properties of mountain waves have an important influence on the vertical extent and strength of boundary-layer rotors. By comparing the rotor height and strength diagnosed from simulations ($z_0 = 0.1$ m) with linear-theory estimates of the wave amplitude w and PGF_x, we identify the flow regimes in which the rotor properties are most tightly linked to the mountain wave aloft.

In general, linear theory is expected to provide useful predictions only if wave perturbations are small compared with the mean flow speed ($u'/U \ll 1$ or equivalently $NH/U \ll 1$). However, it has been shown in the literature (e.g. Smith (1989) on flow splitting and Ambaum and Marshall (2005) on boundary-layer separation) that linear theory can provide useful guidance for determining orographic flow responses even if the flow regime is nonlinear, at least as long as no irreversible processes such as wave breaking occur. For that reason, we investigate rotor properties only during a time period before the onset of nonlinear interactions in the wave field (see section 2). Therefore, we expect linear theory to provide useful guidance in our context as in the above-mentioned studies.

The linear model we use is based on the solution of the Taylor–Goldstein equation in spectral space (e.g. Nappo, 2012) and is semi-analytical, because it does not require the topography profile to have an exact (closed-form) Fourier transform. Since the transformation to spectral space is performed numerically, any arbitrary topography can be used. Here we adopt the same profile as in the numerical simulations of section 3. A detailed description of the linear model is presented in Appendix A1.

Nondimensional linear estimates of the maximum amplitude of vertical wind-speed perturbations w_{max}/U are shown in Figure 9(a). Values refer to the maximum perturbations found at altitudes below the (hydrostatic) vertical wavelength, $2\pi U/N$. Figure 9(a) should be compared with Figure 8(a), which shows rotor heights diagnosed from numerical simulations. The highest rotors occur in flows where updraughts in the first wave crest are strongest according to linear mountain-wave theory, i.e. in non-hydrostatic flows past relatively steep mountains. Linear theory also suggests that, for a given value of NH/U, the largest vertical wind-speed perturbations do not occur leeward of the steepest mountains, but rather of those with an intermediate value of H/L (Figure 9(a)). The rotor heights diagnosed from numerical simulations generally display the same behaviour (Figure 8(a)). This aspect is discussed more in detail in the Appendix (see section A2).

The linear estimates of the minimum (most negative) values of the non-dimensional surface pressure gradient force, $PGF_x/(NU)$, occurring on the lee side of the mountain (indicating the strongest deceleration, Figure 9(b)) should be compared with the simulated rotor strengths in Figure 8(b). The largest values of $PGF_x/(NU)$ appear in non-hydrostatic and nonlinear flows (high NH/U and low NL/U, Figure 9(b)). Simulated rotor strengths have a similar behaviour, at least in cases where $NL/U \lesssim 5$ (see also Figure 10(b)). Therefore, in this regime, rotors in the boundary layer seem to adjust to pressure perturbations tightly linked to the wave field aloft.

Similar results apply to the horizontal scale of atmospheric rotors. According to linear theory, the dominant non-hydrostatic wave mode corresponds to $k = N/U$ and $\lambda_{nh} = 2\pi U/N$. For the values of NH/U in our parameter space, the corresponding values are $\lambda_{nh} = \{12.5, 8.4, 6.3, 5.0, 4.2\}$ km. In the case of hydrostatic conditions instead, $k \ll N/U$ and thus much longer horizontal wavelengths should be expected (see the Appendix for details).

The rotor widths diagnosed from numerical simulations (e.g. from Figure 7) are shown in Figure 8(c). As expected, they match λ_{nh} very well in non-hydrostatic regimes ($NL/U \lesssim 5$). Contrary to expectations, they have similar values (and not much larger ones) in near-hydrostatic conditions ($NL/U \geq 15$). Atmospheric rotors are not closely related to the wave-induced pressure field in these cases, as shown by the correlation between rotor properties (Figure 8) and the related mountain-wave perturbations (Figure 9) becoming rather poor for $NL/U \geq 15$.

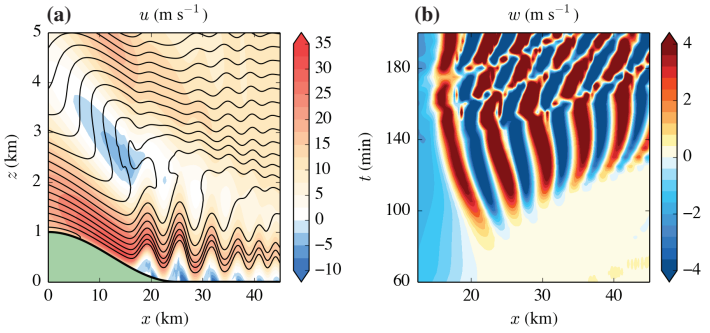

Figure 11. (a) Vertical cross-section of the u wind component at $t = 130$ min in the simulation corresponding to $NH/U = 1.5$ and $H/L = 0.04$. Black contours represent potential temperature at 2 K increments. (b) Hovmöller diagram of the w wind component at $z = 700$ m for the same simulation.

The coupling between the primary mountain wave and the underlying rotors is further elucidated in Figure 10. Non-hydrostatic ($NL/U < 5$) and near-hydrostatic ($NL/U \geq 15$) flow regimes are denoted with black and white circles respectively. A strong coupling of the primary mountain wave with underlying rotors is found for non-hydrostatic flows (black circles). In fact, there are approximately linear relationships between w_{max}/U and rotor height (Figure 10(a)) and between $PGF_x/(NU)$ and rotor strength (Figure 10(b)). In contrast, near-hydrostatic flows (white circles) show a weak coupling between rotors and the mountain wave, since the rotor height and strength are essentially independent of the linear-theory estimates of w_{max} and PGF_x (Figure 10(a) and (b)). Results for intermediate regimes ($5 \leq NL/U < 15$, grey circles) are less immediate to interpret, but generally represent a smooth transition from non-hydrostatic to hydrostatic flow features.

All of these pieces of information, taken together, suggest that low-level atmospheric rotors are essentially decoupled from the wave field aloft for large values of NH/U and NL/U, i.e. when large-amplitude hydrostatic waves are expected to develop. In other words, the formation of atmospheric rotors in conjunction with near-hydrostatic waves ($NL/U \geq 15$) must be a manifestation of nonlinear processes (e.g. wave breaking). This conclusion agrees with a previous study by Jiang *et al.* (2007) and its implications are discussed in greater detail below.

4.2. *Rotor streaming*

Evidence of the occurrence of rotor streaming (i.e. a series of adjacent rotors: Förchtgott, 1957) in our simulations is provided by Figure 7, where Hovmöller diagrams of the near-surface horizontal wind speed for all simulations with $z_0 = 0.1$ m are presented. Pronounced and persistent rotor trains, visible as blue streaks in this figure, develop in simulations where wave breaking occurs ($NH/U \gtrsim 0.75$). This particular flow pattern develops in nonlinear conditions in which the vertically propagating internal gravity waves have large amplitudes and break.

As we show in the following material, the undulations that form below the wave-breaking region can be described reasonably well with a linear model. In other words, we describe rotor streaming as a horizontally propagating secondary wave motion that can develop only when a primary vertically propagating wave motion reaches critical amplitude.

To investigate the mechanisms of rotor streaming in detail, we focus on the most hydrostatic simulation of the set, corresponding to $NH/U = 1.5$ and $H/L = 0.04$. We show that, while the primary wave motion is essentially hydrostatic, the secondary wave motion giving rise to rotor streaming is inherently non-hydrostatic.

A vertical cross-section of the horizontal wind speed and the thermal structure of the flow is presented in Figure 11(a). The elevated jet has a limited vertical extent (< 1 km) and is strongly stratified ($N = 0.03\,\mathrm{s}^{-1}$). The atmosphere in the wave-breaking layer aloft and in the layer of separated air below the jet is neutrally stratified. To a first approximation, this situation can be modelled as a two-layer flow with an inversion of strength $\Delta\theta$ at the interface between the layers. A wave disturbance rides along this interface and creates undulations in the jet, as made evident by the shape of the isentropes at low level. Except for the initial phase, the wave field is quasi-stationary (Figure 11(b)).

The properties of wave motions along interfaces can be concisely described with a frequency dispersion relationship (FDR) between the wavenumber k and the intrinsic frequency Ω. The FDR of waves on an interface of strength $\Delta\theta$ between two neutrally stratified layers (with finite depth H_d below and infinite depth above) is (Sachsperger *et al.*, 2015)

$$\Omega^2 = \frac{g'k}{\coth(kH_d) + 1}, \tag{1}$$

where $g' = g\Delta\theta/\theta_0$ is the reduced gravity. Non-hydrostatic effects are retained in Eq. (1) because no assumptions on the wavenumber have been made. Assuming that the fluid depth is small compared with the wavelength ($kH_d \ll 1$, so that the motion is hydrostatic) would imply $\coth(kH_d) \approx (kH_d)^{-1}$ and therefore the shallow-water FDR $\Omega^2 = g'H_dk^2$. Equation (1) can be derived assuming that the motion is irrotational in both layers of fluid, vorticity being concentrated along the interface (Turner, 1973).

The phase speed of interfacial waves in a fluid moving with speed $\overline{u}$, $c_p = \overline{u} \pm \Omega/k$, is

$$c_p = \overline{u} \pm \sqrt{\frac{g'}{k\,[\coth(kH_d) + 1]}}. \tag{2}$$

Unlike in the special case of shallow water, these waves are dispersive.

The generation of interfacial waves in the rotor-streaming cases can be conceptualized as follows. The lift-off of the downslope flow from the surface, during the BLS process, provides the initial buoyancy perturbation. After detaching from the ground, the head of the jet is subject to free oscillations around its level of neutral buoyancy and consequently generates gravity waves. While the jet head moves downstream, interfacial waves propagate upstream of it; see Figure 11(b). No interfacial waves propagate downstream because the atmospheric structure in that region cannot support this type of motion, given the absence of a density discontinuity. A similar sequence of events might also be important for the development of surface waves on cold pools (Soontiens *et al.*, 2013). In this case, the initial buoyancy perturbation is generated when the downslope flow impinges on the surface of the denser air in the cold pool basin.

Equation (2) suggests that, of all possible wave modes that propagate against the flow, one will be stationary (i.e. such that $c_p = 0$). This corresponds to the root of the transcendental equation:

$$k\overline{u}^2[\coth(kH_d) + 1] - g' = 0. \quad (3)$$

This particular wave mode, continuously excited by the stationary forcing provided by BLS at the bottom of the slope, eventually dominates the flow field between the mountain and the head of the jet. As a result, a sequence of undulations develops, giving rise to rotor formation underneath the wave crests. A rough estimate of the flow properties for the most hydrostatic case in the region downstream of the mountain yields $\Delta\theta = 9$ K ($g' = 0.29\,\mathrm{m\,s^{-2}}$) and $H_d = 700$ m. Hence, the solution of Eq. (3) with a flow speed $\overline{u} = U$ gives a wavelength of 5.3 km, in fairly good agreement with the numerical result (5.7 km).

The close agreement between theory and numerical simulations shows that linear theory is sufficiently accurate in describing rotor streaming. Further support for this idea is provided by the shape of the undulations along the interface. If finite-amplitude effects were important, the shape of the wave disturbance would approach that of a Stokes wave (with wide troughs and narrow crests) due to a superposition of higher harmonics (Turner, 1973). In all rotor-streaming cases, instead, the disturbance remains almost exactly sinusoidal, indicating that finite-amplitude effects are of negligible importance. However, a slight decrease of wave amplitude and wavelength along the interface, from the mountain towards the jet head, is apparent in our simulations. This feature can be attributed either to wave-energy absorption in the boundary layer (Smith *et al.*, 2006), or to wave-energy leakage through the wave-breaking region, as is explained in what follows.

The strongly stratified jet constitutes a wave duct, where wave energy is forced to propagate horizontally. However, as a close inspection of Figures 6 and 11 reveals, vertically propagating wave modes do exist above the interface even in the presence of rotor streaming. This happens because the neutrally stratified wave-breaking layer is not thick enough to damp the amplitude of the interfacial wave perturbation completely. Leakage of wave energy through the neutral wave-breaking layer triggers secondary non-hydrostatic waves in the overlying stably stratified atmosphere (compare the lower right diagrams in Figures 5 and 6). These secondary waves have amplitude comparable to that of the primary mountain wave, in terms of w. The extent to which they affect the large-scale flow in terms of energy and momentum fluxes will be the subject of future investigations.

Overall, these results suggest that atmospheric rotors arise primarily as a consequence of strong vertical accelerations caused by non-hydrostatic wave modes. This conclusion is valid even when the flow upstream of the mountain generates an essentially hydrostatic large-amplitude wave. In this case, rotors arise from non-hydrostatic secondary wave motion on the density interface between the boundary layer and the overlying wave-breaking region.

5. Summary and conclusions

Several aspects of boundary-layer separation induced by mountain waves in vertically uniform stratified flow have been investigated systematically using numerical simulations and linear theory. Flows ranging from weakly to strongly nonlinear and from non-hydrostatic to hydrostatic were considered. Results from numerical simulations are in good overall agreement with previous laboratory experiments (Baines, 1995) and confirm that wave-induced BLS, leading to the formation of atmospheric rotors, is a likely occurrence for $NH/U \gtrsim 0.8$, even if strong inversions or other wave ducts are absent in the ambient flow upstream of the mountain.

The analysis of numerical results also brought a few novel elements to the fore. Firstly, the strongest and highest rotors occur in non-hydrostatic and nonlinear flow conditions. In this flow regime, boundary-layer rotors are strongly coupled with the mountain wave aloft. Linear relationships were found between wave amplitudes (provided by linear theory) and rotor properties (determined from numerical simulations). In fact, the amplitude of the vertical velocity perturbation was shown to be linked with the rotor height and the surface pressure gradient force with the rotor strength. These results are consistent with findings by Doyle and Durran (2002), who used numerical model simulations instead of linear theory to quantify the wave forcing. Generally, the strongest rotors tend to occur in nonlinear flow ($NH/U > 1$) over mountains with vertical aspect ratios between 0.1 and 0.325. These are the conditions where linear mountain-wave theory predicts the largest perturbations to occur.

Secondly, atmospheric rotors may also develop in near-hydrostatic flows (Jiang *et al.*, 2007), but their features cannot be explained by the theory of linear mountain waves in a continuously stratified atmosphere. As is well known, when the mountain-wave amplitude exceeds the limits of linear theory in the hydrostatic regime, a broad wave-breaking region develops right above supercritical flow in the lee of the mountain. We demonstrated that, in these conditions, linear non-hydrostatic hydraulic theory is appropriate to describe the undulations that form along the stably stratified jet underneath the breaking wave. Closed circulations develop in the boundary layer below the crests of this steady secondary wave disturbance, leading to rotor streaming. In analogy to trapped lee waves, rotor streaming is described reasonably well by a linear and non-hydrostatic model of flow in a layered atmosphere. In this case, the key wave-ducting mechanism is related to the presence of a sharp density discontinuity collocated with the jet. These findings are consistent with recent real-case observations of rotor formation in conjunction with a hydrostatic wave-breaking event (French *et al.*, 2015; Grubišić *et al.*, 2015).

Finally, rotor streaming near the surface has a distinctive impact on the atmosphere aloft. Namely, even when the wind speed, stratification and mountain width imply that only a hydrostatic wave would develop right above the mountain, rotor streaming in the lee launches vertically propagating, short-wavelength (non-hydrostatic) wave modes that perturb the flow in the free atmosphere. This process cannot be captured by simple analytical mountain-wave models, where frictional effects, including the possible development of rotors, are typically ignored. Its implications towards wave energy and momentum fluxes still have to be quantified.

Acknowledgements

We thank Peter Baines, Richard Rotunno and Branko Grisogono for many stimulating discussions on boundary-layer separation and interfacial-wave dynamics. We are also grateful to two reviewers and Lukas Strauss for their helpful suggestions, which improved the manuscript. Numerical calculations were performed on the Vienna Scientific Cluster (VSC) and on the computing facilities of the European Centre for Medium-Range Weather Forecasts (ECMWF). NCAR is sponsored by the National Science Foundation. This study was supported by the FWF (Austrian Science Fund) grant P24726-N27 to the University of Vienna.

Appendix A

A1. Linear model description

The Taylor–Goldstein equation in the case of constant wind speed U (e.g. see Nappo, 2012) is

$$\frac{d^2\hat{w}_k}{dz^2} + \left(\frac{N^2}{U^2} - k^2\right)\hat{w}_k = 0. \quad (A1)$$

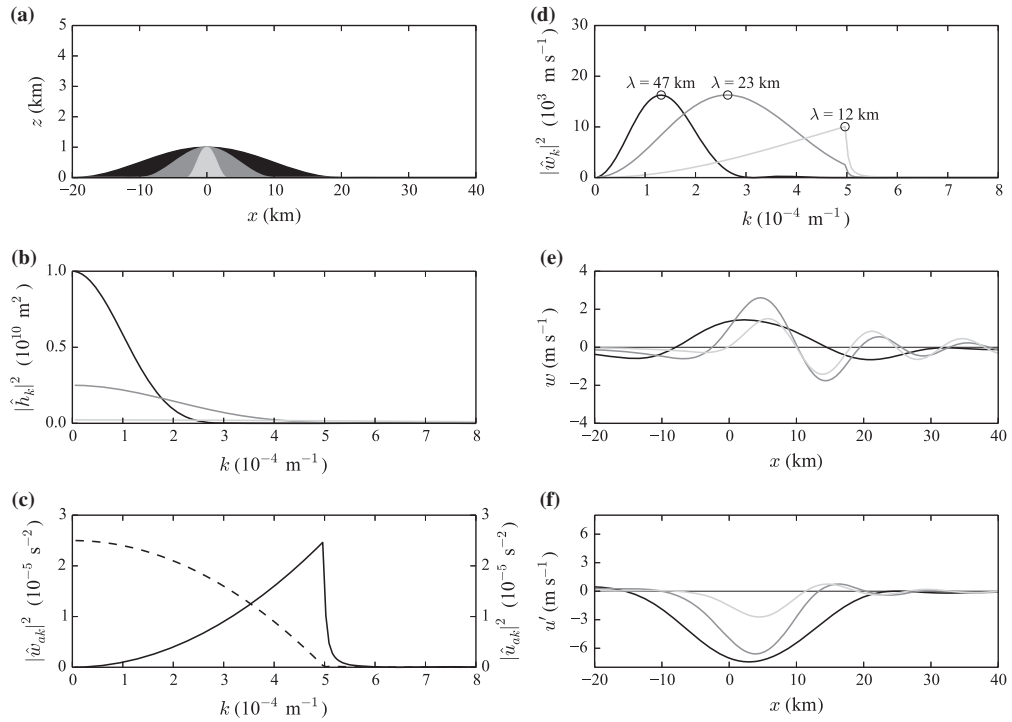

Figure A1. Wave perturbations generated by stratified flow over mountains of different half width. The black, dark grey and light grey topography contours in (a) refer respectively to $L = 20$, 10 and 3 km. Other panels represent the following: (b) power spectra of topography; (c) atmospheric response functions for vertical and horizontal wind-speed perturbations (solid and dashed respectively); (d) spectral power of $\hat{w}_k$ (Eq. (A6)) in flow over the three mountains; (e) vertical wind speed; and (f) horizontal wind-speed perturbation. Numerical values in (c)–(f) assume $N = 0.005\ \mathrm{s}^{-1}$, $U = 10\ \mathrm{m\,s}^{-1}$ and $z = 9$ km ($\approx 3/4\lambda_z$, the approximate height of the wave updraught region).

Here, k is the horizontal wavenumber and $\hat{w}_k$ is an auxiliary variable defined as $\hat{w}_k = [\rho_s/\rho_0(z)]^{-1/2}\,\tilde{w}_k$, where $\tilde{w}_k$ is a generic Fourier mode of the vertical velocity and ρ_s and ρ_0 denote the air density at the surface and the unperturbed density profile, respectively.

The term in brackets in Eq. (A1) represents a vertical wavenumber to the second power, m^2. Both k and $m = -\left(N^2/U^2 - k^2\right)^{1/2}$ are assumed to be negative, as required by the radiation condition appropriate in the case of mountain waves. While k is a real number, m can be imaginary. Equation (A1) describes the propagation of a single internal gravity wave mode that is excited at the bottom boundary. It is valid if the wind speed U and stratification N are uniform in the background flow and the amplitude of the wave disturbance is small. The assumption of small vertical displacements implicitly admits that the Boussinesq and incompressibility approximations are valid and implies that $u'/U \ll 1$.

The resulting wave field of flow over an arbitrary topography profile $h(x)$, with Fourier transform $\hat{h}_k$, can be determined by evaluating the monochromatic solutions of Eq. (A1) for all k,

$$\hat{w}_k(x,z) = -\mathrm{i}kU\hat{h}_k \mathrm{e}^{-\mathrm{i}(kx+mz)}, \tag{A2}$$

over a domain of n horizontal grid points and length $D = n\Delta x$. The full solution is recovered by summing up over all Fourier components:

$$w(x,z) = \left(\frac{\rho_s}{\rho_0(z)}\right)^{1/2} \Re\mathfrak{e}\left[\frac{1}{n}\sum_{k=-2\pi/D}^{0} |\hat{w}_k| \mathrm{e}^{\mathrm{i}\phi_w}\right], \tag{A3}$$

where we have used $\hat{w}_k = |\hat{w}_k|\mathrm{e}^{\mathrm{i}\phi_w}$ and $\phi_w = \tan^{-1}[\Im\mathfrak{m}(\hat{w}_k)/\Re\mathfrak{e}(\hat{w}_k)]$.

Similarly, the horizontal surface pressure gradient force,

$$PGF_x = -\frac{1}{\rho_0}\frac{\partial p}{\partial x}\Big|_{z=0},$$

can be determined from Eq. (A2) using the polarization relation $\hat{p}_k = (m/k)U\rho_0\hat{w}_k$ (Nappo, 2012):

$$PGF_x = \Re\mathfrak{e}\left[\frac{1}{n}\sum_{k=-2\pi/D}^{0} \mathrm{i}mU\hat{w}_k|_{z=0}\right], \tag{A4}$$

where we have dropped the density term because $\rho_s/\rho_0|_{z=0} = 1$.

A2. Optimal mountain aspect ratio for intense mountain-wave development

The linear model described above can be used to identify the flow conditions under which mountain waves have the largest amplitude, in terms of vertical and horizontal wind-speed perturbations.

For convenience, we define

$$\hat{w}_{ak} = -\mathrm{i}kU\mathrm{e}^{-\mathrm{i}(kx+mz)}\ . \tag{A5}$$

It follows from Eq. (A2) that $\hat{w}_k = \hat{h}_k\hat{w}_{ak}$. Similarly, the power spectrum $|\hat{w}_k|^2$ becomes

$$|\hat{w}_k|^2 = |\hat{h}_k|^2|\hat{w}_{ak}|^2. \tag{A6}$$

We refer to $\hat{h}_k$ and $\hat{w}_{ak}$ respectively as the topographic forcing and the atmospheric response for vertical velocity, while $|\hat{h}_k|^2$ and $|\hat{w}_{ak}|^2 = k^2U^2|e^{-imz}|^2$ denote the respective power spectra.

Depending on k and m, the atmospheric response spectrum for the vertical velocity corresponds to

$$|\hat{w}_{ak}|^2 = \begin{cases} k^2U^2 & \text{if } N^2/U^2 > k^2 \ (m^2 > 0, \text{propagating}) \\ k^2U^2|e^{mz}|^2 & \text{if } N^2/U^2 < k^2 \ (m^2 < 0, \text{evanescent}). \end{cases} \tag{A7}$$

Since m is defined as a negative wave number, evanescent solutions vanish with increasing height, as expected.

In analogy, the power spectrum of horizontal velocity perturbations can be expressed as

$$|\hat{u}_k|^2 = |\hat{h}_k|^2|\hat{u}_{ak}|^2, \tag{A8}$$

where u_{ak} is derived from Eq. (A2) and the incompressibility constraint and corresponds to

$$|\hat{u}_{ak}|^2 = \begin{cases} N^2 - k^2U^2 & \text{if } N^2/U^2 > k^2 \ (m^2 > 0, \text{propagating}) \\ (k^2U^2 - N^2)|e^{mz}|^2 & \text{if } N^2/U^2 < k^2 \ (m^2 < 0, \text{evanescent}). \end{cases} \tag{A9}$$

Equations (A6) and (A8) show that vertical and horizontal velocity perturbations induced by flow over an obstacle are the result of the modulation of the topography wave spectrum by the atmospheric response function. Since $|\hat{w}_{ak}|^2$ and $|\hat{u}_{ak}|^2$ are not equal (see Eqs (A7) and (A9)), vertical and horizontal velocity perturbations induced by identical topographic forcing will have a different power spectrum. The concept is clarified in Figure A1, where plots of $|\hat{h}_k|^2$, $|\hat{w}_{ak}|^2$, $|\hat{u}_{ak}|^2$, $\hat{w}_k$ and $\hat{u}_k$ are shown for three mountains of different width.

For the widest of the three mountains (Figure A1(a)), most of the spectral power $|\hat{h}_k|^2$ (Figure A1(b)) is concentrated at low wavenumbers (large wavelengths). In the narrowest mountain, instead, it is almost evenly distributed over a wide range of wavenumbers, but with significantly lower magnitude.

The atmospheric response function for vertical velocity (Eq. (A7)) has a sharp maximum at $k = N/U = 5 \times 10^{-4}\,\mathrm{m}^{-1}$ (solid line in Figure A1(c)). In the case of the wide mountain, there is limited overlap between the spectral powers of the terrain and the atmospheric response (black line in Figure A1(b) and solid line in Figure A1(c)) and the wave mode that gives the largest contribution to the wave amplitude $|w|$ corresponds to $k = 1.3 \times 10^{-4}\,\mathrm{m}^{-1}$, i.e. to $\lambda = 47\,\mathrm{km}$ (black line in Figure A1(d)).

For the narrow mountain, instead, there is a broad region of overlap between the spectra of the terrain and the atmospheric response, but the former has a very low magnitude. The wave amplitude spectrum consequently has a peak at $k = 5 \times 10^{-4}\,\mathrm{m}^{-1}$, i.e. $\lambda = 12\,\mathrm{km}$ (light grey line in Figure A1(d)).

The mountain with intermediate width (dark grey line in Figure A1(d)) corresponds to a condition where the atmospheric response selects a relatively broad range of wavenumbers from relatively strong topographic forcing, with a spectral peak at $k = 2.6 \times 10^{-4}\,\mathrm{m}^{-1}$ ($\lambda = 23\,\mathrm{km}$). This condition maximizes the wave amplitude $|w|$ compared with the two other mountains (Figure A1(e)).

When individual contributions to w from different modes are summed according to Eq. (A3), they may partially compensate each other and cause destructive interference. In all three cases, an evaluation of the phase vectors revealed that the modes have similar phase; hence their interference pattern is mostly constructive (not shown). Therefore, the length of the mountain wave in Figure A1(e) matches approximately the wavenumber of the maximum in the power spectrum in Figure A1(d).

Similar considerations apply to the horizontal wind-speed perturbations. In this case, the atmospheric response is described by Eq. (A9). The maximum response now lies at $k = 0\,\mathrm{m}^{-1}$ (dashed line in Figure A1(c)). Consequently, the largest values of $|u'|$ tend to occur over wide mountains (Figure A1(f)), for which the topographic spectrum has greater power density at low wavenumbers (Figure A1(b)). Even for u', individual wave modes mostly interfere constructively (not shown).

References

Ambaum MHP, Marshall DP. 2005. The effects of stratification on flow separation. *J. Atmos. Sci.* **62**: 2618–2625.

Baines PG. 1995. *Topographic Effects in Stratified Fluids*. Cambridge University Press: Cambridge.

Baines PG, Hoinka KP. 1985. Stratified flow over two-dimensional topography in fluid of infinite depth: A laboratory simulation. *J. Atmos. Sci.* **42**: 1614–1630.

Batchelor GK. 1967. *An Introduction to Fluid Dynamics*. Cambridge University Press: Cambridge.

Bryan GH, Fritsch JM. 2002. A benchmark simulation for moist nonhydrostatic numerical models. *Mon. Weather Rev.* **130**: 2917–2928.

Deardorff JW. 1980. Stratocumulus-capped mixed layer derived from a three-dimensional model. *Boundary-Layer Meteorol.* **18**: 495–527.

Doyle JD, Durran DR. 2002. The dynamics of mountains-wave-induced rotors. *J. Atmos. Sci.* **59**: 186–201.

Doyle JD, Durran DR. 2007. Rotor and subrotor dynamics in the lee of three-dimensional terrain. *J. Atmos. Sci.* **64**: 4202–4221.

Doyle JD, Gaberšek S, Jiang Q, Bernardet L, Brown JM, Dörnbrack A, Filaus E, Grubišić V, Kirshbaum DJ, Knoth O, Koch S, Schmidli J, Stiperski I, Vosper S, Zhong S. 2011. An intercomparison of T-REX mountain wave simulations and implications for mesoscale predictability. *Mon. Weather Rev.* **139**: 2811–2831.

Förchtgott J. 1957. Active turbulent layer downwind of mountain ridges. *Stud. Geophys. Geod.* **1**: 173–181.

French JR, Haimov SJ, Oolman LD, Grubišić V, Serafin S, Strauss L. 2015. Wave-induced boundary-layer separation in the lee of the Medicine Bow Mountains. Part I: Observations. *J. Atmos. Sci.* **72**: 4845–4863, doi: 10.1175/JAS-D-14-0376.1.

Gohm A, Mayr GJ, Fix A, Andreas G. 2008. On the onset of bora and the formation of rotors and jumps near a mountain gap. *Q. J. R. Meteorol. Soc.* **134**: 21–46.

Grubišić V, Billings BJ. 2007. The intense lee-wave rotor event of Sierra Rotors IOP 8. *J. Atmos. Sci.* **64**: 4178–4201.

Grubišić V., Serafin S, Strauss L, Haimov SJ, French JR, Oolman LD. 2015. Wave-induced boundary-layer separation in the lee of the Medicine Bow Mountains. Part II: Numerical modelling. *J. Atmos. Sci.* **72**: 4865–4884, doi: 10.1175/JAS-D-14-0381.1.

Hertenstein RF, Kuettner J. 2005. Rotor types associated with steep lee topography: Influence of the wind profile. *Tellus A* **57**: 117–135.

Houghton DD, Kasahara A. 1968. Nonlinear shallow fluid flow over an isolated ridge. *Commun. Pure Appl. Math.* **21**: 1–23.

Jiang Q, Doyle JD, Wang S, Smith RB. 2007. On boundary layer separation in the lee of mesoscale topography. *J. Atmos. Sci.* **63**: 401–419.

Keller T, Trier S, Hall W, Sharman R, Xu M, Liu Y. 2015. Waves associated with a commercial jetliner accident at Denver international airport. *J. Appl. Meteorol. Climatol.* **54**: 1373–1392.

Long RR. 1953. Some aspects of the flow of stratified fluids: I. A theoretical investigation. *Tellus* **5**: 42–58.

Miles JW, Huppert HE. 1969. Lee waves in a stratified flow. Part 4: Perturbation approximation. *J. Fluid Mech.* **35**: 497–525.

Nance LB, Durran DR. 1998. A modeling study of nonstationary trapped mountain lee waves. Part II: Nonlinearity. *J. Atmos. Sci.* **55**: 1429–1445.

Nappo CJ. 2012. *An Introduction to Atmospheric Gravity Waves* (2nd edn). Academic Press: London, UK.

Sachsperger J, Serafin S, Grubišić V. 2015. Lee waves on the boundary-layer inversion and their dependence on free-atmospheric stability. *Front. Earth Sci.* **3**: 70, doi: 10.3389/feart.2015.00070.

Scorer RS. 1997. *Dynamics of Meteorology and Climate*. Wiley: Chichester, UK.

Sheridan P, Vosper S. 2012. High-resolution simulations of lee waves and downslope winds over the Sierra Nevada during T-REX IOP 6. *J. Appl. Meteorol. Climatol.* **51**: 1333–1352.

Smith RB. 1979. The influence of mountains on the atmosphere. *Adv. Geophys.* **21**: 87–230.

Smith RB. 1989. Mountain-induced stagnation points in hydrostatic flow. *Tellus A* **41**.

Smith CM, Skyllingstad ED. 2009. Investigation of upstream boundary layer influence on mountain-wave breaking and lee wave rotors using a large-eddy simulation. *J. Atmos. Sci.* **66**: 3147–3164.

Smith RB, Jiang Q, Doyle JD. 2006. A theory of gravity wave absorption by a boundary layer. *J. Atmos. Sci.* **63**: 774–781.

Soontiens N, Stastna M, Waite ML. 2013. Numerical simulations of waves over large crater topography in the atmosphere. *J. Atmos. Sci.* **70**: 1216–1232.

Strauss L, Serafin S, Grubišiç V. 2016. Atmospheric rotors and severe turbulence in a long deep valley. *J. Atmos. Sci.*, doi: org/10.1175/JAS-D-15-0192.1.

Strauss L, Serafin S, Haimov S, Grubišić V. 2015b. Turbulence in breaking mountain waves and atmospheric rotors estimated from airborne in situ and Doppler radar measurements. *Q. J. R. Meteorol. Soc.* **141**: 3207–32275.

Turner JS. 1973. *Buoyancy Effects in Fluids*. Cambridge University Press: Cambridge.

Vosper SB. 2004. Inversion effects on mountain lee waves. *Q. J. R. Meteorol. Soc.* **130**: 1723–1748.

Wirth V, Kristen M, Leschner M, Reuder J, Schween JH. 2012. Banner clouds observed at Mount Zugspitze. *Atmos. Chem. Phys.* **12**: 3611–3625.

Zängl G. 2003. Orographic gravity waves close to the nonhydrostatic limit of vertical propagation. *J. Atmos. Sci.* **60**: 2045–2063.

Chapter 3

Lee waves on the boundary-layer inversion and their dependence on free-atmospheric stability

This chapter presents the results of research on the wavelength of lee waves on the boundary-layer inversion. The aims of this study were threefold: (i) to review the most important theoretical frameworks for the description of interfacial waves, (ii) to investigate the influence of upstream flow parameters on the wavelength of boundary-layer inversion lee waves and (iii) to assess the influence of free atmospheric stratification on the shallow-water approximation.

The author contributed to a large part to the design of the study and carried out the analysis to unify the theoretical models presented in the review section. The author also selected the lee wave event and did the analysis for the Madeira lee wave case study and for the discussion of the wavelength influence of free-atmospheric stratification. Furthermore, the author prepared the figures and contributed to a large part to the interpretation of the results and the writing of the text of the manuscript.

This paper is published in Frontiers in Earth Science, Atmospheric Science:
Sachsperger, J., S. Serafin, and V. Grubišić, 2015: Lee waves on the boundary-layer inversion and their dependence on free-atmospheric stability. *Front. Earth Sci.*, **3 (70)**, doi: 10.3389/feart.2015.00070

frontiers in Earth Science

ORIGINAL RESEARCH
published: 18 November 2015
doi: 10.3389/feart.2015.00070

Lee Waves on the Boundary-Layer Inversion and Their Dependence on Free-Atmospheric Stability

Johannes Sachsperger[1]*, *Stefano Serafin*[1] and *Vanda Grubišić*[1,2]

[1] Department of Meteorology and Geophysics, University of Vienna, Vienna, Austria, [2] Earth Observing Laboratory, National Center for Atmospheric Research, Boulder, CO, USA

This study examines gravity waves that develop at the boundary-layer capping inversion in the lee of a mountain ridge. By comparing different linear wave theories, we show that lee waves that form under these conditions are most accurately described as forced interfacial waves. Perturbations in this type of flow can be studied with a linear two-dimensional model with constant wind speed and a sharp density discontinuity separating two layers, a neutral one below and a stable one above. Defining the model parameters on the basis of observations taken in the Madeira archipelago, we highlight the impact of upper-level stability on interfacial waves. We demonstrate that stable stratification aloft limits the possible range of lee wavelengths and modulates the length of the stationary wave mode. Finally, we show that the stable stratification aloft strongly constrains the validity of the shallow-water (or long-wave) approximation by permitting only short-wave modes to be trapped at the interface.

Keywords: trapped lee waves, water waves, boundary layer, inversion layer, stratified flow

OPEN ACCESS

Edited by:
Miguel A. C. Teixeira, University of Reading, UK

Reviewed by:
Stefano Federico, Institute of Atmospheric Sciences and Climate, Italy
Guðrún Nína Petersen, Icelandic Meteorological Office, Iceland
Qingfang Jiang, United States Naval Research Laboratory, USA

***Correspondence:**
Johannes Sachsperger
johannes.sachsperger@univie.ac.at

Specialty section:
This article was submitted to Atmospheric Science, a section of the journal Frontiers in Earth Science

Received: *21 August 2015*
Accepted: *29 October 2015*
Published: *18 November 2015*

Citation:
Sachsperger J, Serafin S and Grubišić V (2015) Lee Waves on the Boundary-Layer Inversion and Their Dependence on Free-Atmospheric Stability. Front. Earth Sci. 3:70. doi: 10.3389/feart.2015.00070

1. INTRODUCTION

Trapped lee waves can be generated in the atmosphere when a mountain perturbs stratified airflow. Unlike other types of mountain waves, trapped waves propagate horizontally (Smith, 1979): their phase lines are vertical and multiple wave crests can extend over several hundreds of kilometers downstream of an obstacle. If the atmosphere contains sufficient moisture, clouds may form at the wave crests (Houze, 2014) and give rise to a characteristic stripe pattern, frequently observed in satellite images close to mountainous areas, e.g., the Alps (Doyle et al., 2002), Pyrenees (Georgelin and Lott, 2001), Rocky Mountains (Ralph et al., 1997), and Pennines (Vosper et al., 2012).

Trapped lee waves can be expected to develop if the atmospheric structure promotes vertical trapping and horizontal propagation of wave energy. This occurs either when the Scorer parameter $l^2 = \frac{N^2}{U^2} - \frac{1}{U}\frac{d^2U}{dz^2}$ (where N is the buoyancy frequency and U the wind speed) decreases with height (Scorer, 1949), or along a density discontinuity, e.g., a temperature inversion. Both of these conditions lead to horizontal propagation of wave energy. In the former case, this happens through wave reflection and superposition in a wave duct; in the latter case, through adjustment to horizontal pressure gradients generated by the deflection of the discontinuity. These two mechanisms have traditionally been regarded as distinct and unrelated. The former has often been highlighted as the primary mechanism that gives rise to trapped lee waves in the atmosphere (e.g., Durran, 1986b; Wurtele et al., 1996; Teixeira, 2014), while the latter has been emphasized mostly in oceanographic investigations, for instance to explain surface water waves and the phenomenon of

dead water (Gill, 1982). In what follows, we refer to the theories that describe these two processes, respectively, as the *internal wave theory* and the *interfacial wave theory*[1].

The internal gravity wave framework, where density is assumed to be a continuous function of height, was used by Scorer (1949) to develop a theory for lee waves in a two-layer atmosphere. Scorer attributed the origin of trapped lee waves to a discontinuity in the parameter l^2, defined above. For l higher in the lower layer, horizontal wave propagation results from the linear superposition of two internal gravity wave modes, an upward-propagating one, excited by the flow over the mountain, and a downward-propagating one arising through wave reflection at the interface between the two layers.

Scorer (1949) also applied interfacial wave theory to atmospheric lee waves that form on a density discontinuity. However, that part of his work has received only little attention. After Scorer's, probably the first study explicitly addressing interfacial lee waves was made by Vosper (2004). Seeking for the most favorable environment for the formation of lee-wave rotors and low-level hydraulic jumps, Vosper (2004) analyzed the conditions that lead to wave trapping at a boundary-layer inversion underneath a continuously-stratified atmosphere. For such a density profile, interfacial waves along the inversion and vertically-propagating wave modes in the free atmosphere may occur at the same time. Teixeira et al. (2013) investigated the magnitude of wave drag, generated by both interfacial and vertically propagating waves in this scenario, and determined the state of maximum total drag. Although these two studies shed light on important aspects of interfacial lee waves, an assessment of how their wavelength (the most striking and immediate feature of the phenomenon, as visible in satellite images) depends on the environmental conditions in the free atmosphere still seems to be lacking. Therefore, the first objective of this paper is to improve the current understanding of the impact of the stratified free atmosphere on the dynamics—and the wavelength in particular—of interfacial lee waves that form at the boundary-layer inversion.

A related theme is the applicability of hydraulic analogies to the quantitative description of layered atmospheric flows. The possibility of a hydraulic-type response in two-layer mountain flow (with discontinuous l^2) was first demonstrated by Durran (1986a), who suggested that transition to supercritical flow at the top of a mountain is an effective mechanism to generate downslope windstorms. The applicability of hydraulic theory, however, depends on stratification in the free atmosphere, which affects the validity of two of the basic assumptions, namely: (i) the presence of a passive upper layer, i.e., one that causes no horizontal pressure gradient force on the lower layer (Jiang and Smith, 2001), and (ii) hydrostatic conditions, which imply the validity of the shallow-water (long-wave) approximation. Relationships between free-atmospheric stratification and the validity of the passive layer assumption have been explored by Jiang (2014). A similar study focusing on the long-wave approximation, however, still seems to be lacking. Hence, the second aim of this study is to explain how static stability in the free atmosphere affects the accuracy of the shallow-water theory when applied to low-level flow below an inversion.

We begin by reviewing the existing theories of trapped lee waves in Section 2. By taking representative values of free-atmospheric stability and inversion strength from an observed lee-wave event (Section 3), we describe how different linear analytical models lead to different estimates of lee wavelength for the same conditions (Section 4). Recognizing the important role played by free-atmospheric stratification, in Section 5 we discuss its impact on lee wavelength and on the applicability of shallow-water theory. Conclusions are drawn in Section 6.

2. REVIEW OF LEE WAVE THEORIES

As briefly discussed in the Introduction, the simplest models of trapped lee waves consider uniform wind speed and a vertical discontinuity, either in the Scorer parameter l or in potential temperature θ. Such discontinuities are responsible for different wave-trapping mechanisms, which may co-exist for a vertical potential temperature profile like the one shown in **Figure 1**. The defining parameters of this type of flow are the buoyancy frequencies in the lower and upper layer (N_1 and N_2 respectively), the potential temperature jump across the interface ($\Delta\theta$), the potential temperature at the ground (θ_0) and the height of the lower layer (h_1).

In general, the dynamics of wave propagation can be concisely described by a frequency dispersion relationship (FDR), i.e., a relation between the intrinsic frequency of the wave, Ω, and the wavenumber, k. For simplicity, we focus on flows with uniform background wind speed U. The Scorer parameter simplifies to $l^2 = \frac{N^2}{U^2}$ in this case. Since lee waves are typically stationary, we consider only wave modes that do not move in a reference frame attached to the mountain, thus $\Omega/k - U = 0$. All wave modes k that satisfy this relation are stationary with respect to the mountain.

For the stability profile in **Figure 1**, the FDR of trapped lee waves can be derived by assuming that wavelike solutions to the governing equations exist in each of the two layers. The derivation, presented in the Appendix, leads to:

$$U^2 = \frac{g'}{im_1 \coth\left(im_1 h_1\right) - im_2} \quad . \tag{1}$$

Here, h_1 is the finite thickness of the lower layer (the upper one being instead infinitely deep), $g' = g \cdot \Delta\theta/\theta_0$ is the reduced gravity at the interface and $m_{1,2} = (l_{1,2}^2 - k^2)^{1/2}$ are the vertical wave-numbers in the lower (subscript 1) and in the upper layer (subscript 2) respectively.

Equation (1) summarizes the behavior of four wave types that may occur in common atmospheric conditions:

– *Internal interface waves*, developing at a density discontinuity between two neutrally stratified fluid layers ($\Delta\theta \neq 0$, $N_{1,2} = 0$).

[1] *Interfacial wave theory* is in turn related to *hydraulic theory*. Hydraulic theory is based on the analogy between the flow of a compressible gas and the flow of a shallow liquid, and is inherently hydrostatic. In contrast, no *a priori* assumption about hydrostaticity is made in interfacial wave theory.

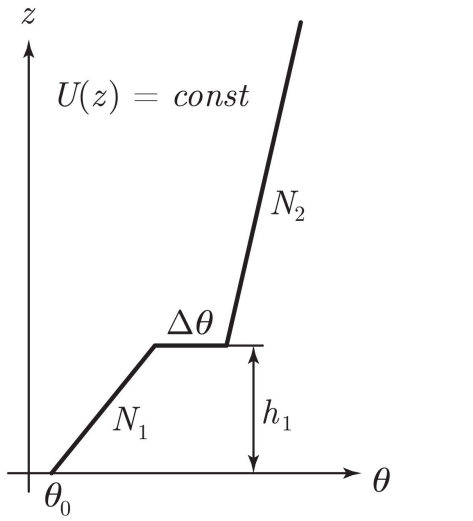

FIGURE 1 | Vertical potential temperature (θ) profile of a generic two-layer flow with a density interface. The wind profile $U(z)$ is assumed to be constant with height (not shown).

- *Free interface waves*, propagating along a density discontinuity between a lower neutral layer and an upper stably stratified passive layer ($\Delta\theta \neq 0, N_1 = 0, m_2 = 0$).
- *Forced interface waves*, similar to the previous case, but with an upper stably stratified active layer ($\Delta\theta \neq 0, N_1 = 0, m_2 \neq 0$).
- *Resonant trapped waves*, developing at a discontinuity in the Scorer parameter ($\Delta\theta = 0, N_1 > N_2 > 0$).

These wave types, and the conditions under which they may form, are described in greater detail in what follows.

2.1. Internal Interface Waves

If both fluid layers are neutrally stratified, wave energy is concentrated at the density discontinuity between them, because all wave modes are evanescent below and above it ($m_{1,2}^2 < 0$). If the source of the wave energy is at the surface, as is the case with mountain waves, higher altitudes of the interface will result in lower lee wave amplitudes. This happens because evanescent wave modes decay with increasing distance from the wave source. Assuming $N_{1,2} = 0$ in Equation (1), the FDR of stationary interfacial waves becomes (Turner, 1973):

$$U^2 = \frac{g'}{k \coth(kh_1) + k} \quad . \tag{2}$$

The coth (kh_1) term in Equation (2) is non-periodic in k, because the argument is a real number. Thus, only a single stationary wave mode can exist on the density discontinuity. The FDR in Equation (2) describes interfacial waves at internal boundaries with a non-passive upper layer, which is the case for relatively short wave modes ($\partial p_2'/\partial x \neq 0$ if $k > 0$, p_2' being the pressure perturbation in the upper layer; see e.g., Nappo, 2012).

Equation (2) is well-known in its long-wave approximation form, where the condition $kh_1 \ll 1$ leads to the non-dispersive FDR:

$$U = (g'h_1)^{1/2} \quad . \tag{3}$$

Another limiting case of Equation (2), that gained less attention in meteorological literature, can be derived by adopting the short-wave approximation, $kh_1 \gg 1$:

$$U = (g'/2k)^{1/2} \quad . \tag{4}$$

Unlike Equation (3), Equation (4) retains the dispersive character of Equation (2) and can be solved for k to estimate the wavelength of a stationary internal interface wave. The FDRs in Equations (3) and (4) are similar to those of shallow- and deep-water external waves, which correspond to the limit $g' \to g$. However, since Equations (3) and (4) apply to flows where the upper layer has non-negligible density, they still describe *internal* interface wave modes.

2.2. Free Interface Waves

Interfaces that are not subject to stress exerted by the upper fluid are referred to as *free surfaces*. The passive layer assumption, $\partial p_2'/\partial x = 0$, applies in this case. Special cases of free surfaces are those where the density difference between the two fluid layers is very large, e.g., between water and air. The corresponding theory was developed by Airy (1841), who firstly derived the universal FDR of (external) water waves (Craik, 2004):

$$U^2 = \frac{g}{k \coth(kh_1)} \quad . \tag{5}$$

This equation is not generally valid in atmospheric flows, which are typically characterized by very small density discontinuities. However, even in the atmosphere it is possible for a density discontinuity (e.g., the capping inversion of the convective boundary layer) to act as a free surface. This is the case if $N_1 = 0$ and $m_2 = 0$. The second constraint means that any internal gravity wave mode in the stably-stratified upper layer must have vertical phase lines at the interface. In this case, Equation (1) becomes:

$$U^2 = \frac{g'}{k \coth(kh_1)} \quad . \tag{6}$$

Although this wave type occurs in the interior of a fluid, the interface behaves as a free surface. The upper layer is passive because of the condition $m_2 = 0$, which implies that wave perturbations in the pressure field, and consequently the horizontal pressure gradient, must vanish therein, as can be demonstrated from the polarization relationships of internal gravity waves (see, e.g., Nappo, 2012). The same applies to wave perturbations in the horizontal wind speed. The FDR of these (internal) *free interface waves* is similar to that of (external) water waves in Equation (5), except for reduced gravity g' instead of g.

2.3. Forced Interface Waves

Interfacial waves conform to Equation (6) only when their horizontal wavenumber is equal to the Scorer parameter in the atmosphere aloft (in fact, $m_2 = 0$ implies $k = l_2$). In general, however, $k \neq l_2$. In this case the upper layer is not passive, i.e., waves propagating along the interface are subject to forcing from internal waves above. The FDR describing these (internal) *forced interface waves* is obtained from Equation (1) by requiring $N_1 = 0$ and maintaining a wave-permitting layer with $N_2 > 0$ aloft (Scorer, 1997):

$$U^2 = \frac{g'}{k \coth\left(kh_1\right) + \sqrt{k^2 - l_2^2}} \quad . \tag{7}$$

Equation (7) is the general form of the FDR considered by Vosper (2004), which is the corresponding short-wavelength ($kh_1 \gg 1$) approximation. All wave modes satisfying $k^2 < l_2^2$ ($m_2^2 > 0$) can propagate into the upper stratified layer, hence they are not trapped at the interface. Consequently, the condition $k^2 = l_2^2$ defines a critical wavenumber, i.e., the lowest wavenumber (longest wavelength) for which wave trapping is possible. This condition transforms Equation (7) into Equation (6), i.e., into the special case of a free interfacial wave (Section 2.2), and generates the maximum total wave drag (Teixeira et al., 2013).

Equation (7) shows that, given N_2 and U, the critical wavenumber depends on the inversion strength $\Delta\theta$ (through g') and on the lower layer depth h_1. Critical values for $\Delta\theta$ and h_1 can be determined inserting $k = l_2 = N_2/U$ into Equation (7). Solving for $\Delta\theta$ or h_1 then gives:

$$\Delta\theta_{crit} = \frac{N_2\ U\ \theta_0}{g} \cdot \coth\left(\frac{N_2 h_1}{U}\right) \tag{8}$$

$$h_{1crit} = \frac{U}{N_2} \cdot \operatorname{acoth}\left(\frac{g'}{N_2 U}\right) \tag{9}$$

Inversions with strength $\Delta\theta \geq \Delta\theta_{crit}$, or located at height $h_1 \geq h_{1crit}$, cause wave trapping because they make stationary waves become evanescent in the layer aloft.

2.4. Resonant Trapped Waves ($g' = 0$)

Setting $g' = 0$ (that is, $\Delta\theta = 0$) in Equation (1) simplifies it to (Scorer, 1949):

$$\coth\left(im_1 h_1\right) = \sqrt{\frac{l_2^2 - k^2}{l_1^2 - k^2}}. \tag{10}$$

Therefore, wave trapping occurs even in absence of a density discontinuity if a wave mode k that satisfies Equation (10) exists. Scorer (1949) showed that this is the case if

$$l_1^2 > k^2 > l_2^2 \tag{11}$$

$$l_1^2 - l_2^2 > \frac{\pi^2}{4h_1^2} \quad . \tag{12}$$

In these conditions, an internal gravity wave mode that propagates vertically in the lower layer is reflected at the discontinuity of l^2, above which it becomes evanescent. The superposition of the reflected and primary mode generates a stationary wave with vertical phase lines, trapped in the layer below the interface. We refer to this wave type as a *resonant trapped* wave. In contrast to the FDRs for interfacial waves [Equations (2), (6), and (7)], the argument of the cotangent function in Equation (10) is imaginary. Since the roots of $\coth\left(im_1 h_1\right)$ are periodic, multiple resonant modes may exist. The amplitude of these modes depends essentially on the interface height and on the mountain shape. In general, the mode with the wavelength closest to the mountain half-width L is dominant.

2.5. Bridging the Theories of Interfacial and Resonant Trapped Lee Waves

Wave propagation in stratified fluids with a more complex vertical structure, i.e., with more than two layers, has been studied with analytical models in the past. For instance, Baines (1995, p. 189) formulated a non-hydrostatic three-layer model, that can be used to estimate the horizontal wavenumber of a lee wave trapped along a finite-thickness inversion. In this case, the wavenumber k satisfies the following FDR:

$$\left[\tan(m_1 h_1) - \frac{im_1}{m_2}\right](m_2 - m_3) = e^{-2im_2 d}\left[\tan(m_1 h_1) + \frac{im_1}{m_2}\right](m_2 + m_3)\,. \tag{13}$$

Here, subscripts $j = 1, 2, 3$ denote the fluid layers, numbered from below; $m_j = \left(N_j^2/U^2 - k^2\right)^{1/2}$ is the vertical wavenumber in each of the layers; h_1 is the thickness of the lowest layer and d that of the middle one (the inversion layer). The third layer represents the free atmosphere, which is assumed to be infinitely deep. Equation (13) is transcendental, because it has no closed-form solutions for k. Moreover, it remains transcendental even after adopting the long- ($kh_1 \ll 1$) or short-wave ($kh_1 \gg 1$) approximations, in contrast to the two-layer models introduced in Sections 2.1–2.3 above.

In the strict limit of the middle layer depth being zero ($d = 0$), the inversion disappears and the FDR in Equation (13) approaches the FDR for resonant waves (Equation 10). This is to be expected as the Baines (1995) model assumes a continuous density profile.

For small but finite values of the inversion depth and the finite value of $\Delta\theta$ across the inversion, one would expect the solution of Equation (13) to converge to that of the most general two-layer model (Equation 1), assuming that all other parameters are the same. We show this to be true in the following section by numerically solving Equation (13) for a specific case (cf. **Figure 3**).

3. WAVES ALONG THE BOUNDARY-LAYER INVERSION

The typical thermal structure of the convective boundary layer ($N_1 \approx 0, N_2 > 0, \Delta\theta > 0$) is such that it supports forced interface waves (Section 2.3). Since similar conditions are often

present above ocean surfaces, or at daytime during the warm season over land, it is likely that wave trapping at the boundary layer inversion is a common mechanism for lee waves.

To confirm this hypothesis, we study a lee wave event that occurred on 24 December 2013 downstream of the Desertas islands. These islands are part of the Madeira archipelago, located in the subtropical Atlantic ∼800 km south-west of mainland Portugal. The Desertas are elongated in the N-S direction and reach an altitude of 300 m MSL. Sufficient data is available in this area to estimate the wavelength (from high-resolution satellite images) and the vertical structure of the atmosphere (from operational radiosonde observations in Funchal, Madeira's capital).

The satellite image in **Figure 2A** shows a characteristic cloud-stripe pattern, generated by a trapped wave leeward of the Desertas islands. The lee wave train is not visibly influenced by the prominent wake of Madeira (Grubišić et al., 2015) and extends over a distance of 40 km with approximately nine wave crests, hence $\lambda \approx 4.4$ km.

The vertical structure of the atmosphere during this event, as measured in nearby Funchal, is shown in **Figure 2B**. It consists of a neutrally stratified lower layer ($N_1 = 0$) with $\theta_0 = 291$ K, a boundary-layer inversion with $\Delta\theta = 8$ K at $h_1 = 1100$ m and a continuously stratified free atmosphere with $N_2 = 0.010$ s^{-1} aloft. The flow is westerly with almost no directional shear. A representative value of $U = 10$ m s^{-1} for the wind speed is determined from the wind profile in **Figure 2C** as the average in the layer below $z = 2h_1$. The altitude of the inversion coincides with the layer of largest relative humidity (gray shading, $RH = 97\%$ at $h_1 = 1100$ m), implying that the cloud pattern in **Figure 2A** likely corresponds to an interfacial wave. Further evidence for the interfacial wave character of the disturbance is provided by the Scorer parameter profiles in **Figure 2D**. The observed wave mode (dashed black) is evanescent ($k^2 > l^2$) below and above the inversion, indicating that the disturbance can only propagate along it. The flow configuration determined from **Figure 2B** is similar to that causing forced interfacial waves (Section 2.3).

Given its small thickness, the inversion layer can be approximated as a density discontinuity. This is supported by a comparison between the solutions of Equation (1), which is derived from the discontinuous two-layer model, and Equation (13), which is derived from the continuous three-layer model introduced in Section 2.5. Both equations are solved numerically for $\lambda = 2\pi/k$, imposing the sounding parameters presented above and letting d in the three-layer model vary in the range between 0 and 1000 m. The results in **Figure 3** reveal a difference of ∼5% in the wavelength estimates for $d = 150$ m, which corresponds to the observed profile. This level of accuracy is sufficient for our needs. Hence, from now on, we only consider two-layer models, with the benefit that an analytical solution for k is possible (if the short-wave approximation is adopted).

In what follows, we use observations from the Desertas islands to provide numerical values for the parameters of the linear models described in Section 2, and thereby explore the impact of free-atmospheric stratification on interfacial waves.

4. LINEAR THEORY RESULTS

Our two-dimensional, two-layer linear model is described in detail in the Appendix. We solve it for the perturbation velocity fields $u'(x, z)$ and $w'(x, z)$ as a function of the flow profile

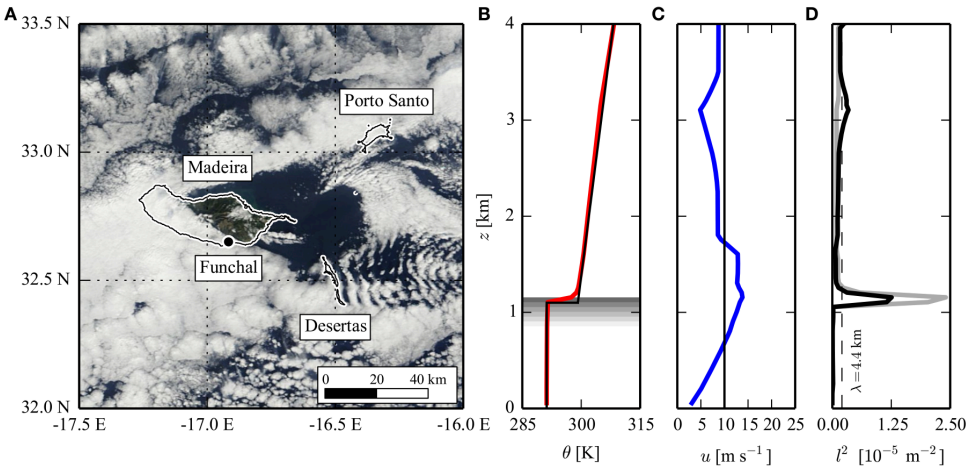

FIGURE 2 | (A) MODIS Terra visible satellite image on 24 December 2013, showing signature of trapped lee waves downwind of the Desertas islands in the Madeira archipelago. Coastlines are shown with solid white-black contours. The location of the sounding site (Funchal) is marked with a black dot. Flow is from left to right. Satellite image from NASA Earthdata and SRTM topography data from Jarvis et al. (2008). **(B–D)** Funchal operational sounding at 1200 UTC 24 December 2013. The panels show vertical profiles of **(B)** potential temperature, **(C)** wind speed projected in lee wave direction and **(D)** Scorer parameter $l^2 \approx [N/U(z)]^2$ (black), $l^2 \approx [N/U]^2$ with $U = 10$ m s^{-1} (gray) and observed wavenumber k^2 (dashed). The solid black lines in **(B,C)** show the approximated idealized sounding that defines the parameters listed in **Table 1**. Gray shaded areas in **(B)** indicate regions where relative humidity $RH > 90\%$.

TABLE 1 | Flow parameters determined from the sounding in Figure 2.

	FIW	IIW	Free IIW	
N_1	0	0	0	s^{-1}
N_2	0.010	0	0.010	s^{-1}
$\Delta\theta$	8	8	$\Delta\theta_{crit} = 3.7$	K
h_1	1100	1100	1100	m
U	10	10	10	$m\,s^{-1}$

FIW (forced interface wave) represents the observed flow configuration, IIW (internal interface wave) assumes $N_2 = 0$ and Free IIW (free internal interface wave) assumes $\Delta\theta = \Delta\theta_{crit}$.

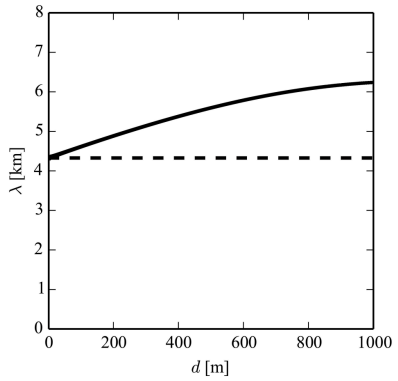

FIGURE 3 | Comparison of the wavelength λ estimated from the FDR of forced interfacial waves (Equation 7, dashed) and from the Baines (1995) three-layer model (Equation 13, solid).

$(N_1, N_2, U, \Delta\theta, h_1)$ and the topography $h_0(x)$. The latter is specified with a cosine function, in analogy to Vosper (2004):

$$h_0(x) = \begin{cases} H/2 + H/2 \cdot \cos\left[\frac{\pi}{L}(x - x_0)\right] & \text{if } x_0 - L < x < x_0 + L \\ 0 & \text{elsewhere} \end{cases}$$

Here, $H = 300$ m denotes the mountain height and $L = 2$ km its half-width, while x_0 is the location of the mountain top. The model parameters $(N_1, N_2, U, \Delta\theta, h_1)$ are estimated from the idealized sounding in **Figures 2B,C** and are listed in **Table 1**.

Figure 4 shows the wave field predicted by linear theory in two-layer flow over the mountain for two combinations of parameters, one reflecting the observations ($N_2 = 0.010\ s^{-1}$, **Figures 4A,D**) and the other disregarding stratification in the free atmosphere ($N_2 = 0$, **Figures 4B,E**). For completeness, in **Figures 4C,F** we also show the wave field for the special case $\Delta\theta = \Delta\theta_{crit}$, i.e., when the interface acts as a free surface (Section 2.2).

Two wave branches are evident in the wave perturbations u' and w' in **Figures 4A,D**: a vertically propagating internal gravity wave and an interfacial wave. The mountain wave branch consists of those wave modes that can propagate into the continuously stratified upper layer ($k^2 < l_2^2$). The interfacial disturbance, in contrast, consists of a single stationary wave mode, described by Equation (7). The wavelength of this stationary mode ($\lambda = 4.2$ km) is close to the observations ($\lambda = 4.4$ km) in the satellite image in **Figure 2A**. Both u' and w' reach their maximum amplitude at the interface height. While w' is continuous across the interface, u' is discontinuous and changes sign as a consequence of the incompressibility constraint.

The wave structure in flow with a neutral upper layer in **Figures 4B,E** is different. As expected, the wave branch in the upper layer vanishes due to the absence of stratification in the free atmosphere. The wavelength of the disturbance ($\lambda = 5.0$ km), determined from Equation (2), increases slightly (by 19%) compared to that in **Figure 4A**. This suggests that free-atmospheric stratification does not impact the lee wavelength significantly for the case examined in this paper. This aspect is discussed in more detail in Section 5.

In the special case where $\Delta\theta = \Delta\theta_{crit}$, the wave field consists of a free interfacial disturbance with a wavelength of $\lambda = 2\pi/l_2$ (**Figures 4C,F**). In this case, the perturbations u' necessarily vanish right above the inversion, as discussed in Section 2.2. In fact, u' is confined entirely in the layer below the inversion in **Figure 4F**, similarly to what happens in water waves. The vertical wind speed w', in contrast to u', is continuous across the interface. In this case, $\lambda = 6.3$ km.

Given the relatively good agreement between observations and linear model results in the Desertas lee-wave case, we use linear theory to explore the dependence of the lee wavelength ($\lambda = 2\pi/k$) on the flow parameters $(\Delta\theta, h_1, N_2, U)$. We impose $N_1 = 0$, because convective boundary layers are typically neutrally stratified.

We proceed by solving the FDRs of internal interface waves (IIW, Equation 2) and of forced interface waves (FIW, Equation 7), varying systematically one of the four parameters mentioned above while keeping all others unchanged. We consider the IIW ($N_2 = 0$) and FIW ($N_2 \neq 0$) flow models because the difference between their solutions allows us to appreciate the impact of free-atmospheric stratification on the lee wavelength. The lee wavelengths, λ_{IIW} and λ_{FIW}, are obtained numerically, because the FDRs are transcendental and cannot be solved analytically.

The results of this elaboration are shown in the four panels of **Figure 5**, which consider $\Delta\theta \in [0, 15]$ K, $h_1 \in [0, 5000]$ m, $N_2 \in [0, 0.03]\ s^{-1}$, and $U \in [0, 15]\ m\ s^{-1}$; λ_{IIW} and λ_{FIW} are shown in all panels as dashed and solid lines respectively. White dots in **Figures 5A,B** mark the critical values $\Delta\theta_{crit}$ (Equation 8) and h_{1crit} (Equation 9). The behavior of λ_{IIW} and λ_{FIW} is generally similar: they increase with increasing wind speed U, while they decrease with increasing $\Delta\theta$ and h_1. While λ_{FIW} decreases with N_2, λ_{IIW} is inherently independent of it, because $N_2 = 0$ in the IIW model.

Since N_2 is the only parameter that differs between the IIW ($N_2 = 0$) and the FIW model ($N_2 \neq 0$), large differences between λ_{IIW} and λ_{FIW} indicate that interfacial waves are heavily affected by the free-atmospheric stratification. This is the case for: weak inversions (**Figure 5A**, maximum deviation 38%), high wind speeds (**Figure 5D**, maximum deviation 27%) and for strong stratification (**Figure 5C**, maximum deviation 117%). Conversely, λ_{IIW} and λ_{FIW} both become independent of the layer

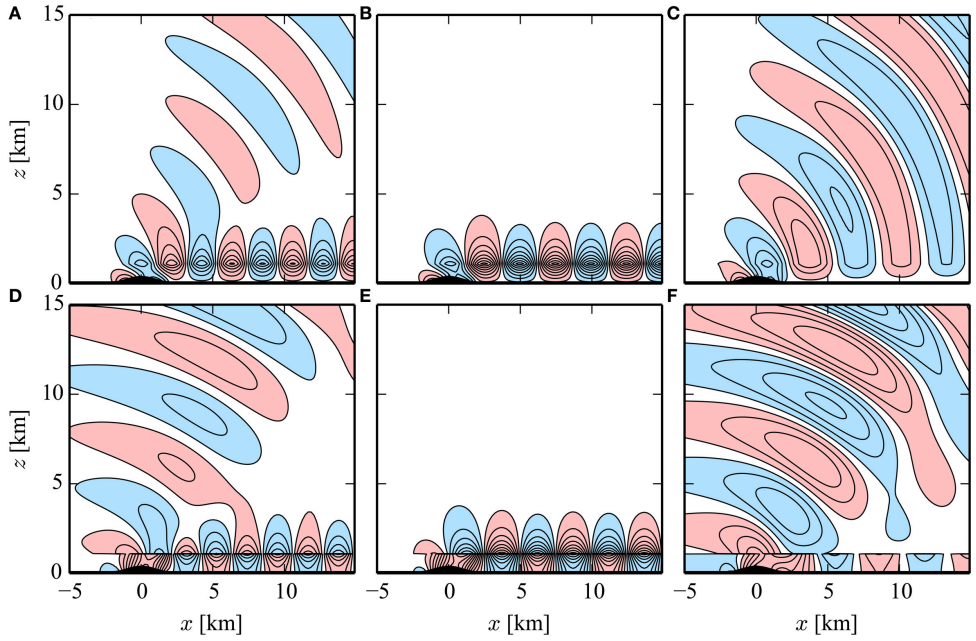

FIGURE 4 | Wave perturbations $w'_{1,2}$ (top) and $u'_{1,2}$ (bottom) determined from linear model solutions (Equations A2 and A3). Model parameters are listed in **Table 1** and correspond respectively to: **(A–D)** forced interface waves; **(B–E)** internal interface waves; **(C–F)** free interface waves. Red and blue shading denote respectively positive and negative areas. The contour interval is 0.5 m s^{-1}.

height h_1 for values beyond $h_1 > 1100$ m (**Figure 5B**). This indicates that the short-wave (or deep-water) approximation is valid for the Desertas lee-wave case examined (the FDR is then independent of h_1, see Equation 4).

5. DISCUSSION

The results described in Section 4 suggest that stratification in the free atmosphere can indeed have a significant influence on the length of interfacial trapped lee waves. In Section 5.1 below, we determine this impact more precisely after simplifying the FDRs of the FIW and IIW models with the short-wave approximation.

Besides controlling lee wavelength, a continuously-stratified free atmosphere limits the range of possible trapped modes on the interface, because it allows the longest ones to propagate vertically through it (as shown in Section 2). This circumstance can impact the validity of the shallow-water approximation, which is inherently applicable only for long wave modes. We discuss this aspect in Section 5.2.

5.1. Impact of Free-atmospheric Stratification on Lee Wavelength

The results shown in **Figure 5** suggest that differences between IIW and FIW predictions depend mostly on g', N_2, and U.

The relative difference between λ_{IIW} and λ_{FIW} cannot be derived analytically from the corresponding FDRs, Equations (2) and (7), because these equations are transcendental with respect to k. Therefore, we simplify them adopting the short-wave approximation $\coth(kh_1) \approx 1$ (when $kh_1 \gg 1$) to obtain analytical expressions for the wave number k. Equations (2) and (7) simplify to:

$$k_{IIW} = \frac{g'}{2U^2} \tag{14}$$

$$k_{FIW} = \frac{g'}{2U^2} + \frac{N_2^2}{2g'}\,. \tag{15}$$

Clearly, the second term on the right-hand side in Equation (15) represents the influence of free-atmospheric stratification on interfacial waves. The relative magnitude of the second term in Equation (15) can be expressed as:

$$\sigma = \frac{k_{FIW} - k_{IIW}}{k_{IIW}} = \frac{N_2^2}{2g'} \Big/ \frac{g'}{2U^2} = \left(l_2 \Big/ \frac{g'}{U^2}\right)^2 = \left(\frac{N_2 U}{g'}\right)^2 \quad . \tag{16}$$

The parameter σ is the ratio between the Scorer parameter in the free atmosphere, l_2, and the coefficient g'/U^2, which quantifies the strength of the BL inversion and appears in the dynamic boundary condition imposed at that interface (see Appendix). According to Jiang (2014), $\sqrt{\sigma}$ represents the ratio

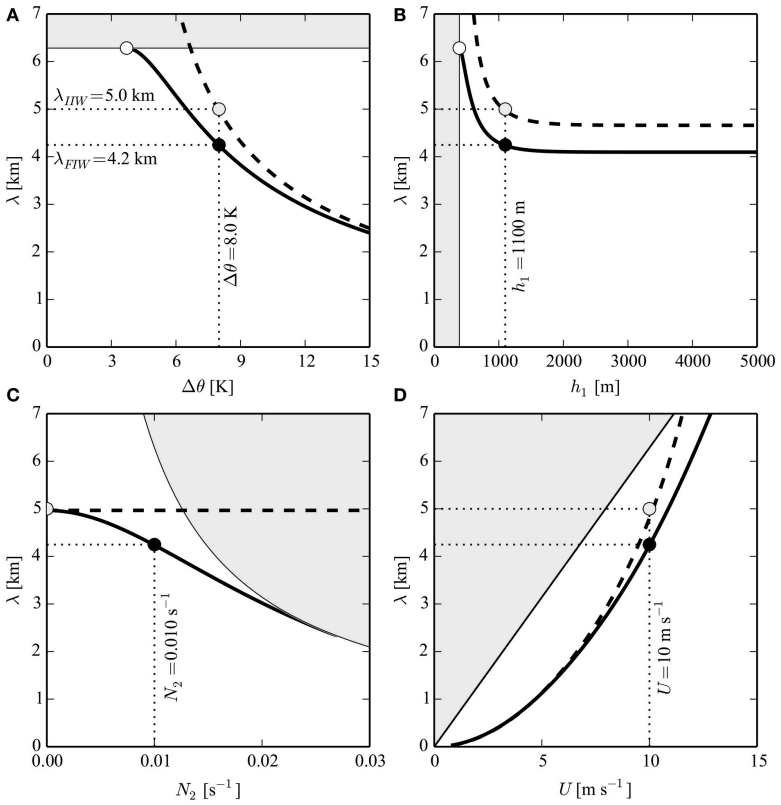

FIGURE 5 | Dependence of the lee wavelength λ on: (A) inversion strength, $\Delta\theta$; (B) inversion height, h_1; (C) free-atmospheric stratification, N_2; and (D) wind speed, U. Solid and dashed lines correspond respectively to λ_{FIW} and λ_{IIW}. Black dots represent the wavelength estimated from the observed flow profile (see **Figure 2**); gray dots indicate the corresponding wavelength when $N_2 = 0$; and white dots mark the critical values $\Delta\theta_{crit}$ and h_{1crit} at the corresponding wavelength $\lambda = 2\pi U/N_2$. Shaded areas indicate the propagating regime in the upper layer, i.e., where wave trapping on the interface is not possible.

between the perturbation pressure associated with waves above the inversion (proportional to $N_2 U$) and the density jump across the inversion (proportional to g'). If σ is small, inversion effects dominate over those introduced by the wave-permitting layer above, and interfacial waves are unaffected by stratification aloft. The passive layer assumption can then be applied if the flow is hydrostatic (Jiang, 2014). However, it generally does not hold for non-hydrostatic flow, even when $\sigma = 0$. This is because interfacial trapped waves excite evanescent short-wavelength pressure perturbations p_2' into the upper layer, consequently $\partial p_2'/\partial x \neq 0$ (Section 2.1). The dependence of σ on l_2 and g'/U^2 is shown in **Figure 6**: σ increases with increasing l_2, but decreases with increasing g'. This behavior is consistent with the curves representing the full FDRs in **Figure 5**.

The considerations expressed above are rigorously valid only if $kh_1 \gg 1$. If this condition applies, then σ (and hence the difference between λ_{IIW} and λ_{FIW}) is independent of the layer depth h_1. However, this is not the case if the layer depth is relatively shallow (**Figure 5B**).

For the case in exam here, the layer depth can be shown to have only a marginal impact on the lee wavelength. With the deep-water approximation (that is, neglecting the influence of the lower layer depth), Equation (16) leads to $\sigma = 0.14$. Without the deep-water approximation (that is, preserving the influence of the lower layer depth), σ can be estimated on the basis of the relative difference between λ_{IIW} and λ_{FIW} from any panel in **Figure 5**: $\sigma = (\lambda_{IIW} - \lambda_{FIW})/\lambda_{FIW} \approx 0.8/4.2 = 0.19$. This means that the wavenumber of the interfacial wave increases due to stratification in the free atmosphere by 19% (white dot in **Figure 6**). The close agreement with the estimate from Equation (16) ($\sigma = 14\%$) indicates that the deep-water approximation is valid in this case.

Given the good agreement between wavelength estimates that are subject to and independent of the short-wavelength approximation, we expect that using σ to assess the importance of stratification effects on interfacial waves beneath the stable layer will give accurate results for most interfacial lee wave observations.

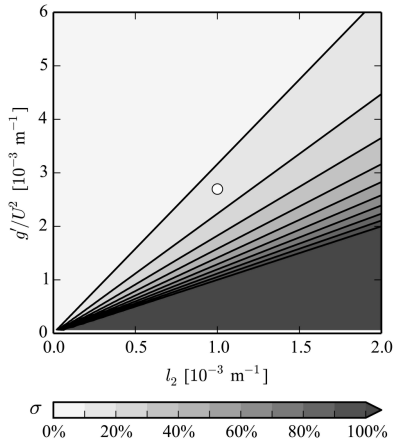

FIGURE 6 | Estimation of the stratification impact on interfacial deep-water waves. Gray shading represents the values of $\sigma = \left[l_2/(g'/U^2)\right]^2$. The white dot shows the flow configuration of the observed lee wave case.

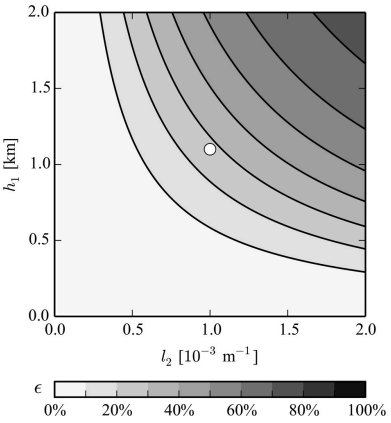

FIGURE 7 | Estimation of the error due to stratification effects in the shallow-water approximation. Gray shading and contours represent the values of $\epsilon = 1 - (l_2 h_1) \cdot \coth(l_2 h_1)$. The white dot shows the flow configuration of the observed lee wave case.

5.2. Impact of Free-atmospheric Stratification on the Shallow-water Approximation

Mountains excite a continuous spectrum of vertically-propagating wave modes if the atmosphere is continuously stratified. In two-layer flow, as shown above, part of these modes become trapped at the interface between the fluid layers. In particular, only relatively short modes satisfying $k > l_2$ are trapped. In what follows, we use this trapping criterion to investigate the validity of the long-wave approximation, which is a fundamental assumption in shallow-water theory, in the presence of a stably stratified upper layer.

Multiplying the terms in the inequality above by h_1 yields $kh_1 > l_2 h_1$. On the other hand, the long-wave (or shallow-water) approximation, $\coth(kh_1) \approx (kh_1)^{-1}$, is only valid when $kh_1 \ll 1$. Scale analysis suggests that the two conditions $kh_1 > l_2 h_1$ (under which interfacial waves exist) and $kh_1 \ll 1$ (under which they can be treated with the shallow-water approximation) can be incompatible.

Typical values for the order of magnitude of the Scorer parameter and the layer depth are respectively $\mathcal{O}(l_2) = 10^{-3}$ and $\mathcal{O}(h_1) = 10^3$, hence $\mathcal{O}(l_2 h_1) = 1$. In this case, the shallow-water approximation is clearly inappropriate. The range of values of l_2 and h_1 for which the approximation remains valid can be estimated from the ratio between the transcendental term in Equation (7), $\coth(kh_1)$, and its shallow-water approximation form, $(kh_1)^{-1}$. This ratio is equal to unity if the approximation is accurate. The inaccuracy is hence quantified by the deviation of the ratio from unity, considering the longest possible trapped mode ($k = l_2$):

$$\epsilon = 1 - (l_2 h_1) \cdot \coth(l_2 h_1) \quad . \tag{17}$$

The dependence of ϵ on l_2 and h_1 is shown in **Figure 7**. Clearly, stratification aloft (l_2) can cause large deviations from ideal shallow-water behavior, easily exceeding $\epsilon = 50\%$ for fairly typical atmospheric conditions. For the Desertas case, $\epsilon \approx 30\%$. We conclude that the non-hydrostatic linear frameworks presented in Section 2 are far more accurate than the shallow-water framework in describing the propagation properties of interfacial waves. This is especially the case, when the overlying free atmosphere is stably stratified.

6. SUMMARY AND CONCLUSIONS

Lee-wave cloud patterns, frequently observed downstream of islands, are often attributed to the presence of resonant gravity waves. Rigorously, resonant waves are expected to develop if the potential temperature profile is continuous and includes a stable layer below a neutral (or less stable) one. In the case of the marine boundary layer, one instead finds a nearly neutral layer capped by a sharp inversion, which can be thought of as a discontinuity in the potential temperature profile. Lee waves may be more appropriately interpreted as interfacial waves in this case.

Using the results of a linear two-layer flow model to explain the lee wavelength in observations taken in the Madeira archipelago, we highlight the large impact that free-atmospheric stability has on interfacial waves at the boundary-layer capping inversion. Through use of linear theory, we demonstrate that interfacial waves are affected by stable stratification aloft (i.e., by an overlying wave-permitting layer) in two ways:

- First, stratification in the upper layer limits the possible range of lee wavelengths. This happens because wave modes with $k^2 < l_2^2$ propagate vertically in the upper layer, without being trapped at the interface (Vosper, 2004). From this criterion, we derived the critical (minimum) values of inversion strength ($\Delta\theta_{crit}$, Equation 8) and height (h_{1crit}, Equation 9) for wave trapping. We showed that waves on an inversion where $\Delta\theta = \Delta\theta_{crit}$, or equivalently $h_1 = h_{1crit}$, are dynamically identical to

surface water waves (see Section 2.2), i.e., they are described by identical FDRs. This equivalence is only possible if the atmosphere above the inversion is stably stratified.

- Second, the wavelength of interfacial disturbances decreases with increasing stratification in the upper layer. In the short-wave limit ($kh_1 \gg 1$), the parameter $\sigma = \left[l_2/(g'/U^2)\right]^2$ quantifies the relative difference between the length of interfacial waves in flow with a neutral and a stratified upper layer. If σ is small, stratification in the free atmosphere has a negligible impact on interfacial waves riding along the inversion.

Furthermore, we show that the shallow-water (or long-wave) approximation ($kh_1 \ll 1$) may give an inaccurate description of interfacial waves in atmospheric flows when the upper layer is stably stratified. This is because inversions only trap short wave modes ($k^2 > l_2^2$). In fact, the two criteria $k^2 > l_2^2$ and $kh_1 \ll 1$ are generally incompatible for typical values of h_1 and l_2 in the atmosphere. Conversely, interfacial waves in such conditions are more properly described with the non-hydrostatic linear frameworks presented in Section 2. The deep-water approximation is more appropriate in this case.

A major limitation of this study is that it is restricted to flows with constant background wind speed U. Vertical variability in the horizontal wind profile is known to affect wave propagation by creating wave ducts in regions with high curvature, $(1/U)(d^2U/dz^2)$, which typically coincide with jets. Furthermore, sharp wind speed gradients, typically occurring across temperature inversions, favor the onset of shear instability (e.g., Kelvin-Helmholtz billows). We note here that the FDR of Kelvin-Helmholtz waves in a two-layer discontinuous density profile (see, e.g., Nappo, 2012) converges to that of internal interface waves (Equation 2), for vanishing wind speed difference across the interface. An accurate investigation of the impact of wind speed variability on interfacial waves is, however, outside the scope of this work, and is left for future investigation.

ACKNOWLEDGMENTS

We thank the reviewers of this paper for their comments and suggestions. This study was supported by the FWF (Austrian Science Fund) grant P24726-N27 to the University of Vienna. NCAR is sponsored by the National Science Foundation.

REFERENCES

Airy, G. B. (1841). "Tides and waves," in *Encyclopaedia Metropolitana (1817–1845), Mixed Sciences*, Vol. 3, eds H. J. Rose, H. J. Rose, and E. Smedley (London: B Fellowes), 241–396.

Baines, P. G. (1995). *Topographic Effects in Stratified Fluids*. Cambridge: Cambridge University Press.

Craik, A. D. (2004). The origins of water wave theory. *Annu. Rev. Fluid Mech.* 36, 1–28. doi: 10.1146/annurev.fluid.36.050802.122118

Doyle, J. D., Volkert, H., Dörnbrack, A., Hoinka, K. P., and Hogan, T. F. (2002). Aircraft measurements and numerical simulations of mountain waves over the central Alps: a pre-MAP test case. *Q. J. R. Meteorol. Soc.* 128, 2175–2184. doi: 10.1256/003590002320603601

Durran, D. R. (1986a). Another look at downslope windstorms. Part I: the development of analogs to supercritical flow in an infinitely deep, continuously stratified fluid. *J. Atmos. Sci.* 43, 2527–2543. doi: 10.1175/1520-0469(1986)043<2527:ALADWP>2.0.CO;2

Durran, D. R. (1986b). "Mountain waves," in *Mesoscale Meteorology and Forecasting*, ed P. S. Ray (Boston, MA: American Meteorological Society), 472–492.

Georgelin, M., and Lott, F. (2001). On the transfer of momentum by trapped lee waves: case of the IOP 3 of PYREX. *J. Atmos. Sci.* 58, 3563–3580. doi: 10.1175/1520-0469(2001)058<3563:OTTOMB>2.0.CO;2

Gill, A. E. (1982). *Atmosphere-Ocean Dynamics*. London: Academic Press.

Grubišić, V., Sachsperger, J., and Caldeira, R. M. (2015). Atmospheric wake of Madeira: first aerial observations and numerical simulations. *J. Atmos. Sci.* doi: 10.1175/JAS-D-14-0251.1. [Epub ahead of print].

Houze, R. A. (2014). *Cloud Dynamics*. Oxford: Academic Press.

Jarvis, A., Reuter, H. I., Nelson, A., and Guevara, E. (2008). *Hole-filled SRTM for the Globe Version 4.* Available from the CGIAR-CSI SRTM 90m Database. Available online at: http://srtm.csi.cgiar.org

Jiang, Q. (2014). Applicability of reduced-gravity shallow-water theory to atmospheric flow over topography. *J. Atmos. Sci.* 71, 1460–1479. doi: 10.1175/JAS-D-13-0101.1

Jiang, Q., and Smith, R. B. (2001). Ideal shocks in 2-layer flow. Part II: under a passive layer. *Tellus A* 53, 146–167. doi: 10.1034/j.1600-0870.2001.00097.x

Klemp, J., and Lilly, D. (1975). The dynamics of wave-induced downslope winds. *J. Atmos. Sci.* 32, 320–339. doi: 10.1175/1520-0469(1975)032<0320:TDOWID>2.0.CO;2

Nappo, C. J. (2012). *An Introduction to Atmospheric Gravity Waves, 2 Edn*. London: Academic Press.

Ralph, F. M., Neiman, P. J., Keller, T. L., Levinson, D., and Fedor, L. (1997). Observations, simulations, and analysis of nonstationary trapped lee waves. *J. Atmos. Sci.* 54, 1308–1333. doi: 10.1175/1520-0469(1997)054<1308:Osaaon>2.0.Co;2

Scorer, R. S. (1949). Theory of waves in the lee of mountains. *Q. J. R. Meteorol. Soc.* 75, 41–56. doi: 10.1002/qj.49707532308

Scorer, R. S. (1997). *Dynamics of Meteorology and Climate*. Chichester: Wiley.

Smith, R. B. (1979). The influence of mountains on the atmosphere. *Adv. Geophys.* 21, 87–230.

Teixeira, M. A. (2014). The physics of orographic gravity wave drag. *Front. Phys.* 2:43. doi: 10.3389/fphy.2014.00043

Teixeira, M. A., Argaín, J. L., and Miranda, P. M. (2013). Orographic drag associated with lee waves trapped at an inversion. *J. Atmos. Sci.* 70, 2930–2947. doi: 10.1175/JAS-D-12-0350.1

Turner, J. S. (1973). *Buoyancy Effects in Fluids*. Cambridge: Cambridge University Press.

Vosper, S. B. (2004). Inversion effects on mountain lee waves. *Q. J. R. Meteorol. Soc.* 130, 1723–1748. doi: 10.1256/qj.03.63

Vosper, S. B., Wells, H., Sinclair, A., and Sheridan, P. F. (2012). A climatology of lee waves over the UK derived from model forecasts. *Meteorol. Appl.* 20, 466–481. doi: 10.1002/met.1311

Wurtele, M., Sharman, R., and Datta, A. (1996). Atmospheric lee waves. *Annu. Rev. Fluid Mech.* 28, 429–476.

Conflict of Interest Statement: The authors declare that the research was conducted in the absence of any commercial or financial relationships that could be construed as a potential conflict of interest.

APPENDIX

Frequency Dispersion Relationship for Trapped Lee Waves

The Taylor-Goldstein equation can be derived from the two-dimensional Euler equations (subject to the Boussinesq approximation), the first law of thermodynamics and the incompressible mass continuity equation after linearization and by postulating the existence of wavelike solutions (see, e.g., Nappo, 2012):

$$\frac{d^2\hat{w}}{dz^2} + \left[l^2 - k^2\right]\hat{w} = 0 \quad . \tag{A1}$$

We solve this equation in two fluid layers by assuming that wave solutions are stationary in both the lower (subscript 1) and the upper one (subscript 2):

$$\hat{w}_1 = A_1 e^{im_1 z'} + B_1 e^{-im_1 z'} \tag{A2}$$

$$\hat{w}_2 = A_2 e^{im_2 z'} + B_2 e^{-im_2 z'} \quad . \tag{A3}$$

Here $\hat{w} = [\rho_s/\rho_0(z)]^{-1/2} \cdot \tilde{w}$, where $\tilde{w}$ denotes a Fourier component of the vertical wind speed perturbation, and ρ_s and ρ_0 the surface density and the unperturbed density profile respectively; $z' = z - h_1$, where h_1 is the thickness of the lower layer.

Four boundary conditions (BCs) are required to close the system. The first two are the parallel flow condition at the surface and a radiation condition in the upper layer. For simplicity, we assume flat terrain with constant interface height ($z' = 0$), a realistic scenario for a lee wave that propagates above a flat surface after being excited by a mountain. The corresponding BCs become then

$$\hat{w}_1(z' = -h_1) = 0 \tag{A4}$$

$$B_2 = 0 \quad . \tag{A5}$$

The other two conditions are the kinematic and the dynamic BC at the interface ($z' = 0$), which consists of a potential temperature jump with reduced gravity $g' = g \cdot \Delta\theta/\theta_0$. The former condition ensures continuous vertical wind speed, while the latter requires continuous pressure across the θ discontinuity. Following Klemp and Lilly (1975) and Vosper (2004), the kinematic and dynamic BCs are respectively:

$$\hat{w}_1 = \hat{w}_2 \tag{A6}$$

$$\frac{d\hat{w}_1}{dz} - \hat{w}_1 \frac{g'}{U^2} = \frac{d\hat{w}_2}{dz} \quad . \tag{A7}$$

Imposing the constraints (A4)–(A7) on Equations (A2) and (A3) and solving for A_1 and B_1 leads to:

$$A_1 = \frac{A_2}{1 - e^{-2im_1 h_1}} \tag{A8}$$

$$B_1 = \frac{A_2}{1 - e^{2im_1 h_1}} \quad . \tag{A9}$$

Both coefficients depend on the amplitude A_2 of the interfacial disturbance. Substituting Equations (A5)–(A9) in Equations (A2) and (A3) and eliminating A_2 results finally in a condition that relates the wind speed with the vertical wave numbers $m_{1,2}$

$$U^2 = \frac{g'}{im_1 \coth\left(im_1 h_1\right) - im_2} \quad . \tag{A10}$$

Equation (A10) is the frequency dispersion relationship that describes interfacial waves on an inversion between two continuously stratified fluid layers.

Two-dimensional Trapped Lee Wave Model

The two-dimensional wave fields in **Figure 4** are obtained by determining the coefficients A_1, A_2, B_1 and B_2 in Equations (A2) and (A3) after imposing a parallel flow condition along topography. Equation (A4) is therefore replaced by:

$$\hat{w}_1(z' = -h_1) = U\frac{dH}{dx} = i\hat{h}kUe^{ikx} \quad , \tag{A11}$$

where H is the height and $\hat{h}$ is the Fourier-series expansion of the terrain profile. Using again (A5)–(A7), and (A11) in Equations (A2) and (A3) yields:

$$A_1 = \hat{w}_{1(z'=-h_1)} e^{im_1 h_1} - B_1 e^{2im_1 h_1} \tag{A12}$$

$$B_1 = \hat{w}_{1(z'=-h_1)} \frac{\alpha \cdot e^{im_1 h_1}}{\beta + \alpha \cdot e^{2im_1 h_1}} \tag{A13}$$

where $\alpha = i\,(m_1 - m_2) - \frac{g'}{U^2}$ and $\beta = i\,(m_1 + m_2) + \frac{g'}{U^2}$. In the upper layer,

$$A_2 = \hat{w}_{1(z'=-h_1)} \cdot e^{im_1 h_1} + B_1 \cdot (1 - e^{2im_1 h_1}) \tag{A14}$$

$$B_2 = 0 \quad . \tag{A15}$$

The full solution in a domain of n horizontal grid points and a length $D = n\Delta x$ is computed independently at each level by summing up all Fourier components:

$$w'_{1,2}(x, z) = [\rho_s/\rho_0(z)]^{1/2} \cdot \mathrm{Re}\left[\frac{1}{n}\sum_{k=0}^{k=2\pi/D} \hat{w}_{1,2}(x, z)\right]. \tag{A16}$$

Horizontal wind speed perturbations $u'_{1,2}$ are determined in a similar fashion, using the incompressibility constraint $\hat{u}_{1,2} = -(m_{1,2}/k) \cdot \hat{w}_{1,2}$.

Since the model described above is solved numerically in spectral space, the boundary conditions are necessarily periodic. This is a critical aspect for trapped lee wave solutions, which are asymmetric with respect to the mountain and do not decay with distance downstream of it. We solve this problem by including an artificial *ghost*-mountain in the domain, downstream of the first. The distance between the two mountains is set so as to achieve complete destructive interference of the lee wave train. The flow field becomes then symmetric. **Figure 4** only shows the left half of the domain.

Chapter 4

The amplitude of lee waves on the boundary-layer inversion

This chapter delivers a new approach for the analytical description of large amplitude lee waves. The main aims of this work were: (i) to develop an analytical model for the amplitude of interfacial lee waves that incorporates nonlinear effects, (ii) to verify the new model against numerical simulations and water tank experiments and (iii) to investigate the regime transition between lee waves and hydraulic jumps in terms of the Froude number and the nondimensional mountain and inversion heights.

The author's contributions are the idea and design of this study as well as the theoretical analysis to extend Lemoine's analytical amplitude model for surface water waves to atmospheric lee waves. Furthermore, he performed the numerical simulations and analyzed the model output and the data of the water tank experiments. The author also prepared the figures and contributed to a large part to the interpretation of the results and the writing of the manuscript.

This paper is submitted to the Quarterly Journal of the Royal Meteorological Society:
(submission date: 26. May 2016)
Sachsperger, J., S. Serafin, V. Grubišić, I. Stiperski, and P. Alexandre, 2016b: The amplitude of lee waves on the boundary-layer inversion. *submitted to Q. J. R. Meteorol. Soc.*

Quarterly Journal of the Royal Meteorological Society *Q. J. R. Meteorol. Soc.* **00: 1–?? (2016)**

The amplitude of lee waves on the boundary-layer inversion

Johannes Sachsperger,[a*] Stefano Serafin,[a] Vanda Grubišić,[b†] Ivana Stiperski[c] and Alexandre Paci[d]

[a] *University of Vienna, Department of Meteorology and Geophysics, Vienna, Austria*
[b] *National Center for Atmospheric Research[‡], Boulder, Colorado*
[c] *University of Innsbruck, Institute of Atmospheric and Cryospheric Sciences, Innsbruck, Austria*
[d] *CNRM-GAME, Météo-France and CNRS, Toulouse, France*

[*] Correspondence to: Johannes Sachsperger, Department of Meteorology and Geophysics, University of Vienna, Althanstraße 14 UZA2, 1090 Vienna, Austria, johannes.sachsperger@univie.ac.at

[†] Additional affiliation: Department of Meteorology and Geophysics, University of Vienna, Vienna, Austria
[‡] The National Center for Atmospheric Research is sponsored by the National Science Foundation

This study presents an analytical model for the amplitude of lee waves on the boundary-layer inversion in two-dimensional flow. Previous linear lee wave models, in which the amplitude depends on the power spectrum of topography, can be inaccurate if the amplitude is large. Our model incorporates nonlinear effects by assuming that lee waves originate at an internal jump downstream of topography. Energy flux convergence at the jump is compensated by the radiation of laminar lee waves. The available energy is estimated using a hydraulic jump model and the resulting wave amplitude is determined from linear theory. According to this model, the amplitude of lee waves depends essentially on their wavelength and on the inversion height difference across the jump. The new amplitude model is verified against numerical simulations and water tank experiments. The agreement between the model and the numerical results is excellent, while the verification with water tank experiments reveals that the accuracy of the model is comparable with that of numerical simulations. Finally, we derive a nonlinearity parameter for interfacial lee waves and discuss the regime transition from lee waves to hydraulic jumps in terms of the Froude number and the nondimensional mountain and inversion heights.

Key Words: Trapped lee waves, surface water waves, wave breaking, hydraulic jump, water tank experiments, numerical simulations

Received . . .

1. Introduction

Lee waves are a special type of internal gravity waves, generated when stratified airflow is lifted over a mountain. Instead of propagating vertically, lee waves are trapped in a layer of finite depth and propagate horizontally over large distances, up to a few hundred kilometers. When condensation occurs in the wave crests, trapped lee waves can be observed in satellite images as cloud stripe patterns in the lee of mountains, with a typical wavelength of 3–15 km. Since lee waves can cause strong vertical motion in their up- and downdrafts, accurate forecasts of this phenomenon are important for aircraft pilots. On the one hand, the strong updrafts allow long and smooth glider flights to high altitudes. On the other hand, they can originate severe low-level turbulence in atmospheric rotors (Doyle and Durran 2007; Strauss et al. 2015) and pose a potential hazard for aviation.

Dynamically, atmospheric trapped lee waves are analogous to waves on a free water surface (Scorer 1949). However, unlike free waves on a stream of water, atmospheric lee waves form in the interior of the fluid. Scorer found that they do not only develop along layer interfaces such as temperature inversions, but may also occur within continuously stratified layers, if vertically propagating waves are reflected downwards (resonant waves). This happens when the parameter $l^2 \approx \frac{N^2}{U^2} - \frac{1}{U}\frac{d^2U}{dz^2}$ (where N is the buoyancy frequency and U the wind speed) decreases with height and the layer in which the wave is reflected is sufficiently deep. Resonant lee waves have been studied extensively in the literature (e.g. Durran 1986b; Wurtele et al. 1996; Teixeira 2014), while interfacial lee waves have been long overlooked and reexamined only recently (Vosper 2004; Teixeira et al. 2013; Sachsperger et al. 2015). Linear theory shows that the wavelength of resonant and interfacial waves depends on the flow profile far upstream of the mountain (Scorer 1949; Vosper 2004) and is independent of the mountain half-width and height (in contrast to vertically propagating internal gravity waves). While linear theory explains well the wavelength, it gives only limited insight into the behaviour of the wave amplitude (Corby and Wallington 1956), because nonlinear effects may be important in that respect.

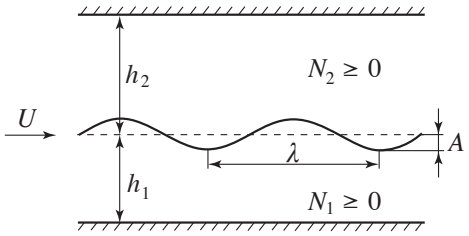

Figure 1. Schematic of two-layer flow in a channel. Symbols U, N_i and h_i represent the mean flow speed, the stratification in the lower ($i = 1$) and upper ($i = 2$) layer and the depths of both layers respectively. The wavelength is denoted by λ and the amplitude by A.

The development of large-amplitude lee waves can be understood also in analogy to shallow water flow over an obstacle. If the obstacle is sufficiently high, the flow is partially blocked upstream of it and a hydraulic jump forms in the lee (Houghton and Kasahara 1968). Dissipation in the jump implies that the flow loses energy in the form of turbulence as it transitions from super- to subcritical. Lord Rayleigh (1914) showed that the amount of energy loss depends on the jump size (altitude difference of the interface across the jump). Observations in laboratory experiments by Favre (1935) revealed that if the jump size is small, the transition to subcritical flow does not lead to energy dissipation, but rather to energy radiation through laminar waves. Motivated by this result, Lemoine (1948) successfully combined the energy source model of Lord Rayleigh with a linear wave model that relates the available energy to the wave amplitude, as described in Benjamin and Lighthill (1954).

Since under certain conditions the behaviour of atmospheric flows is similar to that of hydraulic flow (e.g. Durran 1986a; Vosper 2004), we extend Lemoine's approach in order to determine the amplitude of atmospheric lee waves. To the knowledge of the authors, this has not been done thus far. In this paper, we only focus on lee waves forming on a density discontinuity (e.g. on the boundary-layer inversion), leaving the case of resonant lee waves for future research.

In Section 2, we extend Lemoine's model to atmospheric flows and discuss briefly the hydraulics of two-layer flow. Theoretical results are verified against numerical simulations and water tank experiments, as described in Section 3 and 4. Furthermore, we discuss the large-amplitude limit of lee waves in Section 5 and show that hydraulic jumps correspond to the limiting case of breaking lee waves. Conclusions are drawn in Section 6.

2. Theoretical considerations

In this section, we develop a simple analytical model for the amplitude of lee waves forming on the boundary-layer inversion. The model consists of two components that describe the wave propagation and the energy source separately. The wave-propagation component is based on linear gravity wave theory and relates the wave amplitude with the wave energy flux, while the wave-energy-source component is based on hydraulic theory and gives an estimation of the available energy for wave propagation. We consider two-layer flow with a neutrally stratified lower layer representing a well mixed boundary layer, a continuously stratified upper layer representing the free atmosphere and a temperature inversion at the layer interface.

2.1. *Wave energy propagation*

Whenever waves are excited, they radiate energy away from the energy source, e.g. from an internal jump. It can be shown that, for small amplitude (linear) waves, the rate of energy radiation, i.e., the wave energy flux, is proportional to the lee wave amplitude. We use this property to determine the wave amplitude for a given rate of energy propagation.

The linear wave-energy-propagation model considers a two-layer Boussinesq fluid in a channel, see Fig. 1. The two fluid layers are continuously stratified with $N_i \geq 0$ and are of depth h_i, where the subscript $i \in \{1, 2\}$ denotes the lower and upper layer respectively. In what follows we use $N_1 = 0$, since we consider a well mixed boundary layer, as described above. For the moment, we assume that the fluid is at rest ($U = 0$). The case of a moving fluid is discussed further below.

The wave disturbance between the two layers is assumed to be of form $\eta_0 = A\cos(k(x - Ct))$, where A is the displacement amplitude, $k = 2\pi/\lambda$ is the wavenumber and C is the intrinsic phase speed. The displacement field $\eta_i(x, z)$ in each fluid layer depends on the imposed wave mode η_0 and can be determined using generic solutions to the Taylor-Goldstein equation and zero-displacement boundary conditions at the walls of the channel (see the Appendix for details). The total horizontal and vertical wave energy fluxes are then the sum of the respective fluxes in each fluid layer, defined as (Nappo 2012)

$$EF_x = \int_{-h_1}^{h_2} \overline{p'u'}\, dz' = \int_{-h_1}^{0} \overline{p'_1 u'_1}\, dz' + \int_{0}^{h_2} \overline{p'_2 u'_2}\, dz' \quad \text{and} \tag{1}$$

$$EF_z = \int_{-h_1}^{h_2} \overline{p'w'}\, dz' = \int_{-h_1}^{0} \overline{p'_1 w'_1}\, dz' + \int_{0}^{h_2} \overline{p'_2 w'_2}\, dz' \quad , \tag{2}$$

where $z' = z - h_1$ is the geometric height with respect to the interface, p' is the pressure perturbation and u' and w' are the horizontal and vertical wind speed perturbations. The overbar in the correlation terms represents averaging over one wavelength. Since the wave disturbance is either trapped on the interface or in the channel, its phase lines are vertical and the energy flux EF_z is zero in both layers. The perturbations u'_i and p'_i can be derived from η_i using the phase relationships for internal gravity waves (see Appendix for details). Inserting u'_i and p'_i into Eq. (1) gives the total vertically integrated horizontal energy flux across the channel (in J m^{-1} s^{-1})

$$EF_x = \frac{\hat{\rho}A^2C^3}{4}\left\{ n_1\left[\frac{e^{2n_1h_1} - e^{-2n_1h_1} + 4n_1h_1}{\left(e^{n_1h_1} - e^{-n_1h_1}\right)^2}\right] + n_2\left[\frac{e^{2n_2h_2} - e^{-2n_2h_2} + 4n_2h_2}{\left(e^{-n_2h_2} - e^{n_2h_2}\right)^2}\right]\right\}. \tag{3}$$

Here, $n_i = -(k^2 - N_i^2/C^2)^{1/2}$ is the decay rate of the displacement η with distance from the interface in each layer and $\hat{\rho}$ is the density at the interface. The two terms in the curly brackets of Eq. (3) represent the decay of the energy flux with

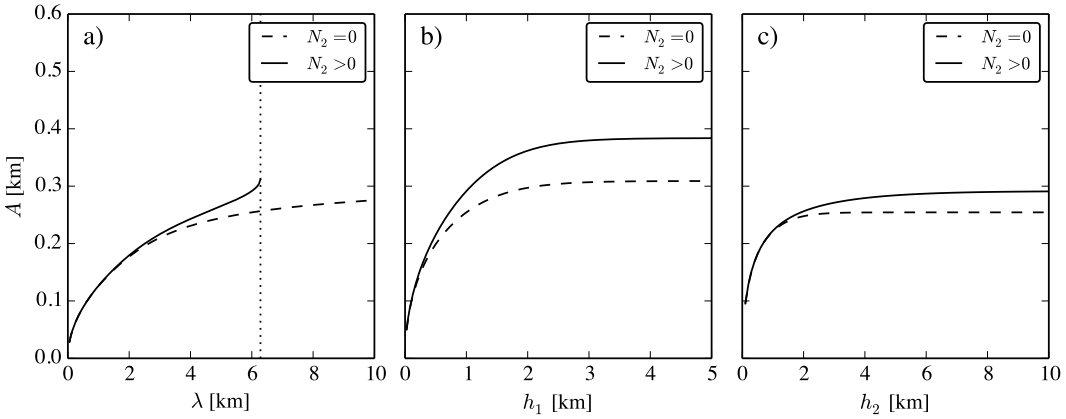

Figure 2. Dependence of the amplitude A on (a) wavelength λ, (b) depth of lower layer h_1 and (c) depth of upper layer h_2. Solid and dashed lines represent different stratifications in the upper layer. The vertically integrated energy flux is taken constant with $EF = -50$ kW m^{-1}. The curves in (a)–(c) are computed from Equation (4) for the following values typical for the atmosphere: $N_1 = 0$, $N_2 = 0.01$ s^{-1}, $U = 10$ m s^{-1}, $h_1 = 1$ km, $h_2 = \infty$, $\lambda = 6$ km and $\rho_0 = 1$ kg m^{-3}.

increasing vertical distance from the interface in the respective layers. Solving Eq. (3) for the amplitude yields

$$A = \sqrt{\frac{4EF_x}{\hat{\rho}C^3}} \left\{ n_1 \left[\frac{e^{2n_1h_1} - e^{-2n_1h_1} + 4n_1h_1}{\left(e^{n_1h_1} - e^{-n_1h_1}\right)^2} \right] + n_2 \left[\frac{e^{2n_2h_2} - e^{-2n_2h_2} + 4n_2h_2}{\left(e^{-n_2h_2} - e^{n_2h_2}\right)^2} \right] \right\}^{-\frac{1}{2}}. \quad (4)$$

So far, we have assumed that the fluid is at rest. In the atmosphere, however, lee waves are excited when flow with speed U (> 0) moves over an obstacle. Since lee waves are typically stationary with respect to a fixed location at the ground ($c = C + U = 0$), the intrinsic phase speed of the wave disturbance η_0 must oppose the mean flow with $C = -U$. In what follows, we emphasize some important properties of Eq. (4) in this context.

First, in order to maintain a real root, the energy flux has to be negative because $C = -U$ is negative. This implies that energy is transported against the wind, similar to internal gravity waves (Nappo 2012).

Second, the amplitude depends significantly (through n_1 and n_2) on the wavelength of the disturbance, as is evident in Fig. 2a. For large wavelengths, a given wave energy flux leads to larger amplitudes than it does for smaller wavelengths. However, if the upper layer is stratified, a cut-off wavelength exists above which wave energy propagates vertically without being trapped at the interface (Sachsperger et al. 2015). Consequently, the solid curve ($N_2 > 0$) in Fig. 2a ends at the cut-off wavelength (dotted line, where $k^2 = N_2^2/U^2$), while the dashed line ($N_2 = 0$) extends to longer waves.

Third, the amplitude becomes independent of the layer depths beyond a certain threshold. This happens when the wave disturbance is damped out in the vertical before it can be reflected from the boundaries, i.e., when n_ih_i is large.

The only a-priori-unknown parameter in Eq. (4) is the wave energy flux EF_x, which needs to be parameterized. This can be done using a hydraulic jump model for the amount of energy that becomes available at an internal jump, as explained in what follows.

2.2. *Wave energy source*

It is instructive to consider first the relatively simple case of an external jump on the free surface of a single shallow fluid layer. The fluid has constant density and expands rapidly in depth at the jump. Assuming mass and momentum conservation in the layer, it can be shown that the energy flux converges at the jump (Baines 1995, p. 37). As mentioned above, the energy accumulated by energy flux convergence can either be dissipated in a jump or radiated in waves.

Similarly, the energy flux converges at an internal jump between two fluid layers of different density. In this case, however, momentum (in contrast to mass) is not conserved in the individual fluid layers, but only in the entire column. Since there is only one momentum conservation condition for two fluid layers, the system is underdetermined and requires a closure (Yih and Guha 1955). One possibility to close the system is to assume energy conservation in one of the layers, while the energy flux convergence occurs in the other (Wood and Simpson 1984). The comparison with laboratory experiments and numerical simulations suggests that assuming energy conservation in the lower (expanding) layer and energy accumulation in the upper (contracting) layer is more realistic, as shown by Klemp et al. (1997, hereafter KRS). In this work, we use the KRS model to estimate the available energy at an internal jump.

For the flow sketched in Fig. 3, the energy flux convergence at the internal jump is (according to KRS)

$$\Delta EF = -\frac{\hat{\rho}U^3 d(d-h_a)(d-2h_f)(h_f-h_a)^3}{2h_f^2(d-h_f)^2(2d-h_f-h_a)} \quad [\text{J m}^{-1}\text{ s}^{-1}]. \quad (5)$$

Here, d is the channel depth, while h_f and h_a denote the interface height upstream and downstream of the jump respectively. The horizontal wind speed U is vertically uniform and $\hat{\rho} = (\rho_1 + \rho_2)/2$ is the fluid density at the interface. The densities in both fluid layers are assumed to be constant. In the case of stratified fluid layers (e.g., in the atmosphere) the constant density approximation is reasonable provided that the layers are shallow compared to their scale depth. Eq. (5) differs from the KRS model by a minus sign. This is required, because the jump moves in the opposite direction in our case. A detailed derivation of Eq. (5) is out of the scope of this paper and can be found in KRS and Li and Cummins (1998). The expression for the energy flux convergence in Eq. (5) can be cast in nondimensional form using the parameters $\Delta EF/(\hat{\rho}U^3h_a)$, $\alpha = h_a/d$ and $\beta = h_a/h_f$

$$\Delta EF/(\hat{\rho}U^3h_a) = -\frac{(1-\alpha)(1-2\alpha\beta)(\alpha\beta-\alpha)^3}{\alpha^3\beta^2(1-\alpha\beta)^2(2-\alpha\beta-\alpha)} \quad (6)$$

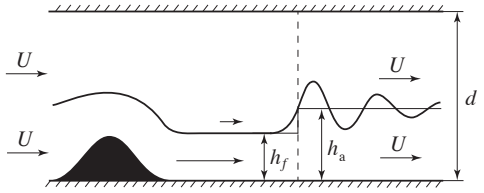

Figure 3. Schematic of shallow water flow over a mountain. The vertical dashed line represents the location of readjustment of the shooting flow (depth h_f) to the undisturbed downstream layer height (h_a).

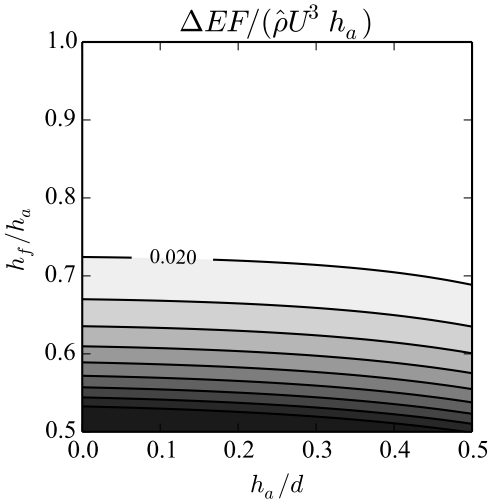

Figure 4. Impact of nondimensional channel depth (x axis) and nondimensional jump size (y axis) on the nondimensional energy flux convergence $\Delta EF/(\hat{\rho}U^3 h_a)$ (shades and contours). Contour values every 0.02 are drawn.

The dependence of the nondimensional energy flux convergence on channel depth and jump size is shown in Fig. 4 for the most relevant parameter space in the context of lee waves. Clearly, the influence of the jump size dominates over that of the channel depth d. It is also apparent that the impact of d can be neglected for an infinitely deep layer ($\Delta EF/(\hat{\rho}U^3 h_a)$ becomes independent of h_a/d as $h_a/d \to 0$). Therefore, the KRS model, which is developed for flow in a channel with rigid lid conditions at the boundaries, can be applied to atmospheric flows.

The wave-propagation model (Eq. 4) can be coupled with the energy-source model (Eq. 5) assuming that $EF_x = \Delta EF$, i.e., no dissipation occurs at the jump. This is explained more in detail in Section 4 below.

3. Data and experimental design

In order to verify the analytical amplitude model presented in the previous section, we use numerical simulations and data from observations in water tank experiments. A description of the two data sources is presented in what follows.

3.1. Numerical model

Numerical simulations of two-layer atmospheric flow with a temperature inversion at the layer interface are carried out with the Bryan Cloud model (CM1; Bryan and Fritsch 2002; Doyle et al. 2011). CM1 is a fully nonlinear and nonhydrostatic large-eddy-simulation model. The model equations are integrated using a third-order Runge-Kutta scheme in time and a fifth-order finite-difference scheme in space. Sub-grid scale turbulent fluxes are parameterized after Deardorff (1980). The computational domain is two-dimensional and spans $n_x \times n_z = 2880 \times 145$ grid points in the horizontal and vertical directions with an isotropic grid spacing of $\Delta x = \Delta z = 50$ m in the layer where lee waves are expected to form (below $z = 2$ km). Above $z = 2$ km, the vertical grid spacing increases linearly to $\Delta z = 200$ m at $z = 7$ km and remains constant until the model top. At $x_0 = 55$ km a gaussian shaped mountain of the form

$$h(x) = H \exp\left[-(x - x_0)^2/2\sigma^2\right] \tag{7}$$

is placed. Using $\sigma = 1.744$ km results in an approximate mountain half width of $L = 5$ km at the surface. In the experiments described below, two different mountain heights $H = 200$ m and $H = 1000$ m are used.

The boundary conditions are open-radiative at the inflow and outflow boundaries, while they are periodic in cross-stream direction. To minimize spurious wave reflections from the domain boundaries, Rayleigh damping is applied in a 40-km-wide zone at each of the streamwise boundaries and above $z = 10$ km. The undamped part of the domain, i.e. the physical domain, spans $40 < x < 104$ km and $0 < z < 10$ km, which is the region where lee wave formation is expected. In addition to minimizing reflections, we also reduce artifacts arising from the abrupt model start by accelerating the flow from rest to the designated flow speed ($U = 10$ m s^{-1}) in the first simulation hour (the total integration time is 200 min). Furthermore, since we use the simulations to verify the frictionless analytical amplitude model, free-slip lower boundary conditions are applied. The details of the two-layer flow configuration (e.g. stratification, inversion height and strength) depend on the experiment and are described in Section 4.

3.2. Water tank experiments

In addition to numerical simulations, we use water tank measurements of density-stratified two-layer flow over two-dimensional topography, taken during the HYIV-CNRS-SECORO experiments (Stiperski et al. 2016). Laboratory experiments are useful to study interfacial waves, because the flow can be controlled and environmental influences are minimized, in contrast to measurements of atmospheric flows in the field. Therefore, laboratory flows are expected to compare well with theory. HYIV-CNRS-SECORO was carried out to acquire observational evidence of lee wave interference over double-mountain orography (Grubišić and Stiperski 2009; Stiperski and Grubišić 2011). In total, 395 experiments were carried out using both single- and double-mountain obstacles. The density profiles of the fluid represent typical boundary layer flow with two layers, the lower one neutrally stratified ($N_1 = 0$) and the upper one continuously stratified ($N_2 > 0$), with a density jump $\Delta\rho$ between the layers. A gaussian shaped obstacle (Eq. 7) was towed at various speeds along the bottom boundary. Depending on the Froude number $Fr = U/(g'h_1)^{1/2}$ and the nondimensional mountain height H/h_1, different flow responses have been observed to occur in the lee; $g' = g\Delta\rho/\rho_0$ and H are reduced gravity and mountain height respectively. The flow responses for the single mountain experiments were subjectively categorized into two types of response (lee waves and hydraulic jumps). The dependence of the flow types on Fr and H/h_1 is shown in Fig. 5. In this work, we focus on a subset of the single-mountain lee wave cases only. Further details on the HYIV-CNRS-SECORO experiments can be found in Stiperski et al. (2016).

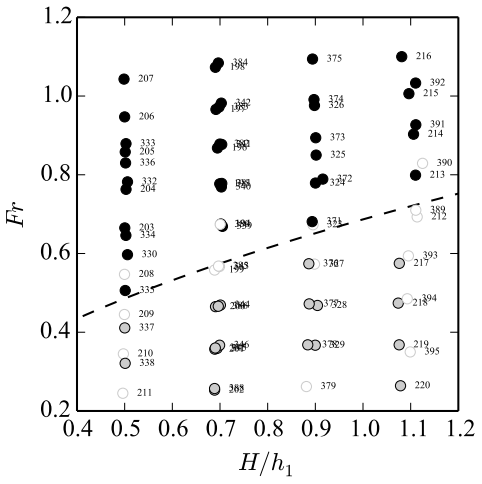

Figure 5. Single-mountain regime diagram in HYIV-CNRS-SECORO, as a function of Froude number Fr and nondimensional mountain height H/h_1. The flow regimes are lee waves (black dots) and hydraulic jumps (grey dots). White dots indicate experiments in which the flow response is ambiguous or could not be identified. The dashed line represents the curve $\gamma = 1$ (Eq. (10) with $NH/U = 0.5$) and marks the transition from lee waves to hydraulic jumps. See Section 5 for details.

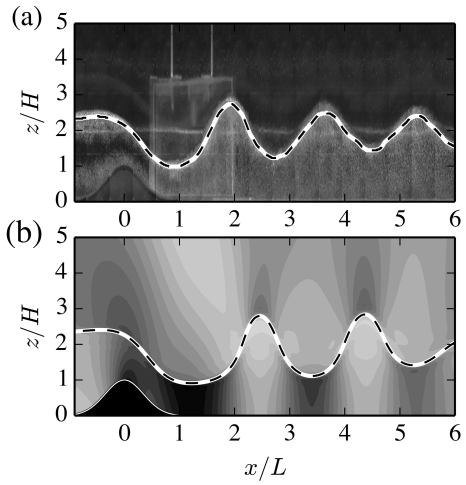

Figure 6. Comparison of (a) water tank experiment Nr. 203 (see Tab. 1b) with (b) the corresponding numerical simulation. Grey shades in (a) indicate particle density and grey shades in (b) indicate u' between -10 m s^{-1} (light grey) and 10 m s^{-1} (black) at an increment of 1 m s^{-1}. The black dashed line indicates the displacement of the layer interface in each panel. Spatial dimensions are nondimensionalized with the mountain height H and half width L. The mountain is represented by the black shape in the left part of the panels.

3.3. Scaling between numerical simulations and water tank experiments

Since the atmospheric numerical simulations ($\rho \sim 1$ kg m^{-3}, horizontal scale ~ 1000 m) are on a different scale than the laboratory experiments ($\rho \sim 1000$ kg m^{-3}, horizontal scale ~ 1 m), we need to determine the simulation setup in order to achieve comparable results. Scaling arguments suggest that flow responses at different scales will be similar when fundamental nondimensional numbers, depending on the physical parameters of the system, are constant. In our case, keeping the vertical aspect ratio H/L of the mountain and the nonlinearity parameter NH/U constant, allows to retain the wave structure in the continuously stratified upper layer (Baines 1995, p 237). Likewise, the interface response in the lee of the mountain is similar when the nondimensional mountain height H/h_1 and Froude number Fr are constant (Houghton and Kasahara 1968). In addition, keeping these dimensionless parameters constant also retains the nondimensional wavenumber Lk across scales, as becomes apparent in the expression

$$Lk = \frac{1}{2}\frac{L}{H}\frac{H}{h_1}Fr^{-2}\,. \tag{8}$$

Here, we have used $k = g'/(2U^2)$, which is valid for interfacial waves in deep-water flow (i.e. when $kh_1 \gg 1$, Turner 1973). Eq. (8) is an important result because it proves that the applied scaling parameters will also keep the lee wavelength in scale with the obstacle. This becomes evident also in the flow comparison in Fig. 6. The flow response in the water tank experiment and the corresponding numerical simulation is similar, although the spatial scale is different by a factor 1000. Details on the scaling of the wave amplitude are provided in Section 5.

4. Results

Using the data sources described above, two sets of experiments are carried out. First, idealized numerical simulations are made in order to verify the linear relationship between the amplitude and the wave energy flux (Eq. 4). Second, observed amplitudes in laboratory flows and corresponding numerical simulations are compared with estimations of the analytical amplitude model with parameterized energy source (Eq. 4 and 5).

4.1. Experimental design

In the first experiment, which we refer to as the *energy-flux experiment*, we compare the wave amplitudes measured in numerical simulations with those estimated using the linear model in Eq. (4). In particular, we use Eq. (4) to obtain an amplitude estimate from the wave energy flux EF_x computed from the numerical simulations. The simulations are initialized with two-layer flow and different inversion strengths (Tab. 1a). From the simulations we determine EF_x according to Eq. (1). The covariance $\overline{p'u'}$ is computed from the simulated pressure and horizontal wind speed field, averaged over one wavelength and integrated vertically in the layer $-h_1 < z' < h_2 = h_1$, which is symmetric about the interface height. Averaging over more than one wave crest, as well as averaging over a layer deeper than $d = 2h_1$, did not show a significant effect on the results. The amplitude and wavelength of the simulated lee wave are determined from the displacement of the isentrope in the center of the inversion layer, $\theta_{inv} = \theta_0 + \Delta\theta/2$. In these simulations the mountain height is $H = 200$ m.

In the second experiment, which we refer to as the *amplitude experiment*, we compare the measured amplitudes of the simulations A_{sim} and water tank experiments A_{obs} with the amplitude A_{th} estimated from Eq. (4) and (5). The numerical simulations in the amplitude experiment are similar to those in the energy-flux experiment, except for the flow setup. The upstream flow conditions (N_2, h_1 and $\Delta\theta$) correspond to those of the water tank experiments and are determined from scaling arguments, that is, preserving H/h_1, NH/U and Fr. Also, a higher mountain ($H = 1000$ m) is used in order to achieve typical values for the atmospheric boundary-layer-inversion height h_1 (determined from H/h_1). The details are shown in Tab. (1b).

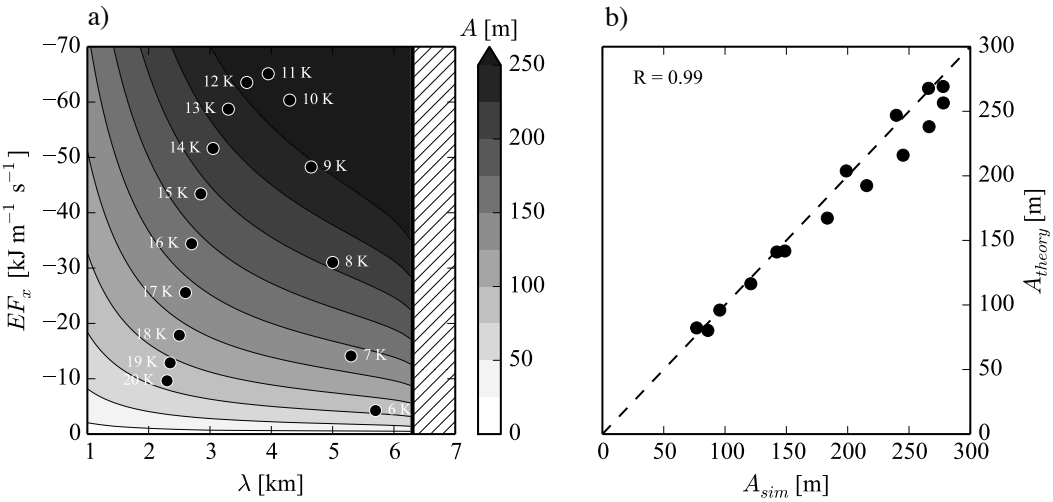

Figure 7. Verification of the amplitude-energy-flux relation, Eq. (4). The figure shows (a) amplitudes A calculated from Eq. (4) as a function of EF_x and λ (grey shades) and measured EF_x and λ from the numerical simulations of the linear experiment at $t = 200$ min (black dots); (b) scatter plot of the measured amplitude in the simulations and the respective linear theory values, taken from the grey shades in (a). R represents the Pearson correlation coefficient.

In order to determine A_{th}, we begin with estimating the available energy flux ΔEF using Eq. (5). To this end, we need to know the upstream flow parameters (N_2, U, $\Delta\theta$, h_1 and d) and the downstream jump parameters (h_a, h_f and λ). The former are known a priori, while the latter are obtained from the interface displacement in the simulations and water tank experiments. We determine h_f as the minimum interface height in the lee of the mountain and h_a as the mean interface height in the wave period with the largest amplitude (see Fig. 3). Once h_f and h_a are known, ΔEF can be calculated with Eq. (5). Assuming that $EF_x = \Delta EF$, i.e., the wave energy flux equals the energy accumulation at the hydraulic transition, we can finally estimate the amplitude A_{th} using Eq. (4). The results from the energy-flux and amplitude experiments are presented below.

4.2. *Energy-flux experiment*

We begin by examining the wavelengths and wave energy fluxes obtained from numerical simulations. In the corresponding model runs, the inversion strength $\Delta\theta$ has been varied. According to interfacial wave theory (Vosper 2004; Sachsperger et al. 2015) an increasing inversion strength leads to a shorter wavelength λ. Respectively, λ varies between 2.3 and 5.7 km, as shown in Fig. 7a (black dots). In addition to the wavelength, the inversion strength also impacts the wave energy flux EF_x in the lee wave train, which reaches a maximum for $\Delta\theta = 11$ K ($Fr = 0.52$). This energy flux maximum can be explained by means of shallow water theory, which predicts a maximum of the jump size $h_a - h_f$ for $Fr \simeq 0.5$ (Fig. 12 in Houghton and Kasahara 1968). Both λ and EF_x impact the amplitude $A = \max(\eta_0)$ of the lee wave (see Eq. 4). The values of A predicted by Eq. 4 in the parameter space spanned by the simulations are shown as grey shades in Fig. 7a. It appears, that simulations with different values of EF_x can have similar amplitude. For example, this is the case for $\Delta\theta = 14$ K and $\Delta\theta = 8$ K where EF_x differs by about 40%, but the maximum displacement is $A \approx 200$ m in both cases.

The comparison of the linear amplitude estimates (grey shades in Fig. 7a) with the amplitudes obtained from the simulations is presented in Fig. 7b. The agreement between theory and simulations is excellent, even when amplitudes are large. In the extreme case, the amplitude is almost 300 m, which is about one third of the lower layer height ($h_1 = 1000$ m).

4.3. *Amplitude experiment*

In this experiment we carry out an intercomparison of the wave amplitudes obtained from the water tank experiments, the numerical simulations and the analytical amplitude model with parameterized energy source (Eq. 4 and 5). We begin with the comparison of the water tank experiments with the numerical simulations, which are expected to be most accurate in reproducing the laboratory flows. Then, the laboratory experiments are compared with the analytical model. Finally, the analytical model is compared with the numerical simulations.

In both the water tank experiments and the simulations, we determine the amplitude from the largest lee wave crest and nondimensionalize it with the mountain height in order to make the results comparable. Fig. 8a shows that simulations and observations are in good agreement. There is significant scatter with a linear correlation coefficient (Pearson) of $R = 0.76$ (a similar value results for the wavelength $R = 0.75$, not shown). A large part of the scatter likely results from the different boundary condition at the top of the fluid. While the laboratory flows are of finite depth and allow reflections of vertically propagating internal waves from the free water surface, those disturbances are absorbed before reaching the upper boundary in the numerical simulations and do not impact the low level flow. Scatter may also arise from friction at the bottom and the side walls of the tank, while the simulations are carried out with a free slip lower boundary condition.

The results of the comparison between theory and numerical simulations is shown in Fig. 8b. The agreement between the two is very good, despite the fact that the theoretical model systematically overestimates the wave amplitude. Since the amplitude-energy-flux relationship (Eq. 4) is very accurate (see Fig. 7b), the systematic error has to arise mainly from the energy source model (Eq. 5). It is reasonable to expect that Eq. 5 overestimates the available energy of the simulated flows. In the numerical simulations, the upper layer is stratified and supports vertically propagating wave disturbances which transport energy

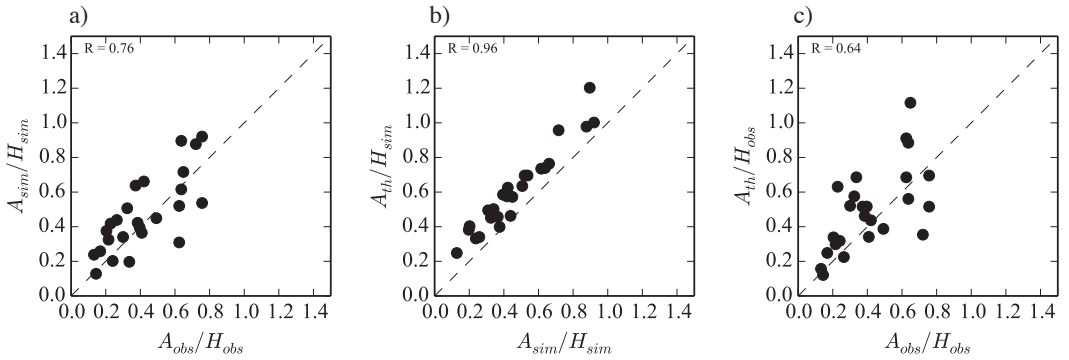

Figure 8. Intercomparison of the wave amplitudes obtained from water tank experiments (subscript obs), numerical simulations (subscript sim) and the analytical model assuming $EF_x = \Delta EF$ (subscript th). R represents the Pearson correlation coefficient.

upward. Since stratification effects are neglected in the KRS model (Eq. 5), vertical wave propagation is not supported and no energy leakage occurs, causing the overestimation of available energy. Another process that might play a role is topographic blocking of the upstream flow, which reduces the mass and energy flux over the obstacle. Since Eq. 5 neglects blocking effects, fluxes upstream of the jump, as well as amplitudes, are overestimated. A detailed analysis on the impact of these two processes on the energy budget of the flow is out of the scope of the paper and left for future research. In any case, the influence of these processes on the present results is marginal.

In Fig. 8c the comparison of theory with water tank experiments is presented. Again, the agreement is reasonably good, considering that the comparison of the laboratory flows with numerical simulations showed large scatter as well (Fig. 8a).

In summary, we showed that wave amplitudes are proportional to the wave energy flux even when amplitudes are large (Fig. 7b). Furthermore, the verification of the analytical amplitude model (Eq. 4 and 5) showed very good agreement with the numerical simulations (Fig. 8b). In a third test, we found that the performance of the analytical model is comparable to that of numerical simulations in predicting the wave amplitude in water tank experiments (Fig. 8a and 8c).

5. Discussion

The amplitude model described in Section 2 and 4 can be used to understand the conditions under which an interfacial lee wave reaches critical amplitude and breaks. In general, wave breaking occurs when the horizontal wind speed perturbation opposes the mean flow causing stagnation, i.e., when $|u'/U| \gtrsim 1$ (Baines 1995). For vertically propagating hydrostatic waves in a continuously stratified atmosphere this happens when the nonlinearity parameter $NH/U \gtrsim 1$. Similarly, lee waves at an inversion can break up into a hydraulic jump if their amplitude is sufficiently large. In analogy to NH/U, a nonlinearity parameter can be formulated also for interfacial waves.

The relevance of NH/U as a nonlinearity parameter for internal gravity waves is described by Baines (1995, p. 239). The scale for u' is derived from the scale for w' using the incompressible mass continuity constraint $|\partial u'/\partial x| = |\partial w'/\partial z|$. For flow over a mountain with scales H and L, the vertical wind speed perturbation and its vertical gradient are obtained from the parallel flow condition as $w' = U\partial h/\partial x \sim UH/L$ and $|\partial w'/\partial z| \sim NH/L$; $\partial/\partial z \sim N/U$ since U/N is the maximum vertical displacement in stratified flow (Smith 1990). It follows that the horizontal wind speed perturbation scales as NH, and correspondingly that $|u'/U| \sim NH/U$.

A similar approach can be used for interfacial waves in two-layer flow. The parallel flow condition along the wave disturbance η_0 gives an expression for the vertical wind speed perturbation $w' = U\partial\eta_0/\partial x \sim UA/L$, where A is the amplitude and L is the characteristic length scale of the interfacial wave. Since the trapped wave is evanescent in the upper layer, its amplitude decays exponentially with height according to $w'\mathrm{e}^{n_2 z'}$. Thus, the vertical gradient of w' at the interface ($z' = 0$) scales approximately as $\partial w'/\partial z \sim An_2U/L$. Using again the continuity equation for the horizontal wind speed perturbation yields $u' \sim An_2U$ and

$$|u'/U| \sim |An_2| = \left| \left[A^2k^2 - (NA/U)^2 \right]^{1/2} \right| \quad . \tag{9}$$

In order to determine this nonlinearity parameter entirely from the upstream flow profile, we need to scale the horizontal wavenumber k and the amplitude A. For k, we use the frequency dispersion relationship of lee waves on the boundary-layer inversion $k = g'/(2U^2) + N^2/(2g')$, which is accurate for waves in deep-water flow (when $kh_1 \gg 1$, Sachsperger et al. 2015). For the amplitude, we use the mountain height H, which is a good approximation for large amplitude lee waves (for which $h_a - h_f$ is large). With these two scales, Eq. (9) can be rearranged to

$$|u'/U| \sim \left| \left[\left(\frac{1}{2}\frac{H}{h_1} Fr^{-2} \right)^2 - \frac{1}{2}(NH/U)^2 + \frac{\sigma}{4} \right]^{1/2} \right| = \gamma \quad , \tag{10}$$

where $\sigma = (UN/g')^2$ is the ratio between the perturbation pressure associated with waves above the inversion ($\sim NU$) and the density jump across the inversion ($\sim g'$) (Jiang 2014). In the case of nonhydrostatic lee waves, σ is small (Sachsperger et al. 2015) and therefore neglected. Since γ depends only on the characteristic nondimensional numbers of the system, it becomes clear that the ratio $|u'/U|$, i.e. the nonlinearity of the wave, is constant across scales as well.

According to the breaking criterion $|u'/U| \gtrsim 1$, lee waves must reach critical amplitude if the parameter γ in Eq. (10) exceeds unity. The isoline of $\gamma = 1$ (with $NH/U = 0.5$; NH/U ranges in the experiments between 0.3 and 0.6) is overlaid (dashed line) on the flow regimes of the water tank experiments in Fig. 5. It is apparent that this line accurately reproduces the regime transition between lee waves and hydraulic jumps. A similar result can be obtained by overlaying this contour (black dashed) over the regime diagram by Vosper (2004), see Fig. 9. This analysis suggests that hydraulic jumps correspond to the limiting

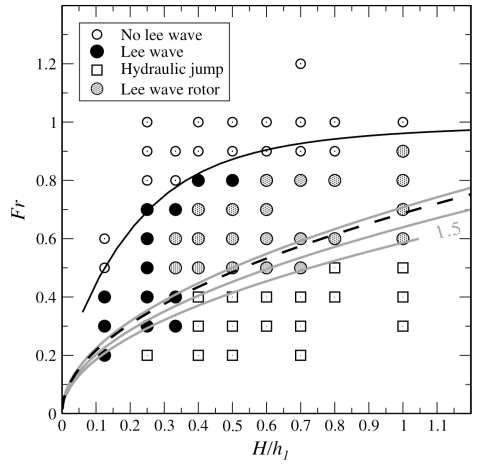

Figure 9. Regime diagram [adapted from Vosper (2004)] for different flow responses (lee waves, lee waves rotors and hydraulic jumps) determined from two-dimensional numerical simulations. The dashed line shows the contour $\gamma = 1$ (Eq. (10) with $NH/U = 0.5$) and indicates the transition from lee waves $\gamma < 1$ to hydraulic jumps $\gamma > 1$. Grey solid lines represent the influence of stratification showing $\gamma = 1$ for $NH/U = 0, 1, 1.5$; the lowest line represents $NH/U = 1.5$. The solid line represents the critical Froude number for which lee waves are possible.

case of breaking lee waves. Moreover, Fig. 9 reveals that free-atmospheric stratification has relatively weak influence on γ. Although $NH/U = 0, 0.5, 1, 1.5$ (black dashed and grey lines) is varied substantially, the difference between the curves is relatively small. Consequently, the first term in the square brackets in Eq. (10) is dominant and stratification only has a second order effect on the breaking of lee waves.

6. Summary and Conclusions

We have extended Lemoine's (1948) theoretical model for the amplitude of surface water waves to atmospheric flows, in order to determine the amplitude of interfacial lee waves. The model consists of two parts that describe the wave propagation and the energy source separately. The accuracy of the theoretical model in predicting measured wave amplitudes in water tank experiments is comparable to that of high resolution numerical simulations. Moreover, the comparison of the theoretical results with the simulations is excellent, even for large-amplitude lee waves. Given the good agreement between theory, simulations and measurements, we may draw further conclusions on the dynamics of atmospheric lee waves on the boundary-layer inversion.

Our investigations confirm Scorer's (1949) statement that the dynamics of interfacial lee waves are similar to those of surface water waves. This becomes apparent as the extended Lemoine model can explain well the amplitude behaviour of atmospheric interfacial lee waves. In analogy to surface water waves, interfacial lee waves develop when the flow over the mountain transitions from subcritical to supercritical at the crest. According to single layer hydraulic theory, this happens when $H/h_1 - (3/2Fr^{3/2} + 1/2Fr^2) \geq 1$ (Baines 1995, p 39) and leads to the formation of a downstream hydraulic jump at which energy accumulates. We showed, using the hydraulic model by Klemp et al. (1997), that the amount of available energy and, thus, the lee wave amplitude, depends on the size of the jump, i.e. the height difference of the interface across the jump.

Modeling the energy source of the wave appropriately is crucial for accurate wave amplitude predictions. This is likely the reason why traditional linear models are highly inaccurate in predicting the amplitude of lee waves (an issue that was raised by Corby and Wallington, 1956, and Vosper, 2004). Those models link the energy source to the power spectrum of the topography. This is relatively accurate for vertically propagating mountain waves (Durran 1992), which are generated at the ground, but inaccurate for interfacial lee waves, which originate at the density interface further aloft in the interior of the fluid. Consequently, their characteristics are not directly determined by topography, rather they depend on the dynamics of two-layer flow over a mountain and nonlinear effects may be important. Therefore, hydraulic theory is more appropriate to describe the energy source, while linear theory is still accurate enough to describe the propagation of the wave, as becomes apparent in Fig. 7b.

Lastly, we showed that hydraulic jumps correspond to the limiting case of breaking lee waves. In analogy to NH/U, which describes the nonlinearity $|u'/U|$ of internal gravity waves, we derived a nonlinearity parameter $\gamma \sim |u'/U|$ (Eq. 10) for interfacial waves in deep water flow ($kh_1 \gg 1$). We showed that the wave breaking criterion ($\gamma \gtrsim 1$) accurately predicts the regime transition between lee waves and hydraulic jumps in water tank experiments and simulations (Vosper 2004). The breaking of lee waves can also be interpreted with hydraulic theory. If energy accumulation at the internal jump is too large to be radiated by lee waves, the available energy is converted to turbulent kinetic energy forming a hydraulic jump.

In this work, we focused on interfacial lee waves on the boundary-layer inversion. However, it is reasonable to expect that the dynamics of resonant lee waves are similar, since the interface behaviour is analogous to hydraulic flow (Durran 1986a). Whether Lemoine's approach can be successfully applied to determine the amplitude of resonant waves remains to be clarified in future research.

Acknowledgements

We gratefully acknowledge Anne Belleudy, Radiance Calmer and Frédéric Murguet for the data acquisition during the HYIV-CNRS-SECORO experiments (European Community's 7th Framework Programme, Integrating Activity HYDRALAB IV, Contract no. 261520). Also, we thank Richard Rotunno for his suggestions on an early version of this work, which improved the manuscript. Numerical simulations were performed on the Vienna Scientific Cluster (VSC). This study was supported by the FWF (Austrian Science Fund) grant P24726-N27 to the University of Vienna.

7. Appendix

7.1. *Displacement field*

The displacement field $\eta_i(x, z)$ in the stratified fluid layers $i \in \{1, 2\}$ can be determined from generic solutions to the Taylor-Goldstein equation in each layer

$$\eta_i(x, z') = \cos(k(x - Ct)) \left[a_i e^{n_i z'} + b_i e^{-n_i z'} \right] \quad . \tag{11}$$

The coefficients a_i and b_i need to be determined from the boundary conditions. Zero-displacement conditions at the walls of the channel give

$$\eta_1(x, z' = 0) = a_1 \left[1 - e^{-2n_1 h_1} \right] \cos(k(x - Ct)) \tag{12}$$

$$\eta_2(x, z' = 0) = a_2 \left[1 - e^{2n_2 h_2} \right] \cos(k(x - Ct)) \tag{13}$$

and the interface condition $\eta_i(x, z' = 0) = \eta_0 = A\cos(k(x - Ct))$ yields the wave displacements

$$\eta_1(x, z') = \eta_0 \left[\frac{e^{n_1(z'+h_1)} - e^{-n_1(z'+h_1)}}{e^{n_1 h_1} - e^{-n_1 h_1}} \right] \tag{14}$$

$$\eta_2(x, z') = \eta_0 \left[\frac{e^{n_2(z'-h_2)} - e^{-n_2(z'-h_2)}}{e^{-n_2 h_2} - e^{n_2 h_2}} \right] . \tag{15}$$

Using $w_i' = \partial\eta_i/\partial t$, the wave perturbations u_i' and p_i' can be derived using the polarization relations of internal gravity waves (Nappo 2012) and become

$$u_1' = n_1 C\eta_0 \left[\frac{e^{n_1(z'+h_1)} + e^{-n_1(z'+h_1)}}{e^{n_1 h_1} - e^{-n_1 h_1}} \right] \tag{16}$$

$$u_2' = n_2 C\eta_0 \left[\frac{e^{n_2(z'-h_2)} + e^{-n_2(z'-h_2)}}{e^{-n_2 h_2} - e^{n_2 h_2}} \right] \tag{17}$$

$$p_1' = n_1 C^2 \rho_0 \eta_0 \left[\frac{e^{n_1(z'+h_1)} + e^{-n_1(z'+h_1)}}{e^{n_1 h_1} - e^{-n_1 h_1}} \right] \tag{18}$$

$$p_2' = n_2 C^2 \rho_0 \eta_0 \left[\frac{e^{n_2(z'-h_2)} + e^{-n_2(z'-h_2)}}{e^{-n_2 h_2} - e^{n_2 h_2}} \right] . \tag{19}$$

References

Baines, P. G., 1995: *Topographic effects in stratified fluids*. Cambridge University Press, 482 pp.

Benjamin, T. B. and M. Lighthill, 1954: On cnoidal waves and bores. *Proc. Roy. Soc. Lond. A Mat.*, **224**, 448–460.

Bryan, G. H. and J. M. Fritsch, 2002: A benchmark simulation for moist nonhydrostatic numerical models. *Mon. Weather Rev.*, **130**, 2917–2928.

Corby, G. and C. Wallington, 1956: Airflow over mountains: The lee-wave amplitude. *Q. J. R. Meteorol. Soc.*, **82**, 266–274.

Deardorff, J. W., 1980: Stratocumulus-capped mixed layer derived from a three-dimensional model. *Bound.-Lay. Meteorol.*, **18**, 495–527.

Doyle, J. D. and D. R. Durran, 2007: Rotor and subrotor dynamics in the lee of three-dimensional terrain. *J. Atmos. Sci.*, **64**, 4202–4221.

Doyle, J. D. et al., 2011: An intercomparison of T-REX mountain wave simulations and implications for mesoscale predictability. *Mon. Weather Rev.*, **139**, 2811–2831.

Durran, D. R., 1986a: Another look at downslope windstorms. Part I: The development of analogs to supercritical flow in an infinitely deep, continuously stratified fluid. *J. Atmos. Sci.*, **43**, 2527–2543.

Durran, D. R., 1986b: Mountain waves. *ed P. S. Ray (Boston, MA: American Meteorological Society)*, 472–492.

Durran, D. R., 1992: Two-layer solutions to long's equation for vertically propagating mountain waves: How good is linear theory? *Q. J. R. Meteorol. Soc.*, **118**, 415–433.

Favre, H., 1935: *Etude théorique et expérimentale des ondes de translation dans les canaux découverts*. Dunod.

Grubišić, V. and I. Stiperski, 2009: Lee-wave resonances over double bell-shaped obstacles. *Journal of the atmospheric sciences*, **66**, 1205–1228.

Houghton, D. D. and A. Kasahara, 1968: Nonlinear shallow fluid flow over an isolated ridge. *Commun. Pur. Appl. Math.*, **21**, 1–23.

Jiang, Q., 2014: Applicability of reduced-gravity shallow-water theory to atmospheric flow over topography. *J. Atmos. Sci.*, **71**, 1460–1479.

Klemp, J. B., R. Rotunno, and W. C. Skamarock, 1997: On the propagation of internal bores. *Journal of Fluid Mechanics*, **331**, 81–106.

Lemoine, R., 1948: Sur les ondes positives de translation dans les canaux et sur le ressaut ondulé de faible amplitude. *Houille Blanche*, **2**, 183–185.

Li, M. and P. F. Cummins, 1998: A note on hydraulic theory of internal bores. *Dynamics of atmospheres and oceans*, **28**, 1–7.

Nappo, C. J., 2012: *An introduction to atmospheric gravity waves*. 2d ed., Academic Press, 359 pp.

Lord Rayleigh, 1914: On the theory of long waves and bores. *Proc. Roy. Soc. Series A, Papers 6*, **90**, 324–328.

Sachsperger, J., S. Serafin, and V. Grubišić, 2015: Lee waves on the boundary-layer inversion and their dependence on free-atmospheric stability. *Frontiers in Earth Science*, **3 (70)**.

Scorer, R., 1949: Theory of waves in the lee of mountains. *Quart. J. Roy. Meteor. Soc.*, **75**, 41–56.

Smith, R., 1990: Why can't stably stratified air rise over high ground? *Atmospheric Processes over Complex Terrain, Meteor. Monogr*, **45**, 105–107.

Stiperski, I. and V. Grubišić, 2011: Trapped lee wave interference in the presence of surface friction. *Journal of the Atmospheric Sciences*, **68**, 918–936.

Stiperski, I. et al., 2016: Stratified water tank experiments on flow over double ridges. In preparation.

Strauss, L., S. Serafin, and V. Grubišić, 2015: Atmospheric rotors and severe turbulence in a long deep valley. *J. Atmos. Sci.*, **73**, 1481–1506.

Teixeira, M. A., 2014: The physics of orographic gravity wave drag. *Frontiers in Physics*, **2 (43)**.

Teixeira, M. A., J. L. Argaín, and P. M. Miranda, 2013: Orographic drag associated with lee waves trapped at an inversion. *J. Atmos. Sci.*, **70**, 2930–2947.

Turner, J. S., 1973: *Buoyancy effects in fluids*. Cambridge University Press, 368 pp.

Vosper, S. B., 2004: Inversion effects on mountain lee waves. *Q. J. R. Meteorol. Soc.*, **130**, 1723–1748.

Wood, I. and J. Simpson, 1984: Jumps in layered miscible fluids. *J. Fluid Mech.*, **140**, 329–342.

Wurtele, M., R. Sharman, and A. Datta, 1996: Atmospheric lee waves. *Annual Review of Fluid Mechanics*, **28**, 429–476.

Yih, C.-S. and C. Guha, 1955: Hydraulic jump in a fluid system of two layers. *Tellus*, **7**, 358–366.

Table 1. Relevant parameters for (a) simulations of the energy flux experiment presented in section 4.2 and (b) HYIV-CNRS-SECORO experiments and the corresponding numerical simulations. The parameters U, N_1 and θ_0 in the simulations in table (b) are the same as in table (a).

a) Energy-flux experiment

$H[m]$	$h_1[m]$	N_1 [s^{-1}]	N_2 [s^{-1}]	$\Delta\theta$ [K]	U [m s^{-1}]	θ_0 [K]
200	1000	0	0.01	6–20	10	300

b) Amplitude experiment

			HYDRALAB				Simulation		
Nr.	Fr	H/h_i	$h_1[m]$	N_2 [s^{-1}]	$\Delta\rho$ [kg m^{-3}]	U [m s^{-1}]	h_1 [km]	N_2 [s^{-1}]	$\Delta\theta$ [K]
188	0.88	0.89	0.15	0.83	39.1	0.20	1.1	0.0055	3.6
189	0.96	0.89	0.15	0.83	40.1	0.22	1.1	0.0049	2.9
195	0.78	0.70	0.19	0.83	43.2	0.21	1.4	0.0052	3.5
196	0.87	0.69	0.19	0.82	44.1	0.24	1.4	0.0046	2.8
197	0.97	0.69	0.19	0.83	44.3	0.27	1.4	0.0041	2.3
198	1.07	0.69	0.19	0.83	43.8	0.29	1.4	0.0038	1.8
203	0.67	0.50	0.26	0.82	51.3	0.23	2.0	0.0047	3.5
204	0.76	0.50	0.26	0.83	52.3	0.27	2.0	0.0041	2.6
205	0.86	0.50	0.26	0.84	52.9	0.30	2.0	0.0037	2.1
208	0.55	0.50	0.26	0.86	54.5	0.20	2.0	0.0058	5.1
213	0.80	1.11	0.12	0.85	46.7	0.18	0.9	0.0063	5.3
214	0.90	1.11	0.12	0.84	46.8	0.20	0.9	0.0055	4.1
215	1.01	1.10	0.12	0.85	46.6	0.23	0.9	0.0050	3.3
324	0.78	0.90	0.15	0.49	30.4	0.16	1.1	0.0041	4.5
325	0.85	0.90	0.15	0.49	32.9	0.18	1.1	0.0036	3.8
326	0.98	0.90	0.15	0.49	31.0	0.20	1.1	0.0033	2.9
332	0.78	0.51	0.26	0.62	23.6	0.19	2.0	0.0044	2.5
333	0.88	0.50	0.26	0.62	23.2	0.21	2.0	0.0039	2.0
334	0.65	0.50	0.26	0.62	23.3	0.15	2.0	0.0053	3.7
336	0.83	0.50	0.26	0.62	23.5	0.20	2.0	0.0041	2.2
340	0.77	0.70	0.19	0.59	26.5	0.17	1.4	0.0047	3.6
341	0.88	0.70	0.19	0.59	26.2	0.19	1.4	0.0042	2.8
342	0.98	0.70	0.19	0.59	26.1	0.21	1.4	0.0037	2.2
373	0.89	0.90	0.15	0.52	27.5	0.17	1.1	0.0040	3.4
382	0.88	0.70	0.19	0.58	27.0	0.19	1.4	0.0040	2.8

Chapter 5

Conclusions and Outlook

In this thesis two of the most striking responses in atmospheric mesoscale flow over topography have been investigated: lee waves and hydraulic jumps. Both are known to give rise to boundary-layer separation and severe low-level turbulence in atmospheric rotors. In the existing literature, lee waves and hydraulic jumps are addressed mostly independently using different theoretical models. While gravity waves are typically studied using the linearized Euler equations under the Boussinesq approximation, hydraulic jumps are investigated using the fully nonlinear shallow-water equations. The former framework describes well the propagation of waves, but typically underestimates the amplitude of finite-amplitude lee waves. The latter framework, in contrast, can accurately describe nonlinear flows, but is restricted to the hydrostatic flow limit and not appropriate to study lee waves, which are nonhydrostatic. This thesis bridges those two independent theoretical frameworks and shows that lee waves and hydraulic jumps are related phenomena. In fact, hydraulic jumps were found to correspond to the limiting case of breaking lee waves.

Further investigations in this thesis are focused on the coupling between terrain-induced gravity waves and atmospheric rotors. The comparison of numerical simulations of wave-induced atmospheric rotors and linear theory predictions of the wave amplitude revealed that rotor properties (strength and vertical extent) tightly correspond to the wave forcings and can be predicted from theory based on a correlation method. For that reason, a large part of this thesis (chapters 2, 3 and 4) was dedicated to analytical investigations of the properties of large amplitude nonhydrostatic gravity waves. Two wave types are addressed: (i) vertically propagating internal gravity waves (chapter 2, see also section 1.2.1) and (ii) interfacial lee waves (chapter 3 and 4, see also section 1.2.2).

5.1 Internal gravity waves

Different mountain wave regimes in uniformly stratified flow, ranging from weakly to strongly nonlinear and near-hydrostatic to nonhydrostatic, have been studied in chapter (2) by means of two-dimensional numerical simulations and linear theory. While the simulations with free-

slip lower boundary conditions showed strong downslope wind storms and a hydraulic-jump-like behaviour, the simulation set in which surface friction was imposed led to boundary-layer separation and the development of rotors. Good agreement was found between the regime transitions in the simulations and the BLS regime diagram by Baines (1995); the regimes are (i) no separation, (ii) bluff-body separation and (iii) wave-induced separation. Closer examination of the simulation results revealed new insights into the process of rotor formation in uniformly stratified flows.

What flow condition leads to the largest (in terms of vertical extent) and strongest rotors? The most significant rotors with respect to both properties appeared to occur in nonlinear (large NH/U) and nonhydrostatic (small NL/U) flows. Linear theory reveals that these conditions are favorable for strong horizontal pressure gradient forces at the surface and strong vertical motion. In nonhydrostatic flows, rotor properties are well explained by linear theory estimates of the mountain wave forcing. In this case, rotors are coupled with the mountain wave and, thus, rotor height and strength can be determined from the mountain wave properties. In the case of near-hydrostatic flows, in contrast, the rotors appear not to be coupled with the mountain wave aloft.

What is the origin of rotors in hydrostatic flows? In order for rotor formation to occur in hydrostatic flows, wave breaking and the formation of a strongly stratified low-level jet is necessary. This is consistent with previous studies on rotor formation in uniformly stratified flows (e.g. Jiang et al., 2007; Smith and Skyllingstad, 2009). Once the stratified jet separates from the surface, a secondary nonhydrostatic wave develops along the jet and rotors form underneath the crests. The wavelength of the secondary trapped wave, and thus the rotor width, can be described quite accurately with linear interfacial wave theory (see section 1.2.2). In conclusion, rotors are a nonhydrostatic phenomenon even in near-hydrostatic flows. The necessary strong surface pressure gradients and strong vertical motions are associated with the secondary waves, the non-hydrostatic interfacial waves. If the amplitude and wavelength of the interfacial disturbance are known, rotor properties can be determined similarly as in the nonhydrostatic case.

5.2 Interfacial lee waves

As explained in the previous section, rotor properties are related to the wave forcing and can be predicted from the wave properties. For that reason, the properties of interfacial waves (wavelength and amplitude) have been investigated analytically in two papers presented in chapter (3) and (4). The results are summarized in what follows.

Is it possible to determine the wavelength of lee waves on the boundary-layer inversion from the upstream flow parameters? This aspect has been investigated in chapter (3). The

wavelength can be determined from the frequency dispersion relationship (FDR) of interfacial waves and depends essentially on the upstream flow conditions. The wavelength tends to decrease for decreasing flow speed U, increasing inversion strength $\Delta\theta$, larger boundary-layer depth h_1 and stronger free-atmospheric stratification N_2. Wavelength predictions from the FDR are robust and remain relatively accurate even for large amplitude waves. In contrast to resonant lee waves, the wavelength of interfacial waves can be determined analytically under certain conditions. In case of a deep layer or a short wavelength, so that $kh_1 \gg 1$, the deep-water approximation becomes accurate and yields $k = g'/(2U^2) + N_2^2/(2g')$ for the wavenumber. This simple expression is typically valid for lee waves on the boundary-layer inversion, as was shown in section (3.5).

Upper-level stratification is of particular interest in the context of boundary-layer lee waves, because it introduces a threshold for the wavelength ($k_{min}^2 = N^2/U^2$ or equivalently $\lambda_{max} = 2\pi U/N$) above which wave modes propagate through the interface into the stratified upper layer without being trapped. Therefore, the wavelength of a lee wave cannot exceed $\lambda_{max} = 2\pi U/N$. This upper limit for the wavelength can have important implications for hydraulic theory, which is valid in the long-wavelength- or shallow-water limit, so that $kh_1 \ll 1$ (shallow-water approximation). It is shown in section (3.5) that the trapping criterion ($k^2 > N^2/U^2$) is in conflict with the shallow-water assumption for typical atmospheric conditions, impacting the accuracy of hydraulic theory.

Is it possible to determine the amplitude of lee waves on the boundary-layer inversion from the upstream flow parameters? Only little is known from previous literature about how the amplitude of interfacial lee waves depends on the upstream flow conditions. A new analytical approach for amplitude predictions has been presented in chapter (4). This method, which has been originally developed for surface water waves by Lemoine (1948), assumes that energy flux convergence at an internal hydraulic jump is compensated by energy radiation through laminar lee waves. This assumption is valid for hydraulic jumps with a small interface height difference (jump size) across the transition (Favre, 1935). In these conditions, the lee wave amplitude can be obtained from the upstream flow parameters, the jump size and the wavelength. The comparison of the analytical model predictions with numerical simulations showed excellent agreement. Furthermore, the accuracy of the analytical model in predicting the wave amplitudes measured in water tank experiments is comparable to that of numerical simulations, which are expected to be most accurate in that respect.

For the investigations in chapter (4) the jump parameters as well as the wavelength have been measured directly in numerical simulations and water tank experiments. However, amplitude estimates can be reduced entirely to a problem determined by the upstream flow parameters by parameterizing the jump size with a hydraulic model (e.g. Houghton and Kasahara, 1968) and the wavelength with the deep-water expression for the wavelength, see above. This is useful to predict wave-induced flow separation and rotor formation in boundary-layer flow over a mountain based on the upstream flow parameters.

Can the flow response (lee waves or hydraulic jumps) downstream of a mountain be inferred from the upstream flow profile? This question has been addressed in chapter (4). Using scaling arguments, a nonlinearity parameter $\gamma \sim |u'/U|$ has been developed for interfacial waves, analogous to NH/U for vertically propagating mountain waves. Similar to $NH/U = 1$, $\gamma = 1$ predicts wave-induced flow stagnation and, thus, lee wave breaking. The verification with water tank experiments and numerical simulations of Vosper (2004) revealed that $\gamma = 1$ accurately predicts the regime transition between laminar lee waves and hydraulic jumps. This suggests that hydraulic jumps represent the limiting case of breaking lee waves. Since γ has been derived from scaling arguments, it is formulated in terms of nondimensional flow governing parameters (Fr, H/h_1, H/L and NH/U) and the leeward flow response is conserved across scales. This becomes apparent in the good agreement of the regime predictions in water tank experiments (scale of ~ 1 m) and the numerical simulations by Vosper (2004) (scale of ~ 1000 m).

5.3 Outlook

In this thesis wave-induced boundary-layer separation has been investigated mostly in idealized flow conditions to identify important physical processes and explain them quantitatively with analytical models. The extent to which the above findings can be applied to real flow conditions is to be clarified in future research. It can be expected that dominant physical processes in idealized flows (such as wave forcings) are also dominant in real flows. To this end, case studies applying analytical models to real-case observations of boundary-layer separation would be required. A comprehensive observational dataset of wave-induced boundary-layer separation was collected during the T-REX campaign (Grubišić et al., 2008) and is expected to reveal further potential for the improvement of the analytical models developed in this thesis.

Room for further development of the analytical wavelength and amplitude models lies, for example, in the inclusion of variable wind speed with height, which is expected to provide deeper insight into the role of wind shear in the dynamics of interfacial waves. In this context, the development of shear instabilities, such as Kelvin-Helmholtz or Holmboe instability, would be of particular interest. Finally, analogies between hydraulic flow and multi-layer continuously-stratified flow (Durran, 1986a) reveal potential for further research on extending the amplitude model (described in section 4.2) to predict the amplitude of resonant lee waves.

Bibliography

Airy, G. B., 1841: Tides and waves. *Encyclopaedia Metropolitana (1817–1845), Mixed Sciences*, **3**, 241 – 396.

Ambaum, M. H. P. and D. P. Marshall, 2005: The Effects of Stratification on Flow Separation. *J. Atmos. Sci.*, **62**, 2618–2625.

Baines, P. G., 1995: *Topographic effects in stratified fluids*. Cambridge University Press, 482 pp.

Baines, P. G. and K. P. Hoinka, 1985: Stratified Flow over Two-Dimensional Topography in Fluid of Infinite Depth: A Laboratory Simulation. *J. Atmos. Sci.*, **42**, 1614–1630.

Batchelor, G. K., 1967: *An introduction to fluid dynamics*. Cambridge University Press, 615 pp.

Belušić, D., M. Žagar, and B. Grisogono, 2007: Numerical simulation of pulsations in the bora wind. *Q. J. R. Meteorol. Soc.*, **133**, 1371–1388.

Bougeault, P., et al., 2001: The MAP Special Observing Period. *Bull. Amer. Meteor. Soc.*, **82**, 433–462.

Craik, A. D., 1988: *Wave interactions and fluid flows*. Cambridge University Press, 325 pp.

Craik, A. D., 2004: The origins of water wave theory. *Annu. Rev. Fluid Mech.*, **36**, 1–28.

Doyle, J. D. and D. R. Durran, 2002: The Dynamics of Mountains-Wave-Induced Rotors. *J. Atmos. Sci.*, **59**, 186–201.

Doyle, J. D. and D. R. Durran, 2007: Rotor and Subrotor dynamics in the lee of three-dimensional terrain. *J. Atmos. Sci.*, **64**, 4202–4221.

Doyle, J. D. and R. B. Smith, 2003: Mountain waves over the Hohe Tauern: Influence of upstream diabatic effects. *Q. J. R. Meteorol. Soc.*, **129**, 799–823.

Durran, D. R., 1986a: Another look at downslope windstorms. Part I: The development of analogs to supercritical flow in an infinitely deep, continuously stratified fluid. *J. Atmos. Sci.*, **43**, 2527–2543.

Durran, D. R., 1986b: Mountain waves. *Mesoscale Meteorology and Forecasting*, 472–492.

Favre, H., 1935: *Etude théorique et expérimentale des ondes de translation dans les canaux découverts*. Dunod et Cie, Paris.

Fernando, H. J. S., et al., 2015: The MATERHORN: Unraveling the Intricacies of Mountain Weather. *Bull. Amer. Meteorol. Soc.*, **96**, 1945–1967.

Förchtgott, J., 1949: Wave streaming in the lee of mountain ridges. *Bull. Met. Czech. Prague*, **3**, 49–51.

Förchtgott, J., 1957: Active turbulent layer downwind of mountain ridges. *Stud. Geophys. Geod.*, **1**, 173–181.

French, J. R., S. J. Haimov, L. D. Oolman, V. Grubišić, S. Serafin, and L. Strauss, 2015: Wave-Induced Boundary Layer Separation in the Lee of the Medicine Bow Mountains. Part I: Observations. *J. Atmos. Sci.*, **72**, 4845–4863.

Gohm, A., G. J. Mayr, A. Fix, and A. Giez, 2008: On the onset of bora and the formation of rotors and jumps near a mountain gap. *Q. J. R. Meteorol. Soc.*, **134**, 21–46.

Gohm, A., et al., 2009: Air pollution transport in an Alpine valley: Results from airborne and ground-based observations. *Bound. Lay. Meteorol.*, **131**, 441 – 463.

Goldstein, S., 1931: On the Stability of Superposed Streams of Fluids of Different Densities. *Proc. Roy. Soc. Series A*, **132**, 524–548.

Grisogono, B. and D. Belušić, 2009: A review of recent advances in understanding the meso- and microscale properties of the severe Bora wind. *Tellus A*, **61**, 1–16.

Grubišić, V. and B. J. Billings, 2007: The intense lee-wave rotor event of Sierra Rotors IOP 8. *J. Atmos. Sci.*, **64**, 4178–4201.

Grubišić, V., J. Sachsperger, and R. M. A. Caldeira, 2015: Atmospheric Wake of Madeira: First Aerial Observations and Numerical Simulations. *J. Atmos. Sci.* , **72**, 4755–4776.

Grubišić, V., et al., 2008: The Terrain-Induced Rotor Experiment: A Field Campaign Overview Including Observational Highlights. *Bull. Amer. Meteor. Soc.*, **89**, 1513–1533.

Haurwitz, B., 1931a: Über die Wellenlänge von Luftwogen, I u. II Mitteilungen. *Gerlands Beitr. Gephys.*, **34, 35**, 213–232,16–24.

Haurwitz, B., 1931b: Zur Theorie der Wellenbewegungen in Luft und Wasser. *Veröff. Geophys. Inst. Leipzig Univ.*, **5**, 1–106.

Hertenstein, R. F., 2009: The influence of inversions on rotors. *Mon. Weather Rev.*, **137**, 433–446.

Hertenstein, R. F. and J. Kuettner, 2005: Rotor types associated with steep lee topography: Influence of the wind profile. *Tellus A*, **57**, 117–135.

Holmboe, J. and H. Klieforth, 1954: Sierra Wave Project, Final Report. Tech. rep., University of California, Los Angeles.

Holmboe, J. and H. Klieforth, 1957: Investigation of mountain lee waves and the air flow over the Sierra Nevada. Tech. rep., University of California, Los Angeles.

Houghton, D. D., 1964: An Example of Interaction Between Finite-Amplitude Gravity Waves. *J. Atmos. Sci.*, **21**, 493–499.

Houghton, D. D. and A. Kasahara, 1968: Nonlinear shallow fluid flow over an isolated ridge. *Commun. Pur. Appl. Math.*, **21**, 1–23.

Jiang, Q., J. D. Doyle, S. Wang, and R. B. Smith, 2007: On Boundary Layer Separation in the Lee of Mesoscale Topography. *J. Atmos. Sci.*, **63**, 401–419.

Kalthoff, N., et al., 2011: The dependence of convection-related parameters on surface and boundary-layer conditions over complex terrain. *Q. J. R. Meteorol. Soc.*, **137**, 70–80.

Klemp, J. B. and D. R. Lilly, 1975: The Dynamics of Wave-Induced Downslope Winds. *J. Atmos. Sci.*, **32**, 320–339.

Küttner, J., 1938: Moazagotl und Föhnwelle (Moazagotl and foehn wave). *Beitr. Phys. Atmos.*, **25**, 79114.

Küttner, J., 1939: Zur Entstehung der Föhnwelle. *Beitr. Phys. Atmos.*, **25**, 251–299.

Lareau, N. P., E. Crosman, C. D. Whiteman, J. D. Horel, S. W. Hoch, W. O. Brown, and T. W. Horst, 2013: The persistent cold-air pool study. *Bull. Amer. Meteor. Soc.*, **94**, 51–63.

Lehner, M., et al., 2016: The METCRAX II Field Experiment: A Study of Downslope Windstorm-Type Flows in Arizonas Meteor Crater. *Bull. Amer. Meteorol. Soc.*, **97**, 217–235.

Lemoine, R., 1948: Sur les ondes positives de translation dans les canaux et sur le ressaut ondulé de faible amplitude. *Houille Blanche*, **2**, 183–185.

Lester, P. F. and W. A. Fingerhut, 1974: Lower Turbulent Zones Associated with Mountain Lee Waves. *J. Appl. Meteor.*, **13**, 54–61.

Long, R. R., 1953: Some aspects of the flow of stratified fluids: I. A theoretical investigation. *Tellus*, **5**, 42–58.

Long, R. R., 1954: Some Aspects of the Flow of Stratified Fluids: II. Experiments with a Two-Fluid System. *Tellus*, **6**, 97–115.

Long, R. R., 1955: Some aspects of the flow of stratified fluids. III. Continuous density gradients. *Tellus*, **7**, 341.

Lyra, G., 1940: Theorie der stationären Leewellenströmung in freier Atmosphäre. *Beitr. z. Phys. d. Atmosphäre*, **26**, 197–206.

Lyra, G., 1943: Theorie der stationären Leewellenströmung in freier Atmosphäre. *ZAMM-Journal of Applied Mathematics and Mechanics/Zeitschrift für Angewandte Mathematik und Mechanik*, **23**, 1–28.

Mohr, T., 1971: Karman-Wirbel im Lee von Jan Mayern. *Met. Rdsch.*, **24**, 30–32.

Nappo, C. J., 2012: *An introduction to atmospheric gravity waves*. 2d ed., Academic Press, 359 pp.

Nunalee, C. G., A. Horváth, and S. Basu, 2015: High-resolution numerical modeling of mesoscale island wakes and sensitivity to static topographic relief data. *Geosci. Model Dev.*, **8**, 2645–2653.

Prandtl, L., 1904: Über die Flüssigkeitsbewegung bei sehr kleiner Reibung. *Verhandlungen des dritten internationalen Mathematiker-Kongresses in Heidelberg vom 8. bis 13. August 1904, A. Krazer, ed., Teubner, Leipzig, Germany*, 484–491.

Prestel, I. and V. Wirth, 2016: What flow conditions are conducive to banner cloud formation? *Published online in J. Atmos. Sci.*, doi: 10.1175/JAS-D-15-0319.1.

Queney, P., 1947: *Theory of perturbations in stratified currents with applications to air flow over mountain barriers*. University of Chicago Press, 80 pp.

Queney, P., 1948: The problem of air flow over mountains: A summary of theoretical studies. *Bull. Amer. Meteorol. Soc.*, **29**, 16–26.

Queney, P., G. Corby, N. Gerbier, H. Koshmieder, and J. Zierep, 1960: The airflow over mountains. Tech. Rep. 34, WMO.

Rayleigh, 1914: On the theory of long waves and bores. *Proc. Roy. Soc. Series A, Papers 6*, **90**, 324–328.

Sachsperger, J., S. Serafin, and V. Grubišić, 2015: Lee waves on the boundary-layer inversion and their dependence on free-atmospheric stability. *Front. Earth Sci.*, **3 (70)**, doi: 10.3389/feart.2015.00070.

Sachsperger, J., S. Serafin, and V. Grubišić, 2016a: Dynamics of rotor formation in uniformly stratified two-dimensional flow over a mountain. *Q. J. R. Meteorol. Soc.*, **142**, 1201–1212.

Sachsperger, J., S. Serafin, V. Grubišić, I. Stiperski, and P. Alexandre, 2016b: The amplitude of lee waves on the boundary-layer inversion. *submitted to Q. J. R. Meteorol. Soc.*

Schappert, S. and V. Wirth, 2015: Origin and Flow History of Air Parcels in Orographic Banner Clouds. *J. Atmos. Sci.*, **72**, 3389–3403.

Schär, C. and R. B. Smith, 1993: Shallow-water flow past isolated topography. Part II: Transition to vortex shedding. *J. Atmos. Sci.* , **50**, 1401–1412.

Scorer, R., 1949: Theory of waves in the lee of mountains. *Q. J. R. Meteorol. Soc.*, **75**, 41–56.

Sheridan, P. and S. Vosper, 2012: High-Resolution Simulations of Lee Waves and Downslope Winds over the Sierra Nevada during T-REX IOP 6. *J. Appl. Meteor.*, **51**, 1333–1352.

Smith, C. M. and E. D. Skyllingstad, 2009: Investigation of Upstream Boundary Layer Influence on Mountain Wave breaking and Lee Wave Rotors Using a Large-Eddy Simulation. *J. Atmos. Sci.*, **66**, 3147–3164.

Smith, R. B., 1979: The influence of mountains on the atmosphere. *Adv. Geophys.*, **21**, 87–230.

Smith, R. B., 1985: On severe downslope winds. *J. Atmos. Sci.*, **42**, 2597–2603.

Stiperski, I. and V. Grubišić, 2011: Trapped lee wave interference in the presence of surface friction. *J. Atmos. Sci.*, **68**, 918–936.

Stokes, G. G., 1847: On the theory of oscillatory waves. *Trans. Camb. Philos. Soc.*, **8**, 441–455.

Strauss, L., 2015: Mountain-wave-induced rotors and low-level turbulence. Ph.D. thesis, University of Vienna, URL `http://othes.univie.ac.at/38943/`.

Strauss, L., S. Serafin, and V. Grubišić, 2015a: Atmospheric rotors and severe turbulence in a long deep valley. *J. Atmos. Sci.*, **73**, 1481–1506.

Strauss, L., S. Serafin, S. Haimov, and V. Grubišić, 2015b: Turbulence in breaking mountain waves and atmospheric rotors estimated from airborne in situ and Doppler radar measurements. *Q. J. R. Meteorol. Soc.*, **141**, 3207–3225.

Stull, R. B., 2012: *An introduction to boundary layer meteorology*, Vol. 13. Springer Netherlands, 666 pp.

Taylor, G., 1931: Effect of variation in density on the stability of superposed streams of fluid. *Proc. Roy. Soc. Series A*, **132**, 499–523.

Teixeira, M. A., 2014: The physics of orographic gravity wave drag. *Front. Phys.*, **2 (43)**, doi: 10.3389/fphy.2014.00043.

Turner, J. S., 1973: *Buoyancy effects in fluids*. Cambridge University Press, 368 pp.

Vosper, S. B., 2004: Inversion effects on mountain lee waves. *Q. J. R. Meteorol. Soc.*, **130**, 1723–1748.

Wirth, V. et al., 2012: Banner clouds observed at Mount Zugspitze. *Atmos. Chem. Phys.*, **12**, 3611–3625.

Wurtele, M., R. Sharman, and A. Datta, 1996: Atmospheric lee waves. *Annu. Rev. Fluid Mech.*, **28**, 429–476.

Zängl, G., 2003: Orographic Gravity waves Close to the Nonhydrostatic Limit of Vertical Propagation. *J. Atmos. Sci.*, **60**, 2045–2063.

Symbols

A	coefficient of the downward propagating wave branch
B	coefficient of the upward propagating wave branch
c_g	group velocity
d	inversion layer thickness
η	vorticity in y-direction
Fr	Froude number
g	gravitational acceleration
g'	reduced gravitational acceleration
h	topography height
H	maximum terrain height
h	terrain height
h_1	height of lower layer
h_2	height of upper layer
i	imaginary unit or layer index (if used as suffix)
k	horizontal wavenumber
l	Scorer parameter
L	mountain width
λ	wavelength
m	vertical wavenumber
n	wave amplitude decay rate
N	buoyancy Frequency
ω	apparent wave frequency for a stationary observer
p	pressure perturbation
p_s	surface pressure perturbation
ψ	wave quantity representing u, w, p and ρ
$\tilde{\psi}$	vertical structure of the wave quantities
$\hat{\psi}$	vertical structure of the wave quantities scaled with the density term $(\rho_o(z)/\rho_s)^{1/2}$
ρ	density perturbation
ρ_0	density profile
$\Delta\theta$	inversion strength
θ	potential temperature
u	horizontal wind speed perturbation
U	mean horizontal wind speed
w	vertical wind speed
x	horizontal distance
z	geometric altitude
z'	geometric altitude with respect to layer interface
z_0	roughness length

Acronyms and Abbreviations

BC	boundary condition
BLS	boundary-layer separation
FDR	frequency dispersion relationship
LTZ	lower turbulence zone
MAP	Mesoscale Alpine Program
MATERHORN	Mountain Terrain Atmospheric Modeling and Observations Program
METCRAX II	Meteor Crater Experiment
MODIS	Moderate Resolution Imaging Spectroradiometer
NASA	National Aeronautics and Space Administration
NASA06	NASA Orographic Clouds Experiment
T-REX	Terrain-induced Rotor Experiment